Novel Plasmonic Imaging Techniques for Measuring Protein Kinetics

by

Yan Wang

A Dissertation Presented in Partial Fulfillment
of the Requirements for the Degree
Doctor of Philosophy

Approved August 2018 by the
Graduate Supervisory Committee:

Nongjian Tao, Chair
Junseok Chae
Michael Goryll
Shaopeng Wang

ARIZONA STATE UNIVERSITY

December 2018

ABSTRACT

Proteins play a central role to human body and biological activities. As powerful tools for protein detections, many surface plasmon resonance based techniques have been developed to enhance the sensitivity. However, sensitivity is not the only final goal. As a biosensor, four things really matter: sensitivity, specificity, resolution (temporal/spatial) and throughput.

This dissertation presents several works on developing novel plasmonic based techniques for protein detections on the last two aspects to extend the application field. A fast electrochemically controlled plasmonic detection technique is first developed with the capability of monitoring electrochemical signal with nanosecond response time. The study reveals that the conformational gating of electron transfer in a redox protein (cytochrome c) takes place over a broad range of time scales (sub-μs to ms). The second platform integrates ultra-low volume piezoelectric liquid dispensing and plasmonic imaging detection to monitor different protein binding processes simultaneously with low sample cost. Experiment demonstrates the system can observe binding kinetics in 10×10 microarray of 6 nL droplet, with variations of kinetic rate constants among spots less than ±5%. A focused plasmonic imaging system with bi-cell algorithm is also proposed for spatial resolution enhancement. The two operation modes, scanning mode and focus mode, can be applied for different purposes. Measurement of bacterial aggregation demonstrates the higher spatial resolution. Detections of polystyrene beads binding and 50 nm gold nanoparticles oscillation show a high signal to noise ratio of the system.

The real properties of protein rely on its dynamic personalities. The above works shed light upon fast and high throughput detection of protein kinetics, and enable more

applications for plasmonic imaging techniques. It is anticipated that such methods will help to invoke a new surge to unveil the mysteries of biological activities and chemical process.

To my beloved parents,

Zhiquan Wang and Ying Liu

and my dear wife,

Hui Wang

ACKNOWLEGMENTS

I would like to express my sincere gratitude to my advisor, Prof. Nongjian Tao, for his continuous guidance, encouragement and support for my Ph.D. years. Without his guidance, the achievement of my research work would not have been possible. His patience, motivation and wealth of knowledge always inspire me. If science is a sea, he is the one who provides me the ship and leads me to find the way. Thanks for teaching me critical thinking and always open for discussion.

I would like to thank my committee members, Prof. Junesok Chae, Prof. Michael Goryll and Prof. Shaopeng Wang, for their valuable advice, discussion and help. You definitely provided me with the suggestions that help me successfully complete my dissertation. Special thanks to Prof. Shaopeng Wang for leading me to the field of engineer optics which guides me to my future job.

I would also like to thank my parents and my wife Hui for always being there. Your encouragement is one of most important things who supports me during the past years.

It is my honor to be a member in BB center and I enjoyed my time here. I want specially thank Dr. Xiaonan Shan for leading me into the SPR field and selfless sharing his valuable experience. Thank Mr. Feng Xiao for cooperating with me on the experiments of IMPDS project. Thanks to my peers, Dr. Yunze Yang, Dr. Xianwei Liu and Dr. Wenwen Jing for fruit discussion and good advice on the research. Explicitly thanks Drs. Francis Tsow, Peter Wiktor, Yixian Wang, Zixuan Chen, Limin Xiang, Chenbin Liu, Yan Guan, Yueqi Li, Yue Deng, Fenni Zhang, Fang Chen, Di Wang, Xiaojun Xian, Erica Forzani, as well as Mr. Guangzhong Ma, Ms. Runli Liang, Ms. Ashley Hunt, Ms. Chenwen Lin, Ms. Manni Mo. I will always remember the time working with you.

TABLE OF CONTENTS

Page

CHAPTER Page

CHAPTER Page

LIST OF FIGURES

Figure Page

Figure Page

Figure Page

Figure Page

LIST OF TABLES

Table Page

CHAPTER 1

INTRODUCTION OF SURFACE PLASMON RESONANCE

1.1 Introduction

Surface Plasmon Resonance (SPR) is an optical approach that measures the local refractive index change within the vicinity of a metal surface. Due to its physical properties, SPR provides a label-free, real time, versatile and highly sensitive way with numerous applications in a variety of disciplines.

Compared with labeled techniques such as fluorescence, SPR technique can eliminate the side effect that fluorescent molecule may bring to the biological system, which may make the detection results uncertain.[1] SPR provides the localized refractive index information which may be very useful for imaging techniques. Therefore, scientists show great interest in it and it has been greatly developed during the past several decades.

So far SPR has been used to measure various phenomenon: biomolecular interactions such as protein-protein interactions and DNA hybridizations, temperature and thermal imaging, metal ion concentrations, protein and DNA arrays, single cell process, and electrochemical reactions imaging.[1-13] The versatile of samples offers SPR a lot of opportunities in both biology and chemistry.

1.2 Surface Plasmon Resonance

If we interpret the surface plasmon resonance literally, it is the resonant oscillation of surface charge stimulated by exterior applied electromagnetic field. In order to understand the surface plasmon resonance, we need to first explain surface plasmons.

A plasmon can be defined as a quantum for the collective oscillation of free electrons, usually at the interface between metals and dielectrics. Surface plasmons occur at the interface of a vacuum or material with a positive dielectric constant, and material with a negative dielectric constant (usually a metal or doped dielectric) whose electrons behave like those of a quasi-free electron gas. These plasmons represent the quanta of the oscillations of surface charges, which are produced by exterior electric field in the boundary. The total excitation including both the charge motion in the metal and associated electromagnetic field in the dielectric, is called surface plasmon polariton (SPP).

For surface plasmon polariton, we can consider it as one kind of electromagnetic wave, therefore the electric field of its propagating can be expressed as

$$E = E_0 \mathrm{e}^{+\mathrm{i}(k_x x \pm k_z z - \omega t)} \tag{1.1}$$

where k_x and k_z is the wave number along x and z direction and ω is the frequency of electromagnetic wave as shown in Fig.1.1(a).

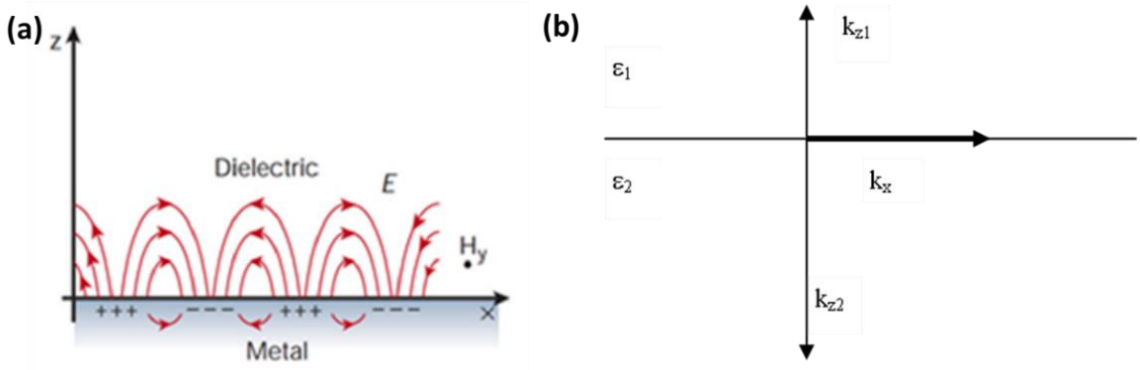

Figure 1.1: Excitation of SPP.(a) Description of SPPs; (b) Wave vector on the interface of different materials[14]

At the interface of the two materials, as shown in Fig.1.1(b), by solving Maxwell equations and using the boundary conditions, we have

$$\frac{k_{z1}}{\varepsilon_1} + \frac{k_{z2}}{\varepsilon_2} = 0 \tag{1.2}$$

$$k_x^2 + k_{zi}^2 = \varepsilon_i \left(\frac{\omega}{c}\right)^2 \quad (1.3)$$

where c is the speed of light, by combining these two equations, we can have the dispersion relationship of surface plasmon polaritons:

$$k_x = \frac{\omega}{c}\left(\frac{\varepsilon_1 \varepsilon_2}{\varepsilon_1 + \varepsilon_2}\right) \quad (1.4)$$

As for metal, the dielectric function is

$$\varepsilon(\omega) = 1 - \frac{\omega_P^2}{\omega^2} \quad (1.5)$$

where ω_P is the bulk plasmon frequency

$$\omega_P = \sqrt{\frac{ne^2}{\varepsilon_0 m^*}} \quad (1.6)$$

Thus, we can plot the dispersion relationship shown as the red curve in Fig.1.2. To excite the SPPs, which in other words is the Surface Plasmon Resonance, we need to have an exterior electromagnetic field dispersion relationship of which should have intersection with this one.

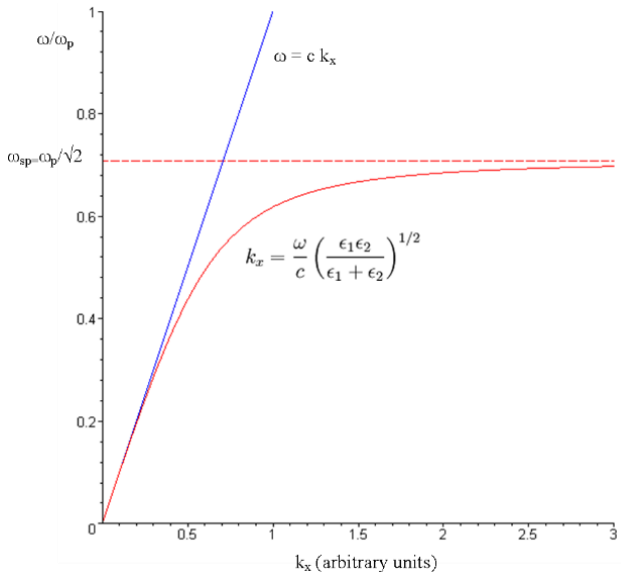

Figure 1.2: Dispersion relationship of SPPs[15]

1.3 Conventional SPR Configuration

To excite SPR, we need to have field which have a dispersion relationship intersecting with the SPP. In other words, it needs to couple into SPP; however, this is not a simple case. The blue curve in Fig.1.2 indicates the dispersion relationship of light in the air, and there is not going to have any SPR.

Before starting to discuss about the configuration to excite SPR, properties of light transmission on interface will be introduced since we need to couple light into SPPs. Fig.1.3 shows a schematic diagram of it.

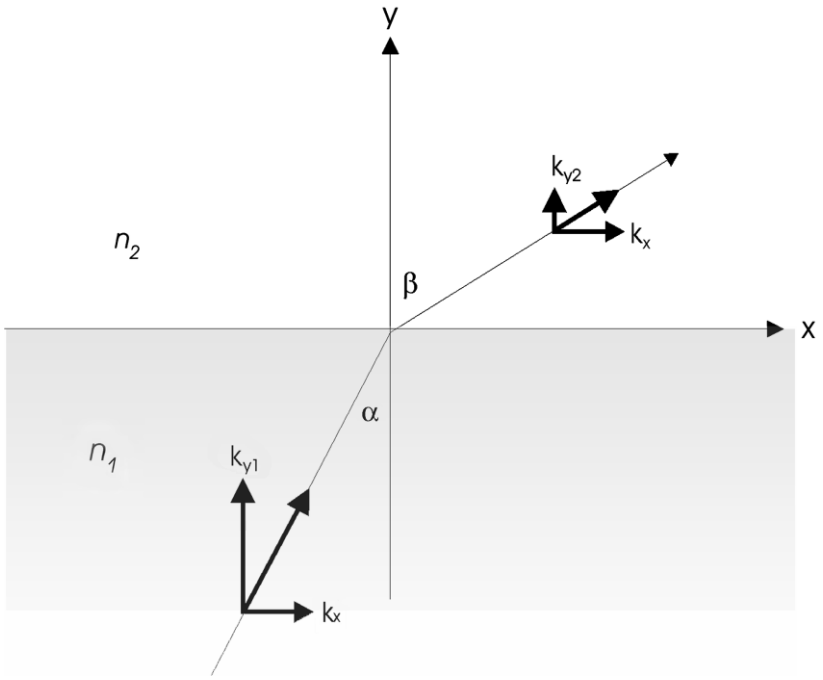

Figure 1.3: Transmission of light across the interface[16]

The relationship between wave vectors in different direction is

$$k = \sqrt{k_x^2 + k_y^2 + k_z^2} = \frac{n\omega}{c} \tag{1.7}$$

According the Snell's law, we have

$$n_1 \sin\alpha = n_2 \sin\beta \tag{1.8}$$

which can deduce that

$$k_1 \sin\alpha = k_2 \sin\beta\,, k_{x1} = k_{x2} \tag{1.9}$$

Thus, we can have the wave vector perpendicular to the surface

$$k_{y2} = \sqrt{n_1^2 \left(\frac{2\pi}{\lambda}\right)^2 \left(\frac{n_2^2}{n_1^2} - \sin^2\alpha\right)} \tag{1.10}$$

Suppose we have $n_1 > n_2$, and when total internal reflection happened, which is $n_1 \sin\alpha > n_2$, we are going to have k_{y2} as purely imaginary, and the electrical field of the transmitted light will be

$$E_t = E_0 e^{-k_{y2} y} e^{j(\omega t - k_x x)} \tag{1.11}$$

This indicates that the transmission light shows an exponential decay along the direction perpendicular to the interface, and the wave is called as 'evanescent wave'. This determines the properties that SPR is only sensitive to change in the vicinity of the interface and changing the refractive index will greatly influence the response.

In order to realize the excitation of SPR, Otto and Kretchmann developed two different configurations as shown in Fig.1.4, which is the same incident configuration as we showed before.[17,18] In both setups, p-polarized light is used because this particular polarization has the electric field vector oscillating normal to the plane that contains the metal film, and the light incidents to a prism at angle θ. Reflected light intensity is recorded by photodiode or CCD camera for different purpose. The difference is that Otto put the sample with lower optical density between the prism and metal, while in Kretchmann configuration the metal is between the prism and sample. In most cases, scientists and researchers use Kretchmann configuration due to that it is easily facilitated and operated. Next, we are going to take it as an example to show how the SPR is excited.

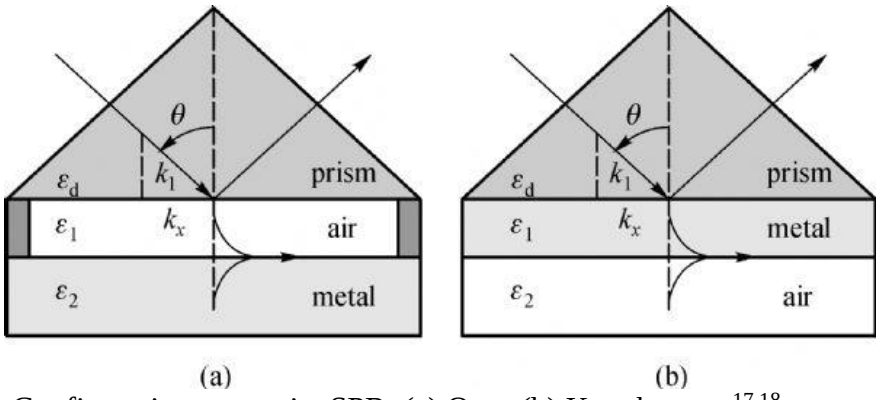

Figure 1.4: Configurations to excite SPR: (a) Otto; (b) Kretchmann.[17,18]

In Kretchmann configuration, we could have the in-plane wave vector of the light and the dispersion relationship

$$k_x = k_1 \sin\theta = n_p k \sin\theta \qquad (1.12)$$

$$\omega = \frac{ck_x}{n_p \sin\theta} \qquad (1.13)$$

Where n_p is the refractive index of prism. Therefore, as shown in Fig.1.5, by applying these configurations we could have the intersection between the SPPs and the incident light in the dispersion relationship diagram.

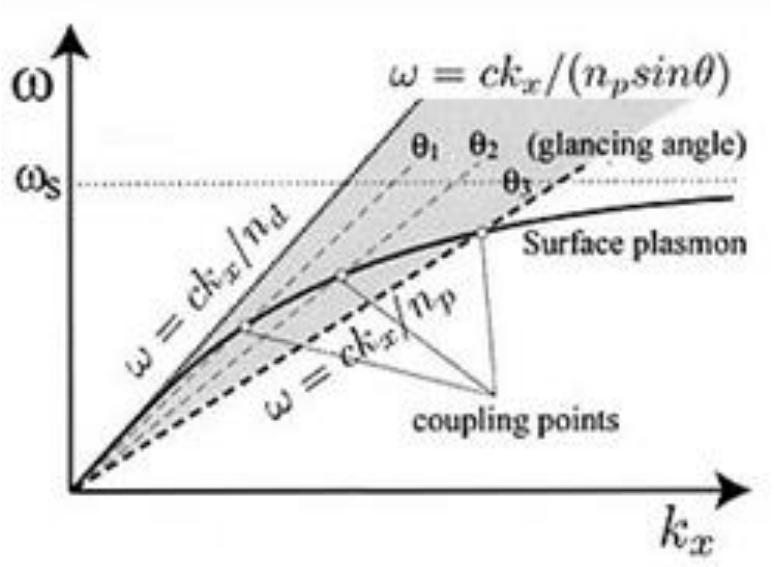

Figure 1.5: Coupling light wave vector to SPPs by tuning incident angle[19]

Fig.1.6 is an example shows how the refractive index of the surface influences dispersion relationship and how we measure this change. Since the energy of incident light each time is certain, which means it has certain ω, we can have certain k_x for SPR excitation. This decides the intersection point each time, which also determines the incident angle. This angle is usually called as 'dip' angle (incident angle has smallest reflectance, as shown in Fig.1.6. When the refractive index of the interface changes, the dispersion relationship of SPP will also change, so does the 'dip' angle. Therefore, if we park incident angle at certain value, the reflectance will vary. And this explains how we apply SPR to detect the activities on the metal surface.

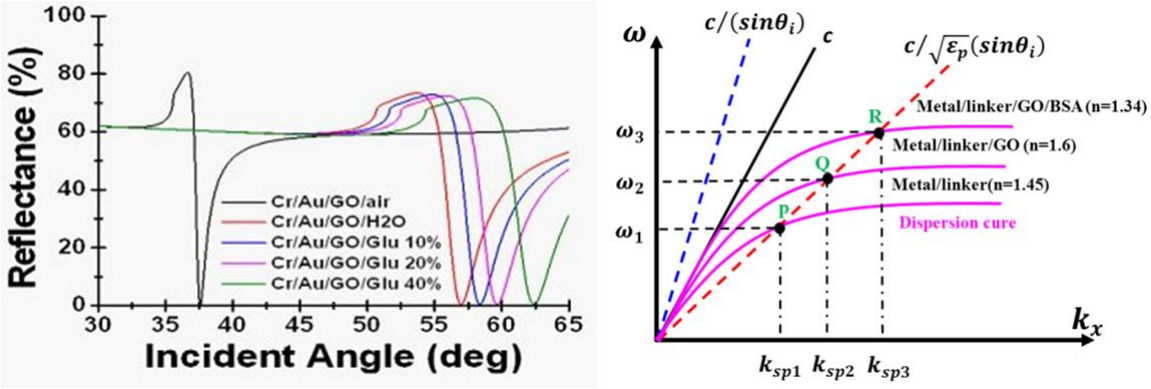

Figure 1.6: Dip angle changes as a function of surface refractive index[20]

1.4 Plasmonic Imaging

Two methods are usually used to detect the refractive index change, including scanning wavelength at a fixed angle and tuning angle with a fixed wavelength. Both methods need scan and scan takes time. For plasmonic imaging, the angle of incident light and camera are fixed at a specific angle near the linear region of the resonance dip, and the reflected light image is recorded. The variation of image intensity is linear related with the

refractive index change, therefore provides the lateral information of surface (Fig.1.7). This is called angle resolved SPR imaging (SPRi) and suitable for higher throughput detections.

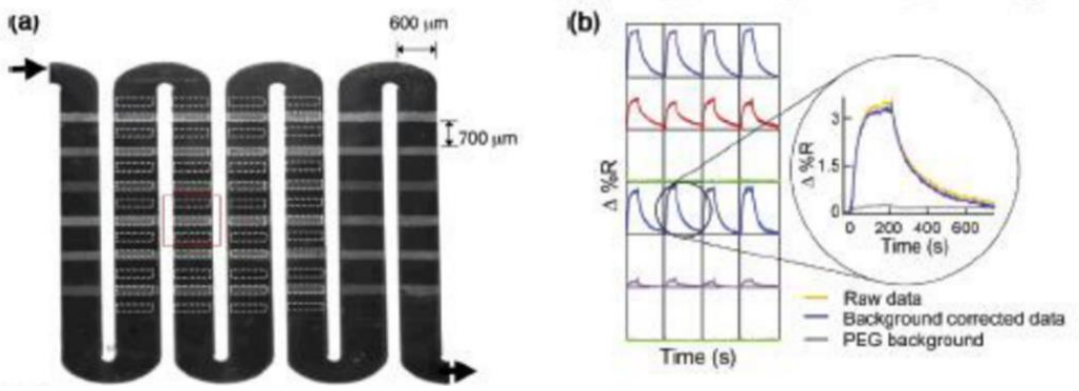

Figure 1.7: Typical SPRi response[21]

Huang et al. first used the high numerical aperture microscope objective for plasmonic imaging (Fig.1.8).[22] They used a 100× and NA=1.4 objective to measure the structure as small as 1 μm. This improved the resolution of SPRi, enabling observations of small molecules and structure such as nanomaterials and cells.

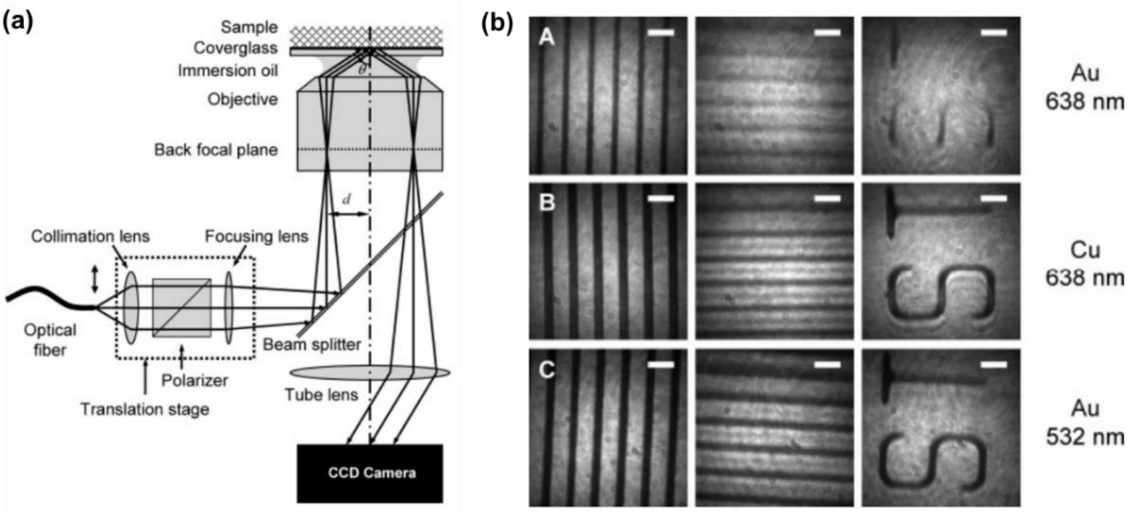

Figure 1.8: SPRi with high NA objective[22]

1.5 Proteins

Proteins are central and fundamental of almost every biological activity. Consist of only 20 amino acids, proteins are estimated 2 million types in a human body. As single entity they catalyze the metabolic reaction(insulin) and regulate the DNA replication (c-JUN and c-FOS). They also work together and formed interaction net called signaling pathways, regulating the cell and responding to stimuli from the changing of the surrounding environment. As shown in the EGFR pathway (Fig.1.9), p53 is a protein which can initiate cell apoptosis process when its level is too high. In normal case, MDM2 binds with phosphorylated p53 to keep it at the normal level and AKT1 is the kinase which catalyzed the phosphorylation of p53. When DNA was damaged due to cell degradation, MDM2 could not be synthesized and p53 would increase, leading to cell apoptosis and elimination of the damaged cells.

Those kinds of functions are governed ultimately by their dynamic character, including the transport of the proteins, their conformational change and interactions with other proteins.[23] Characterizing the dynamic structure and process leads to the birth of many techniques, such as X-ray protein crystallography, electron cryomicroscopy, atomic force spectroscopy, fluorescence resonance energy transfer, pump probe technique, gel electrophoresis and surface plasmon resonance.[24–31]

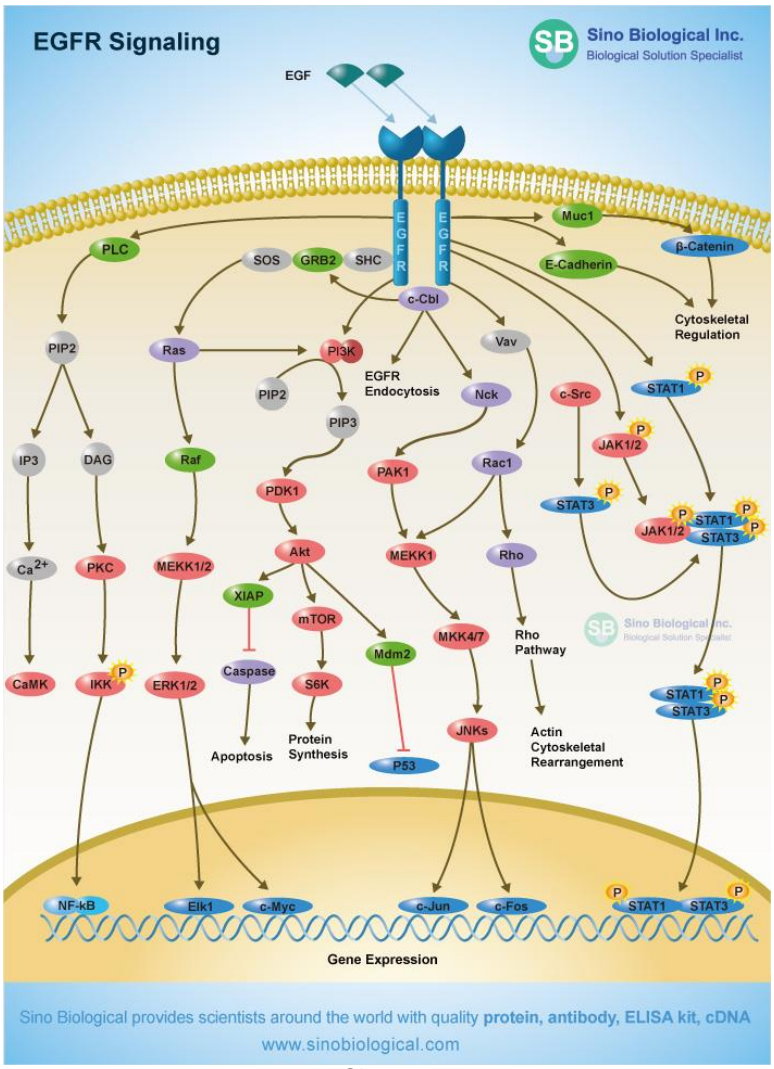

Figure 1.9: EGFR signaling pathway map[32]

1.6 Plasmonic Platforms for Protein Detection Applications

Since it was first used for biosensing 1983, SPR was greatly developed for many bio-applications such as gas sensing, drug screening and fundamental molecular interactions.[33–36] As for protein detections, although some study the conformational change of proteins, most of the researches on SPR are measuring the kinetic and thermodynamic of protein-protein and protein-small molecules interactions.[37,38] Conventional SPRi have been developed, commercialized and combined with microfluidic techniques to increase the

throughput. For example, the Biacore 8K can run 8 channels simultaneously and the Biorad ProteON^{TM} XPR36 can monitor a 6 by 6 interactions at the same time.[39,40]

Another direction for developing plasmonic technique is to enhance the sensitivity. Because proteins and drugs are usually small, improving the detection sensitivity is a must. One technique developed is plasmonic-based electrochemical impedance microscopy (P-EIM), which combines SPRi and electrochemical impedance spectroscopy. Foley et al. first experimentally measure the surface impedance by using the SPR microscopy.[41] The resonance angle θ_R is depends on the permittivity of surface, prism and metal

$$\sin(\theta_R) = \sqrt{\frac{\varepsilon_1 \varepsilon_m}{(\varepsilon_1+\varepsilon_m)\varepsilon_2}} \tag{1.14}$$

where $\varepsilon_1, \varepsilon_2$ and ε_m stand for the dielectric constant respectively. While according to the Drude model,

$$\varepsilon_m(f) = 1 - \frac{n_e e^2}{\varepsilon_0 m_e 4\pi^2 f^2} \tag{1.15}$$

where e, m_e, and n_e are the electron charge, mass, and density. If there is a change in the surface charge $\Delta\sigma$, then for a thin metal film it will be

$$\Delta\sigma = -e d_m \Delta n_e \tag{1.16}$$

Combining the last two equations we will have

$$\Delta\sigma = -\frac{e d_m \Delta n_e}{\varepsilon_m - 1} \Delta\varepsilon_m \tag{1.17}$$

Comparing this equation with the first equation in this section, the relationship between surface charge density and resonance angle will be

$$\Delta\sigma \sim \alpha \Delta\theta_R \tag{1.18}$$

Which indicated the differential of surface plasmon response linearly corresponds to the surface charge density change, providing the theoretical bases for measuring the

electrochemical signal by SPR microscopy. P-EIM technique was used to detect interactions between small molecule drugs and proteins, intracellular cell process and interactions between small molecule drugs and cell receptors.[5,42–44]

Shan et al. has proposed another way to detect protein binding based on monitoring the variation of nanoparticle oscillation using plasmonic imaging.[45] This is a charge sensitive platform because the oscillation amplitude of the particle is directly proportion to the surface charge of the nanoparticles. If precoating the target proteins on the nanoparticle surface, other molecular interaction with the protein could be measured. Applying this technique, they successfully observed the binding between streptavidin and biotin and phosphorylation of kinase.[45,46]

Other novel plasmonic platforms were also developed for different applications. Wang et al. has proposed the cell based plasmonic platforms, which can directly monitor the cell process and molecular interactions with cell surface receptors.[4,44,47,48] Liu et al. combined the patch clamp with plasmonic imaging, which enables the detection of the fast initiation and propagation of action potential within single neurons.[49]

CHAPTER 2

PLASMONIC BASED FAST ELECTROCHEMICAL DETECTION REVEALS MULTI-TIME SCALE CONFORMATIONAL GATING OF ELECTRON TRANSFER IN CYTOCHROME C

2.1 Introduction

Electrochemical Reaction is one of the most familiar phenomena in people's life, as shown in Fig.2.1. In biology, the famous processes photosynthesis and respiratory- involve a lot of electrochemical reactions, e.g. the water splitting with oxygen released, and the oxidation and reduction of different compounds along the electron transport chain. In other fields, such as photovoltaics and batteries, electrochemical reactions also play an important role, which define the efficient, quality and other properties.

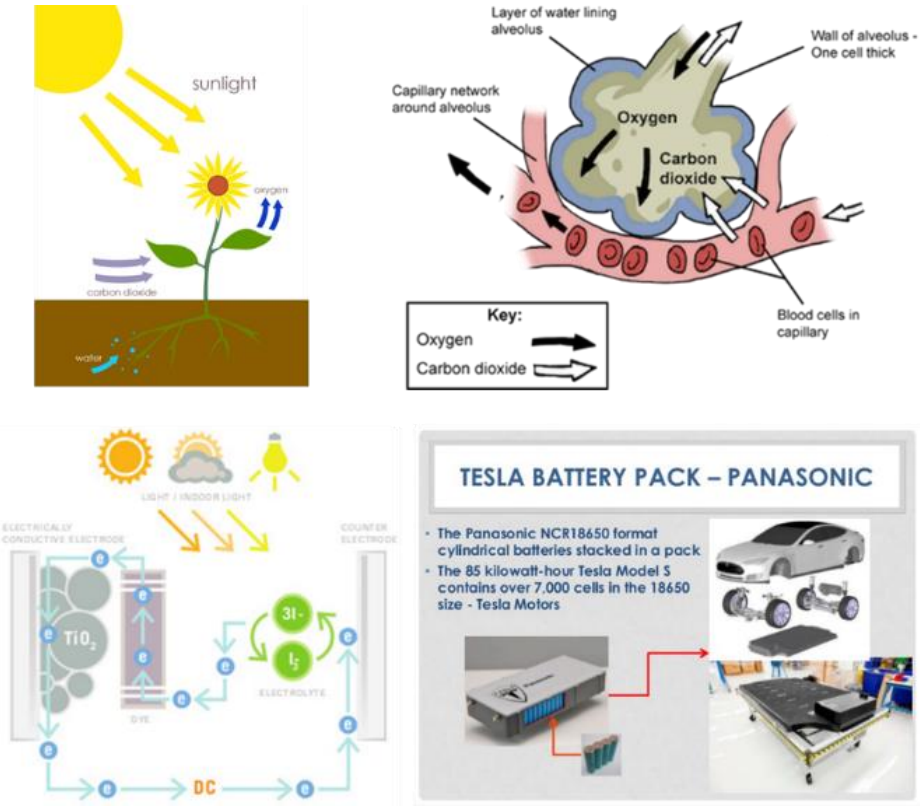

Figure 2.1: Electrochemical reaction in life[50–52]

Research on electrochemical reaction began from the late 18th century and still attracts a lot of attention nowadays.[53,54] The main reasons are two: 1) Various phenomenon is directly or indirectly related with electrochemical reaction; 2) There are a lot of variations in electrochemical reaction, i.e. different conditions can provide different responses.

In early 1970s, scientists started to investigate the electrochemical reaction in biology. Among so may reactions, one of the most interesting topics is to study the electron transfer (ET) process in biological molecular, especially proteins. Measuring ET processes in molecules is critical to the understanding of many basic chemical and biological phenomena,[28,55–57] and directly relevant to applications in energy conversion, molecular electronics and biosensors.[58–61] For example, one of the most important example is the research on electron transport chain (ETC) in photosynthesis and respiratory. Along this chain, electrons have been transferred through different compounds via electrochemical reactions, coupling with proton transfer across the membrane which drives the ATP synthesis. Fig.2.2 depicts the ETC in mitochondria, which plays an important role in respiratory system. Complex I (NADH coenzyme Q reductase) received electrons from nicotinamide adenine dinucleotide (NADH), which is the product of citric acid cycle. Then the electrons will be transported to coenzyme Q (ubiquinone), to which complex II (succinate dehydrogenase) will also pass electrons. In next step, ubiquinone transfers electrons to complex III (cytochrome bc_1 complex) and then to cytochrome *c* (cyt *c*). Finally, Complex IV (cytochrome *c* oxidase) accepts the electrons via cyt *c* reduction, coupling with hydrogen ions to reduce molecular oxygen to water.[62] This is similar to the one in photosynthesis which is shown in left of Fig.2.2, the difference are the reaction complexes along the ETC.

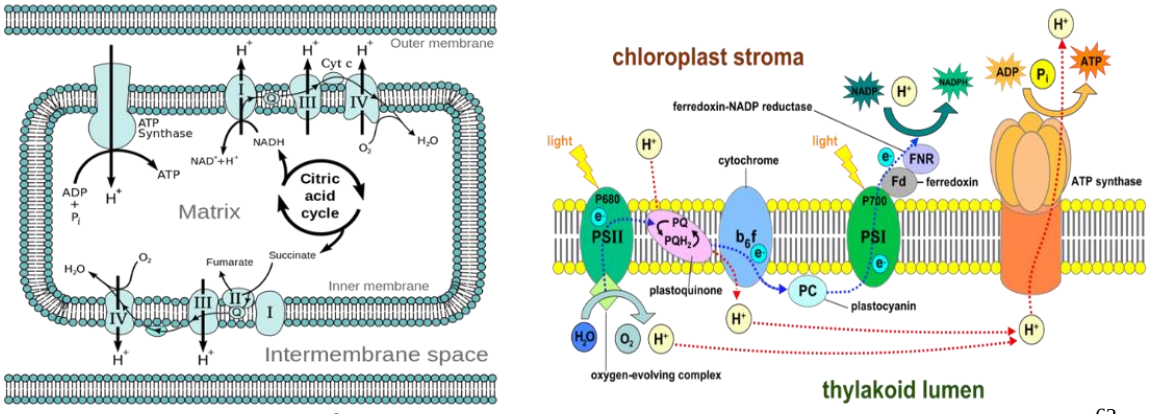

Figure 2.2: Electron transfer chain (ETC) in Mitochondria and photosynthesis system[62]

A key to ET is thermal fluctuations, including conformational changes in the molecules and polarization in the surrounding solvent molecules, which help bring energy levels of the donors and acceptors into alignment, and create transient molecular conformations with large electronic coupling between the donor and acceptor states.[63,64] Evidence has shown that conformational changes due to thermal fluctuations determine ET in the redox proteins, involving possibly proton-coupled and frictional control mechanisms in the ET.[65,66] However, conformational changes in proteins are fast, and distributed over a broad time range, which can be slower than milliseconds and as fast as picoseconds as shown in Fig.2.3.

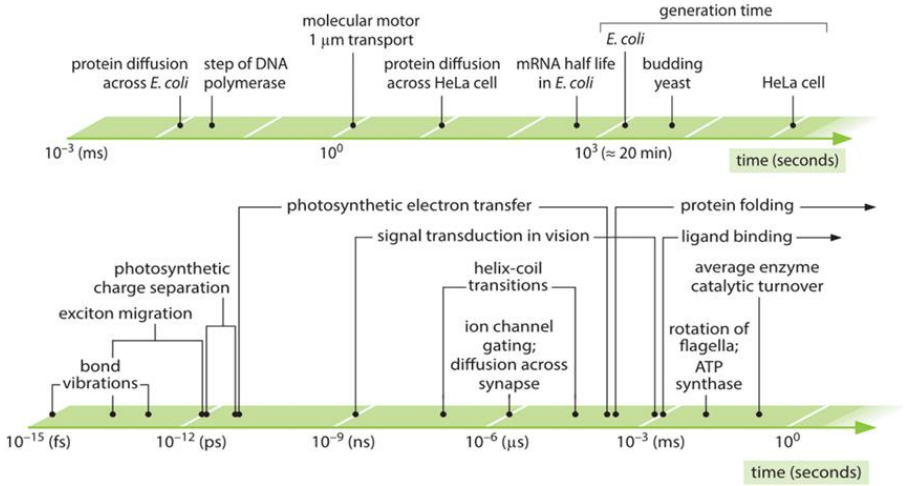

Figure 2.3: Different time scales of biological process[67]

To study the ET process, scientists have proposed the gold-organic tether-molecule system, which is an easy to realize, stable and reproducible system. The most important examples studied to date are redox molecules, such as redox proteins, adsorbed on the electrode. It has been proven that the mechanisms control electron tunneling between a molecular acceptor and donor, and between an electrode and a redox couple are similar. In an electrochemical system, the donor (or acceptor) is an electrode. By applying a potential to the electrode, one can control ET to or from the molecules on the electrode, and by measuring the current passing through the electrode one can determine the ET rate. This drives the birth of new fast electrochemical detection techniques.[56,57,68–71]

2.2 Ultrafast Detection Techniques

2.2.1 Pump-probe

Pump-probe, as an effective method to measure time-resolved spectroscopy, is widely used in detection of photosensitive materials. The basic setup is shown in Fig.2.4.[72] A femtosecond pulsed laser is spilt into two beams: one acts as pump pulse, which is used to excite the sample to excitation states at initial; the other one has a certain temporal delay to the pump and measures the absorption of the excited sample. The optical delay between the pump and probe pulse is determined by the length difference of the two light paths. Since light travels very fast, this optical delay could be very small, e.g. a 1 mm optical path difference could introduce a picosecond delay. By varying the optical delay line, transient signal at different states of the sample can be detected. The time-resolved spectroscopy can be obtained through combining the measurement results together, as shown in Fig.2.4.

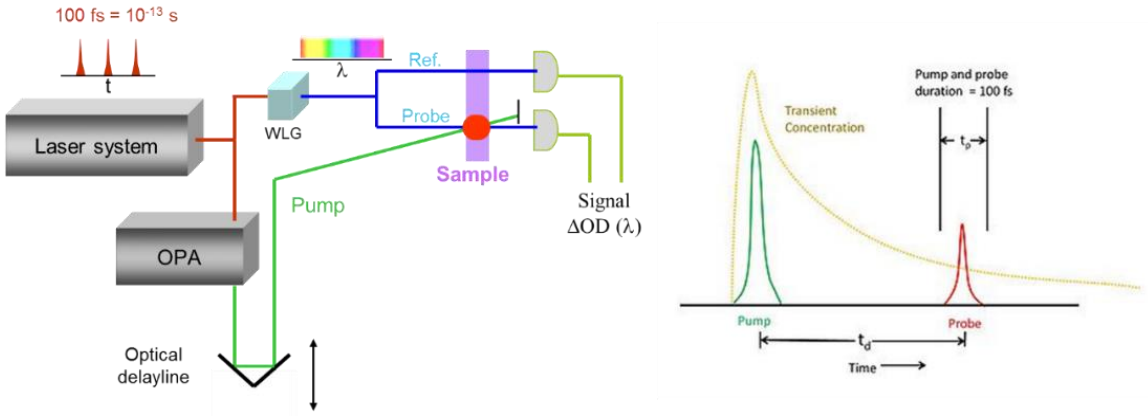

Figure 2.4: Schematic diagram of pump-probe instruments and theoretical response[72]

Pump-probe is widely used for detecting the electron transfer in photosynthesis because most of the processes involve light to triggering the signal. Those studies are focused on the photosynthetic reaction centers of purple bacteria, which allow a direct observation of photo reduced electron transfer (ET) since the functional reaction center (RC) can be separated from the light-collecting antenna systems and the absorption spectra of the bacterial chlorine chromophores show well-separated absorption bands, as shown in the Fig.2.5.[73]

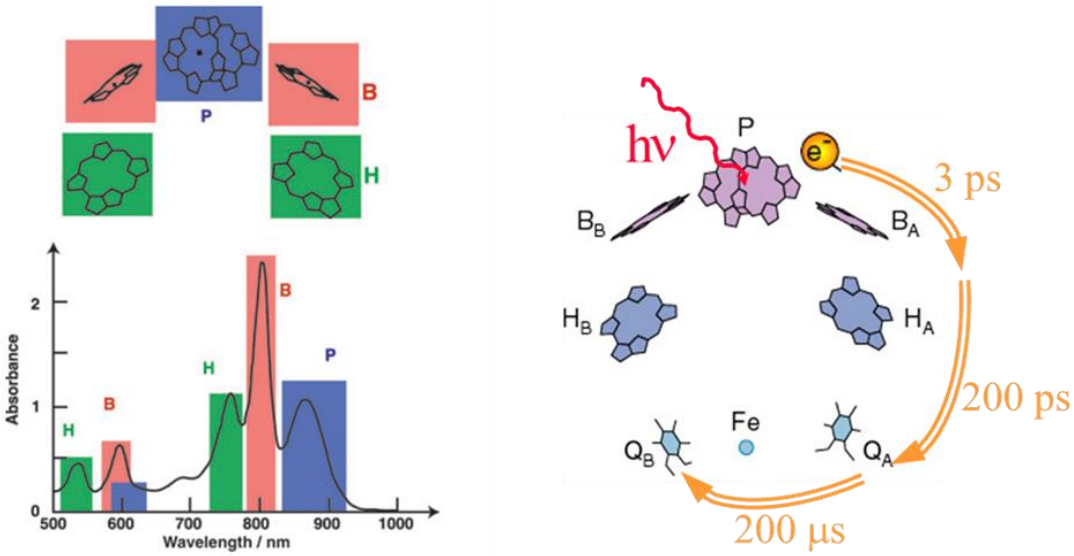

Figure 2.5: Time resolved process and spectroscopy of reaction center in purple blue measured by pump-probe technique[73]

Pump-probe is a powerful tool for measuring ultrafast photo-induced process; however, it is unavailable for the electrochemical reaction that cannot be triggered by light. Therefore, following electrical reaction method have been invented for this purpose.

2.2.2 Cyclic Voltammetry and SECM

Cyclic voltammetry (CV) is one of the conventional electrochemical methods to detect the properties of electrochemical reactions. While the potential is scanning back and force with linear increase/decrease, the current of the working electrode is measured.[74] Usually, if the system is reversible, there will be different current peaks when scanning the voltage in different direction, which indicates the reduction and oxidation (Fig.2.6).

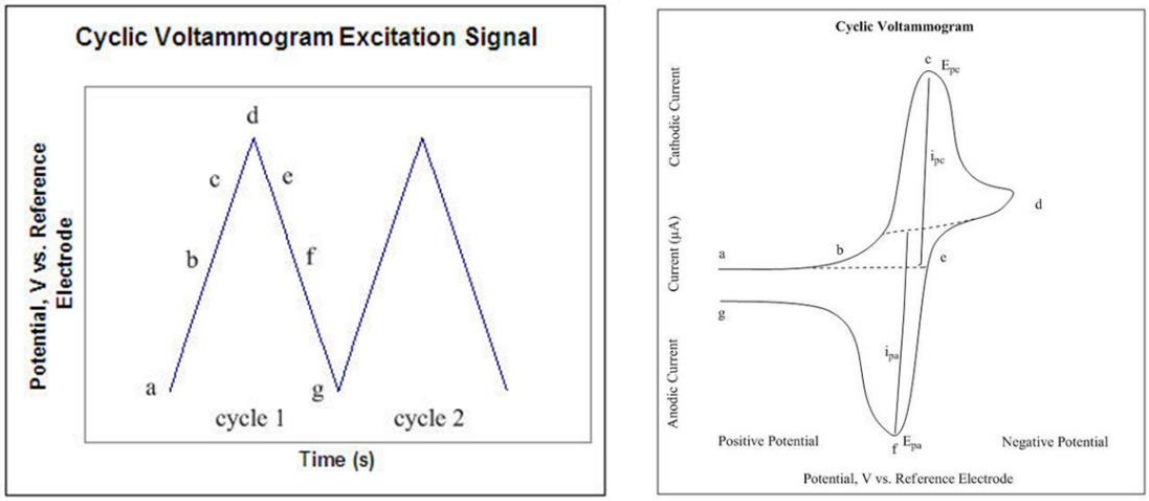

Figure 2.6: Principle of cyclic voltammetry. Left: scanning voltage to get current response; right: example of cyclic voltammetry response, the peak represents where the reduction and oxidation happen.[74]

The current of the electrochemical reaction is different for different conditions. When the diffusion of the reactance is much slower than the electron transfer rate, the current will be dominant by the mass-transfer process, which can be expressed as[75]

$$i = \frac{nFD}{\delta} C \qquad (2.1)$$

where n is the number of electrons involved in reaction, F is the faraday constant, D is the diffusion coefficient, δ is the thickness of diffusion layer, and C is bulk concentration of reactance. If the diffusion is fast and could be neglected (such as rotating disk electrode and small electrochemical cell), the current can be expressed as the Bulter-Volmer equation[75]

$$i = i_0 \left\{ e^{\frac{\alpha_a nF\eta}{RT}} - e^{\frac{\alpha_c nF\eta}{RT}} \right\} \qquad (2.2)$$

Where i_0 is the electrode current density, R is the universal gas constant, η is overpotential, α_a and α_c are the electron transfer coefficient, which correspond to the electron transfer rate.

In traditional electrochemistry, macroelectrodes are used and the current response is usually diffusion controlled. In order to measure the electron transfer rate, microelectrodes and Scanning Electrochemical Microscopy (SECM) is applied. Certain voltage is applied between the working electrodes and microelectrode, and the species will be reduced/oxidized on microelectrode and then regenerated on the working electrode, making it a repeatable cycle. If the electron transfer from the working electrode to the solution is fast, the reduced/oxidized species will be quickly regenerated. Otherwise, the regeneration process will be slow.

Liu et al. have proposed a method of applying SECM to measure the electron transfer tunneling through organic tether which is the SAM layer on top of gold electrode.[76] The experiments were done in time scale much larger than the diffusion time, which they called ‘steady state measurement’, indicating the amplitude of current response actually depends on electron transfer rate. The model they proposed is shown in Fig.2.7.

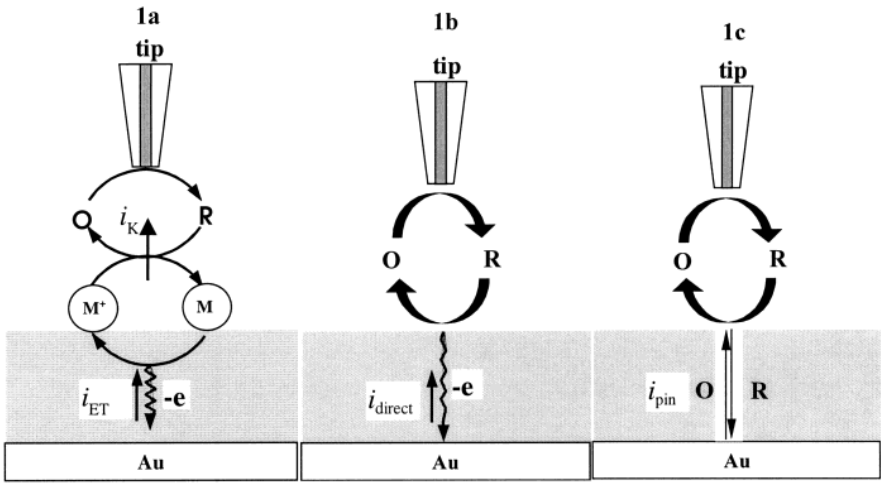

Figure 2.7: Different mechanism of electron transfer to the Au electrode[76]

Two methods were proposed: 1) SAM layer is connected with redox molecules; 2) only SAM Layers. In case 1, three consecutive steps contribute to the signal: 1) mass transfer in the tip/substrate gap; 2) bimolecular ET between the mediator species and the monolayer-bound redox centers; 3) the electron tunneling through the SAM layer, as depicted in Fig.2.7(a), which may provide some positive feedback to the system. In case 2, there is no reactant on the layer, and the electron will tunnel through SAM layer (Fig.2.7(b), negative feedback) and the pinhole (Fig.2.7(c)) to the working electrode. By fitting the approach curve, electron transfer rate of 10^8 s^{-1} could be measured.

SECM is a good approach to measure the kinetics of electrochemical reaction, since it avoids the influence of double layer charging. However, this does not provide intuitional evidence, i.e. the transient signal, since the experiment is done in the steady state and need to build a complicated theoretical model to extract the electron transfer rate.

2.2.3 Chronoamperometry

Chronoamperometry is an electrochemical technique in which step potential (which induce the faradaic processes occur) is applied to working electrode and current is recorded as a function of time.[75] Chidsey et al. employed this method to detect the electron transfer through organic tether.[55,69] Schematic view of their setup is shown in Fig.2.8. Redox center (ferrocene) is connected to the gold microelectrode through organic molecule chain. The microelectrode is contacted with the electrolyte through an μm size pipette. An silver wire is inserted into the electrolyte as the reference electrode.

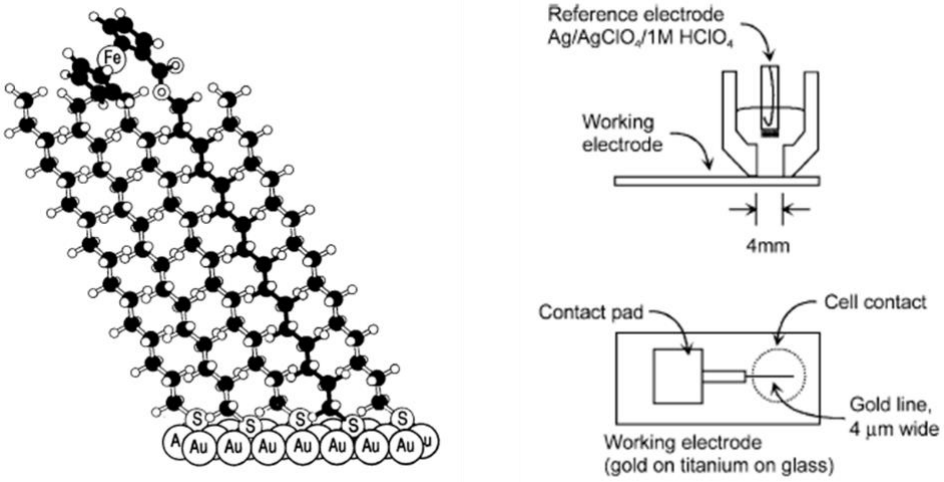

Figure 2.8: Configuration of using Chronoamperometry to detect electron transfer rate[55,69]

The double layer charging/discharging constant of this system can be expressed as[69]

$$RC \cong \frac{\rho}{\pi L}\ln\left(\frac{2L}{W}\right) * \frac{\varepsilon\varepsilon_0 LW}{d} = \frac{\rho\varepsilon\varepsilon_0 W}{\pi d}\ln\left(\frac{2L}{W}\right) \qquad (2.3)$$

where ρ is the resistivity of the electrolyte, ε and ε_0 stand for the permittivity for SAM layer and vacuum, L and W are the length and width of gold microelectrode, respectively. Calculation of the 4 μm electrode indicates an ultrafast charging rate 1.6×10^8 s^{-1}. By

applying a step potential using iterative control method to compensate the ohimc drop effect,[77] they could be able to measure the transient current signal about several hundred nanoseconds, as shown in Fig.2.9(c). The fastest rate they can measure is about 10^7 s^{-1}, which is limited by the signal to noise ratio of the detection circuit.

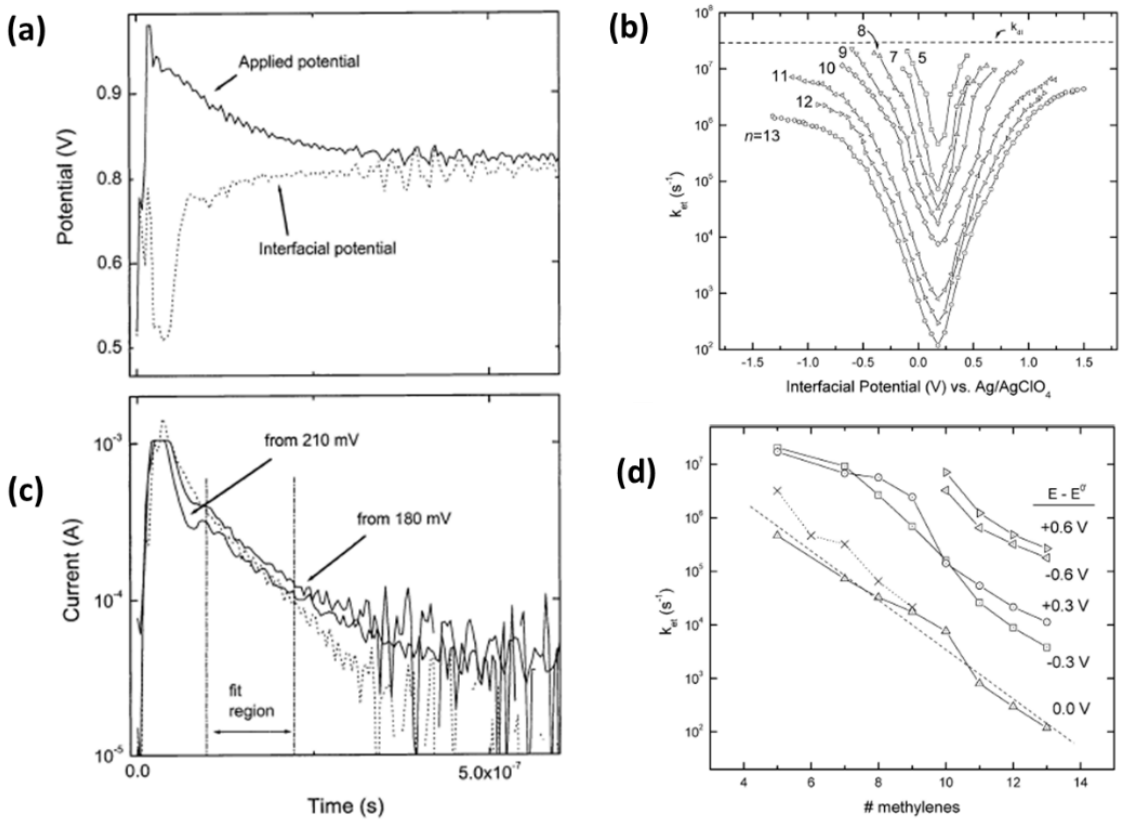

Figure 2.9: Measurement results of Ferrocene-SAM-Au system by chronoamperometry. (a) the step potential applied (iterative control method to compensate the ohimc drop effect); (b) the corresponding current signal; (c) electron transfer rate dependence of interfacial potential; (d) electron transfer dependence of the length of molecular chain.[69]

Chronoamperometry provides the intuitive physical picture to observe the electron transfer process; however, this method gets its limitation due to the balance for charging rate and signal strength. To get faster rate constant, we need smaller microelectrode, which is companied with the decrease of the current. Therefore, the feedback resistance (R_e in

Fig.2.10) needs to be larger to obtain enough signal to noise ratio, which will decrease the temporal resolution for measurement.

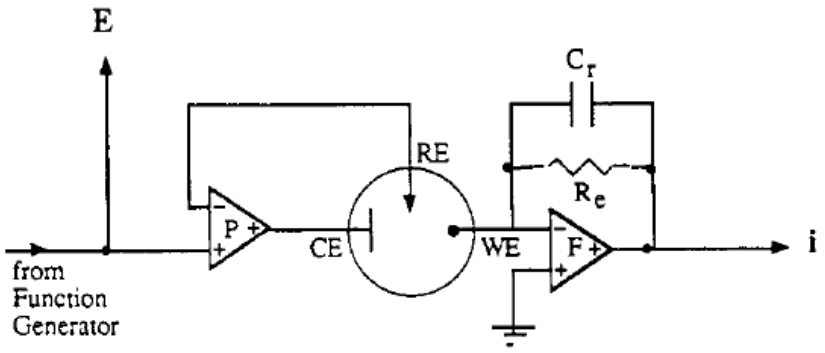

Figure 2.10: Schematic view of Potentiostat: the principle of measuring current response[75]

2.2.4 Indirect Laser Induced Temperature Change

To avoid the problem that we discussed in last section, scientists tried to figure out other ways to trigger the electrochemical reaction. Indirect Laser Induced Temperature Jump (ILIT) method was then been invented by Smalley et al.[56,68,78–80]

The ILIT setup is shown in Fig.2.11. A femtosecond pulse laser is used to apply a sudden temperature jump to the electrochemical cell. Potentiostat is used to hold the potential and provides the current that the electrochemical cell needs. Acoustic sensor is used to extract the temperature information of the cell, and the whole cell is adiabatic. The open circuit voltage is measured by the exterior amplifier board, which has a nanosecond time resolution.[78]

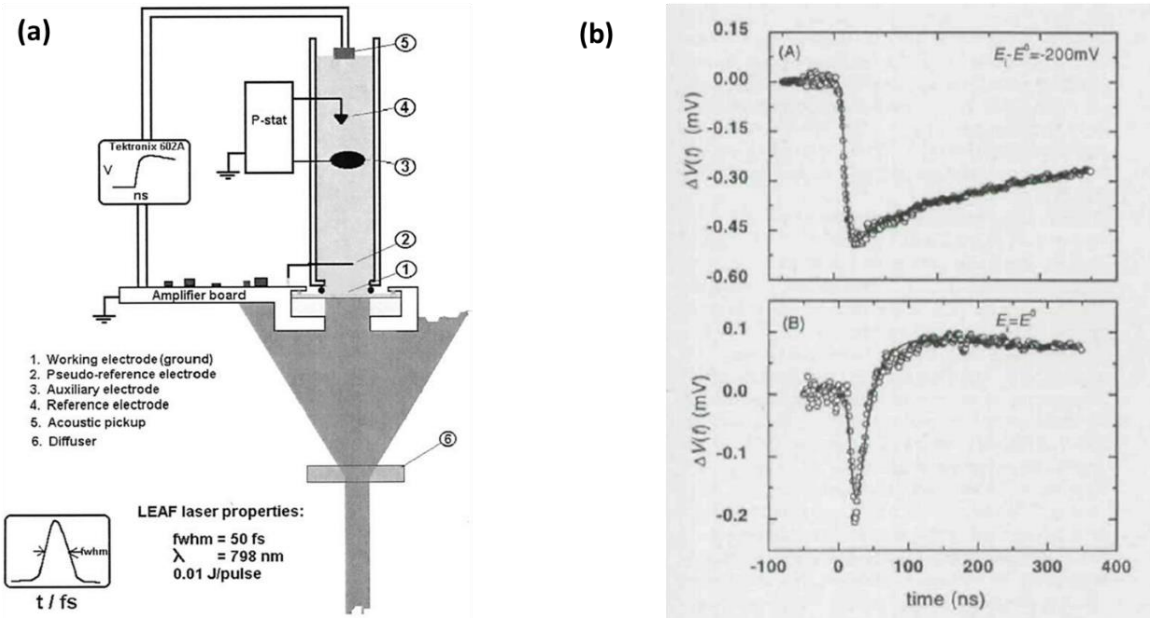

Figure 2.11: Principle of ILIT method. (a) schematic diagram of ILIT setup; (b) Response of ILIT.[78]

The measurement consists of three major steps: 1) the electrochemical cell is first hold at equilibrium by the Potentiostat; 2) the pulsed laser shines to the gold working electrode and initiate an instaneous temperature change of the system, which will break the equilibrium; 3) the system gradually goes back to equilibrium, and the corresponding response of the open-circuit voltage as the function of time will be recorded and used to extract the information of electron transfer. The modeling of the system is described somewhere else. The open circuit voltage can be simplified as[78]

$$\Delta V_{OC} = \Delta T_{step}[A + B(1 - e^{-k_m t})] \qquad (2.4)$$

where A, B is the parameter that could be calculated as[78]

$$\mathrm{A} = \left(E_{pzc}^{i} - V_{oc}^{i}\right)\frac{d\ln[C_i]}{dT} + \frac{dE_{pzc}}{dT} + \frac{dV_{TJ}}{dT}$$

$$B = \frac{1}{C_i^i}\frac{d\sigma_M}{dT} = \frac{\frac{dE^\circ}{dT} + \frac{V_{oc}^i - E^{o,i}}{T^i} - \left(E_{pzc}^i - V_{oc}^i\right)\frac{d\ln[C_i]}{dT} - \frac{dE_{pzc}}{dT}}{1 + \frac{k_B T^i C_i^i}{e^2}\left(\frac{1}{\Gamma_{ox}^i} + \frac{1}{\Gamma_{red}^i}\right)} \quad (2.5)$$

By fitting the recorded curve, the electron transfer rate can be extracted.

The ILIT methods measure the transient current signal and smartly avoids the problem of double layer charging and discharging. According to Smalley et al., since the charging/discharging process for large area electrode is slow, which is much larger than the time scale of measurement, there will be quite small contribute on the open-circuit voltage change for this part, which indicates the faradic process is dominant.[68,79] However, this configuration is too complicated for people to setup and use, since it is hard to accurately control and fast measure the temperature, and the theoretical model to extract the parameter is kind of complicated.

2.3 Measurement of Cytochrome c ET

Most biological reactions of redox proteins happen at the membrane/solution interface. As a good system to mimic the charge distribution in that condition, redox proteins absorbed on SAM coated electrodes are proposed. Most of these studies are focused on cytochrome c, a protein that carries electrons and reduce oxygen to water, because of its well-known structure and dynamic properties. This will help to understand fundamental parameters that governs the ET process in biological activities. During recent 20 years, two major methods are developed for ET detections in cytochrome c: one is based on impedance spectroscopy, and the other one is to measure the transient ET process.

Feng et al. first proposed the impedance spectroscopy approach.[71,81] They applied ac potential modulation to the system, which triggered the ET process of cytochrome c. The

absorption of cytochrome c species will be recorded during the process. The absorption could be expressed as[71]

$$A_{ac}(t) = (\epsilon_{red} - \epsilon_{ox})\Gamma_t f(t) = (\epsilon_{red} - \epsilon_{ox})\Gamma_t \int i_{ac}^F dt \qquad (2.6)$$

where ϵ_{red} and ϵ_{ox} are the absorption coefficient of reduced and oxidized species, Γ_t is the total amount of cytochrome c, i_{ac}^F is the current of faradic process, respectively. According to Randel's circuit model, i_{ac}^F for impedance measurement is given by[71]

$$\begin{cases} i_{ac}^F = Y_F E_{ac}^F \\ Y_F = \frac{1}{R_{ct} \| C_a} = \frac{1}{R_{ct} + \frac{1}{j\omega C_a}} \end{cases} \qquad (2.7)$$

where R_{ct} and C_a are the resistance and capacitance of the faradic process, E_{ac}^F can be treated as the modulations potential if the solution resistance is small. By combining Eq.2.6 and Eq.2.7, we can easily extract the R_{ct} and C_a from the frequency response curve. The ET rate could be calculated with the Butler-Volmer and Nernst equations, which could be simply as[71]

$$k_s = \frac{1}{2R_{ct}C_a} \qquad (2.8)$$

This method smartly avoids measuring the double layer charging, which happens simultaneously with ET of cytochrome c. Murgida et al. further developed this approach by using Surface Enhanced Raman Spectroscopy (SERS), so they could measure the different state of cytochrome c during ET process with enhanced sensitivity.[66,82,83] Avila et al. and Wei et al. applied the method to investigate the ET of cytochrome c-SAM-gold system by varying the SAM layer length.[70,84] It was first assumed that cytochrome c has a fast ET process and the ET rate should increase when SAM layer thickness decreases, because the distance from heme to lysine group of cytochrome c is short. Interestingly,

almost all the groups found that the ET rate would not continue decrease after shorting the SAM layer to less than 6 methylene groups. This indicates there is conformational gating during the ET process. To further validate their conclusion, Khoshtariya et al. used this method to observe ET of cytochrome c in different buffer solutions which may influence the conformational changing rate.[85] They test the buffer with different viscosity, different Ph and different proton hydrate, and proved that the conformational fluctuation limits the ET rate of the system.

The impedance spectroscopy is able to measure the electron transfer rate of the cytochrome c, but it does not provide any transient information of the process. Scientists were curious about how the conformational change happens. T. Pascher and C.-K. Chan et al. monitored the conformational gated ET process by shining pulsed laser on the sample to trigger the ET process and measured the tryptophan fluorescence intensity (indicate the structure change).[28,57] This method helped to determine the different time scale of cytochrome c folding during the ET process; however, they modified the cytochrome c with a Ru^{2+} complex label for reaction initialization and this may affect the measurement. Label free transient measurements have been proposed by both Yuan et al. and Boussaad et al.[86,87] They applied a step potential to the system and used circular dichroism and surface plasmon resonance imaging to monitor the process; however, their temporal resolution is limited to millisecond to seconds because of slow potential trigger. It was observed by labeled method and theoretical estimation that the time scale of cytochrome c conformational gating actually distributed in a wide time scale range, from sub-microseconds to seconds. Therefore, a novel label free approach with high temporal resolution and sensitivity is needed to measure this transient ET process.

2.4 Fast Plasmonic Electrochemical Detection: Setup and Principle

According to the introduction in section 2.2, one limiting factor for fast electrochemical measurements is the response time of an electrochemical cell, which is determined by the capacitance and resistance of the system, including electrode and electrolyte. This response time usually scales linearly with the dimension of the electrode (e.g., width of a line electrode).[61,69,75] By decreasing the electrodes to the micron-scale, sub-μs electrochemical measurements have been demonstrated. Fast electrochemical measurements require not only fast time response, but also a sufficient signal to noise ratio in the data. Traditional electrochemical approach measures the total electrochemical current, which scales with the electrode area, so the signal to noise ratio may be compromised when one improves the response time by reducing the electrode size.[75] This is especially the case when the coverage of the adsorbed redox species on the electrode is low, and the ET current is small compared to the capacitive charging current in the background. For these reasons, previous ET rate measurements of redox proteins are usually based on cyclic voltammetry (CV), which determines an effective ET rate by measuring the separations between the oxidation and reduction peaks vs. potential sweep rate.[78,88–90]

Here we achieve fast detection of electron transfer processes using a plasmonic imaging method combined with microfabricated microelectrodes. The principle of the method is to convert an electrochemical current into a plasmonic signal, and then detect it optically with ns optical detection speed. Like a traditional electrochemical measurement, the plasmonic method measures both capacitive charging and ET processes, but the charging contribution to the plasmonic signal is relatively small, which makes it easier to

study ET than the traditional method. Furthermore, the plasmonic signal does not scale with the electrode area,[8] allowing us to reduce the electrode size without sacrificing the signal to noise ratio. Using this approach, we measure ET in a redox protein (cytochrome c) adsorbed on a microelectrode, and study conformational gating of the ET over a broad time range.

2.4.1 Detection Principle

We have demonstrated plasmonics-based electrochemical microscopy (P-ECM) to image local electrochemical reactions,[7,8,91–93] but its temporal resolution is limited by the frame rate of the imager (CMOS or CCD) and response time of the electrochemical cell. To study fast ET in redox molecules, the first task is to develop fast P-ECM. We build a system with fast electrochemical triggering, fast detection and high signal to noise ratio (SNR) even at small electrochemical current. To realize, we use microfabricated electrodes, and a fast photodiode in parallel to the imager to detect fast electrochemical processes (Fig.2.12). For redox molecules adsorbed on an electrode, the image intensity (I_{SPR}) by P-ECM is related to ET current density (J) by[94]

$$\frac{dI_{SPR}(x,y,t)}{dt} = \mathrm{B}\frac{\alpha_{ox}-\alpha_{red}}{\mathrm{nF}}J(x,y,t) \qquad (2.9)$$

where B is a constant, α_{ox} and α_{red} describe the optical polarizabilities of the molecule in the oxidized and reduced states, respectively. In principle, the difference between α_{ox} and α_{red} could arise from the different electronic states of the reduce and oxidized species, which is shown as distinct absorption bands between 545-555 nm in the optical absorption spectra for cytochrome c.[95–97] However, in the present work, the incident light wavelength is 660 nm, which is far away from the absorption bands, so this contribution is small. A

more dominant contribution to the difference between α_{ox} and α_{red} is the conformational changes of the redox molecules associated with ET. We note that the measured plasmonic signal scale with current density, rather than current, as shown by Eq. 2.9, so it does not decrease with the size of the electrode. This is in contrast to the traditional electrochemical methods that measure current (rather than current density), which scales linearly with the electrode area, and thus decreases when one attempts to reach fast electrochemical response by reducing the electrode size.

P-ECM also measures capacitive (double layer) charging current density, given by

$$\frac{dI_{SPR}(x,y,t)}{dt} = \frac{1}{\alpha} J_d(x,y,t) \qquad (2.10)$$

where α is a constant, which can be calibrated experimentally or calculated with models.[41,91] As we will show later, $1/\alpha$ in Eq.2.10 is small compared to B$\frac{\alpha_{ox}-\alpha_{red}}{\mathrm{nF}}$, so P-ECM provides suppression of the background capacitive charging current, which favors the detection of ET current.

2.4.2 Experiment Setups

Fig.2.12(a) is a schematic illustration of the fast P-ECM setup, including an inverted microscope (Olympus IX81) equipped with a high numerical aperture oil-emersion objective.

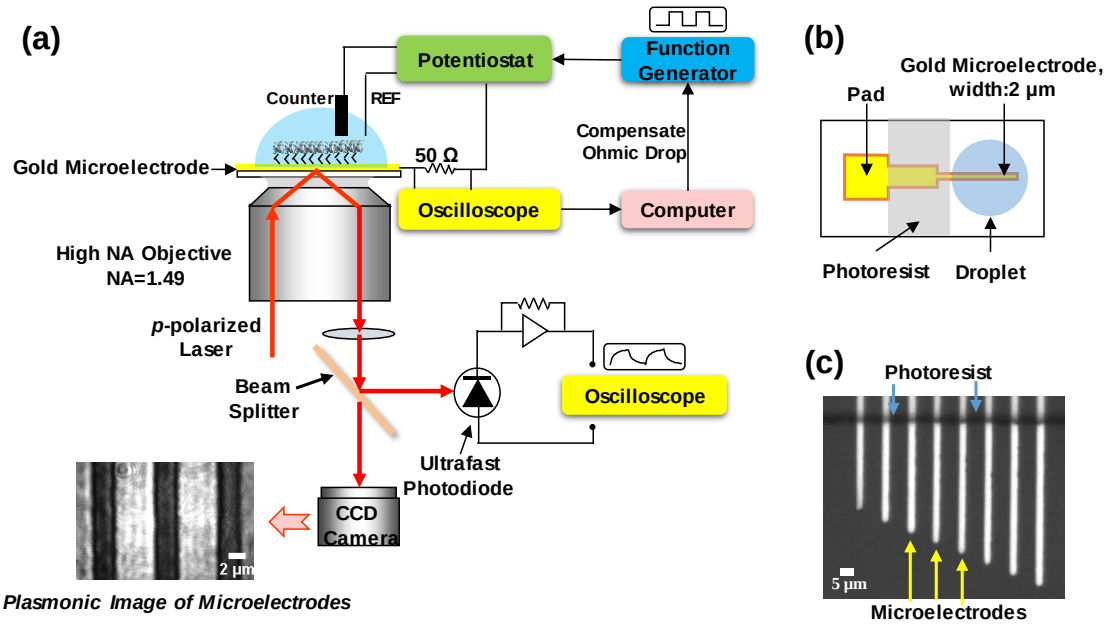

Figure 2.12: Fast P-ECM with ultrafast optical detection and miniaturized microelectrodes. (a) Optical setup including gold microelectrodes in an electrochemical cell mounted on the objective of an inverted microscope, p-polarized laser to excite surface plasmons in the microelectrodes, and detection of the plasmonic signal with a CCD camera and fast avalanche photodiode (3 ns) simultaneously. Redox proteins are immobilized on the microelectrodes, and the electron transfer reaction of the proteins is studied by controlling the microelectrode potential with a homemade Potentiostat and recording the transient electrical current with an oscilloscope connected to a computer. (b) Schematic of one microelectrode, showing a bonding pad for electrical connection to the Potentiostat, and photoresist coating for blocking most of the microelectrode area to the electrolyte. (c) Optical microscopy image of a microelectrode chip, consisting of 8 parallel microelectrodes with different lengths (30-50 µm).

Collimated p-polarized laser (Coherent, OBIS FP 660LX, wavelength of 660 nm and power of 60 mW) was directed via the objective to excite surface plasmons in the microelectrodes. Light reflected from the surface was collected by the same objective, and then split into two paths, one directed to a CCD imager, and the second to an ultrafast avalanche photodiode (Edmund Optics, 1.0 mm UVVIS (200-1000 nm), Si APD). A three-electrode system (the gold microelectrode as the working electrode, an Ag/AgCl reference electrode and a platinum coil counter electrode) was used in the study. The potential of microelectrodes was controlled with respect to the Ag/AgCl wire with a Potentiostat

(homemade) connected to a function generator for creating potential steps for chronoamperometry (Agilent 33521A, arbitrary wave generator). A 50 Ω resistor was connected in series with the electrochemical cell to measure the current. Oscilloscope (Tektronics, DPO2014, 100 MHz bandwidth, 1 GS/s sampling rate) was used to collect both fast plasmonic signal and electrical current. Ohmic drop was compensated using the method described in literature.[69,77]

In order to observe the ultrafast change of the SPR intensity, we build an ultrafast photodetector. We use an avalanche photodiode which has 1 ns response time as the light sensor, and biased voltage is applied in order to amplify the signal. The schematic diagram and the PCB circuit board made in our lab are shown in Fig.2.13. To achieve ultrafast detection speed, we use a small feedback resistor which is equal to 200 Ω. Combining with the capacitance of the photodiode, which is usually 10 to 20 pf, the response time will be less than 1 ns considering the parasitic parameters. Fig.2.14 shows the response time of the avalanche photodiode by an ultrafast laser modulation (1 ns rise/fall time). The time constant of photodiode and detection circuit is ~3 ns, which is consistent with our estimation.

We detected the electrochemical current by electrically connecting a 50 Ω resistor to the working electrode and monitoring its voltage (Fig.2.12). To ensure this resistor does not affect the detection speed, we monitored P-ECM with and without the resistors and found no significant difference (Fig.2.15).

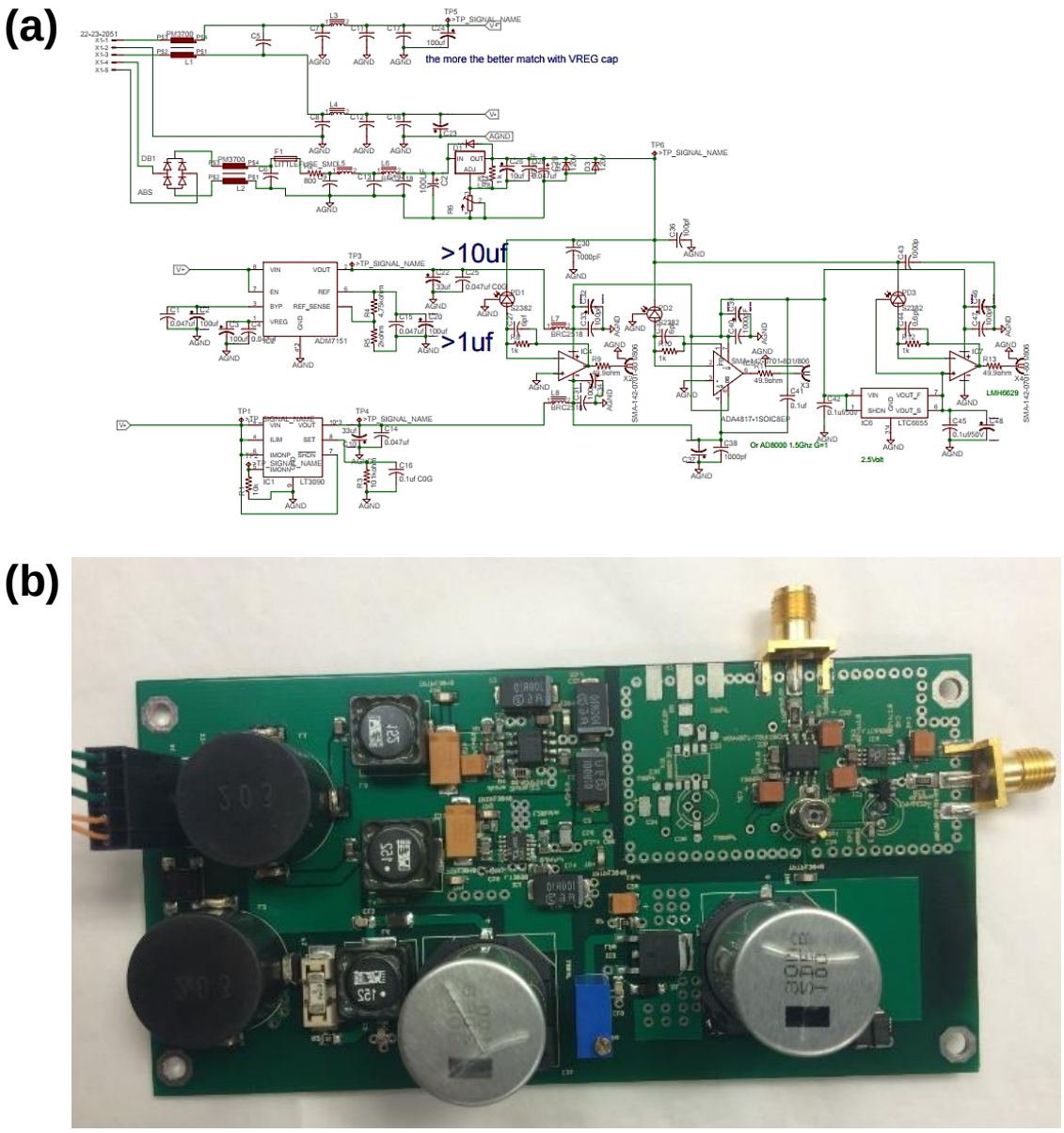

Figure 2.13: Photodetector circuit. (a) Schematic view of DC coupled photodetector; and (b) real object.

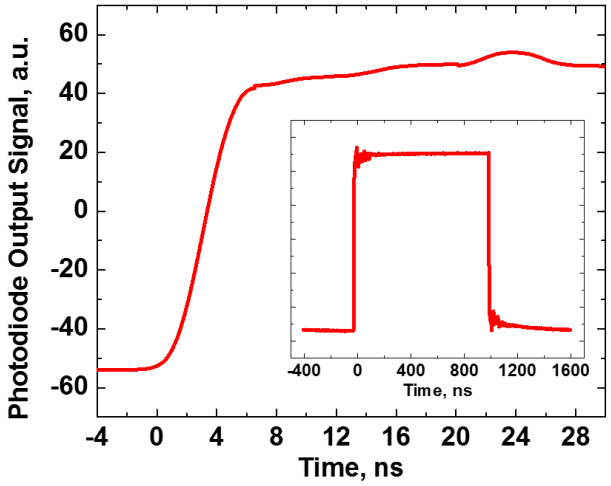

Figure 2.14: Measured response time of the ultrafast photodiode used for fast P-ECM. Inset: Photodiode output over 2 µs time window.

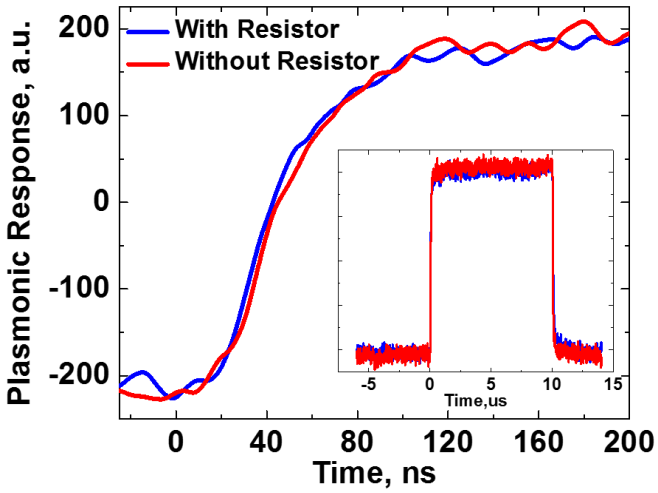

Figure 2.15: Plasmonic responses of a bare gold microelectrode with (blue) and without (red) a 50 Ω resistor connected in series for current measurement. Inset: Plasmonic responses over 20 µs. The experiments were performed in 3.75 M $NaClO_4$, and the potential was stepped from -0.3 V to +0.3 V.

Using the previous ultrafast photodiode detection, a response of light intensity changes as fast as ~3 ns can be detected (Fig.2.14). However, fast P-ECM also requires one to change the electrode potential rapidly, which is limited by the charging time constant,

R_sC_{DL}, of the electrochemical cell, where R_s is the solution resistance and C_{DL} is the surface capacitance of the electrode. Both R_s and C_{DL} depend on the dimensions (width and length) of the electrode, and R_sC_{DL} typically decreases with the dimensions.[98] Therefore, one way to shorten the charging time is to decrease the electrode dimensions.[98]

In the present work, we tested gold microelectrodes with various dimensions fabricated with optical lithography and found that the microelectrode of 2 μm wide and 50 μm long provides the best result. Smaller microelectrodes did not lead to significantly faster responses because stray capacitance arising from the Potentiostat circuit and wiring of the Potentiostat to the microelectrodes became the limiting factor of the time constant of the system (electrochemical cell, wiring and detection system).

2.4.3 Ohmic Drop Compensation

To make sure a square wave is applied on the redox protein and avoid the effect of electrolyte resistance, we followed the method reported in literature to compensate the ohmic drop on the electrolyte.[69,77] We first applied a square wave potential to the electrochemical cell and measured the current response, from which we determined the ohmic drop, and added a correction to the applied potential via the arbitrary waveform function generator. We iterated the same process to achieve ensure fastest application of the interfacial potential (Fig.2.16). The detailed workflow of our algorithm is described in Fig.2.16(d).

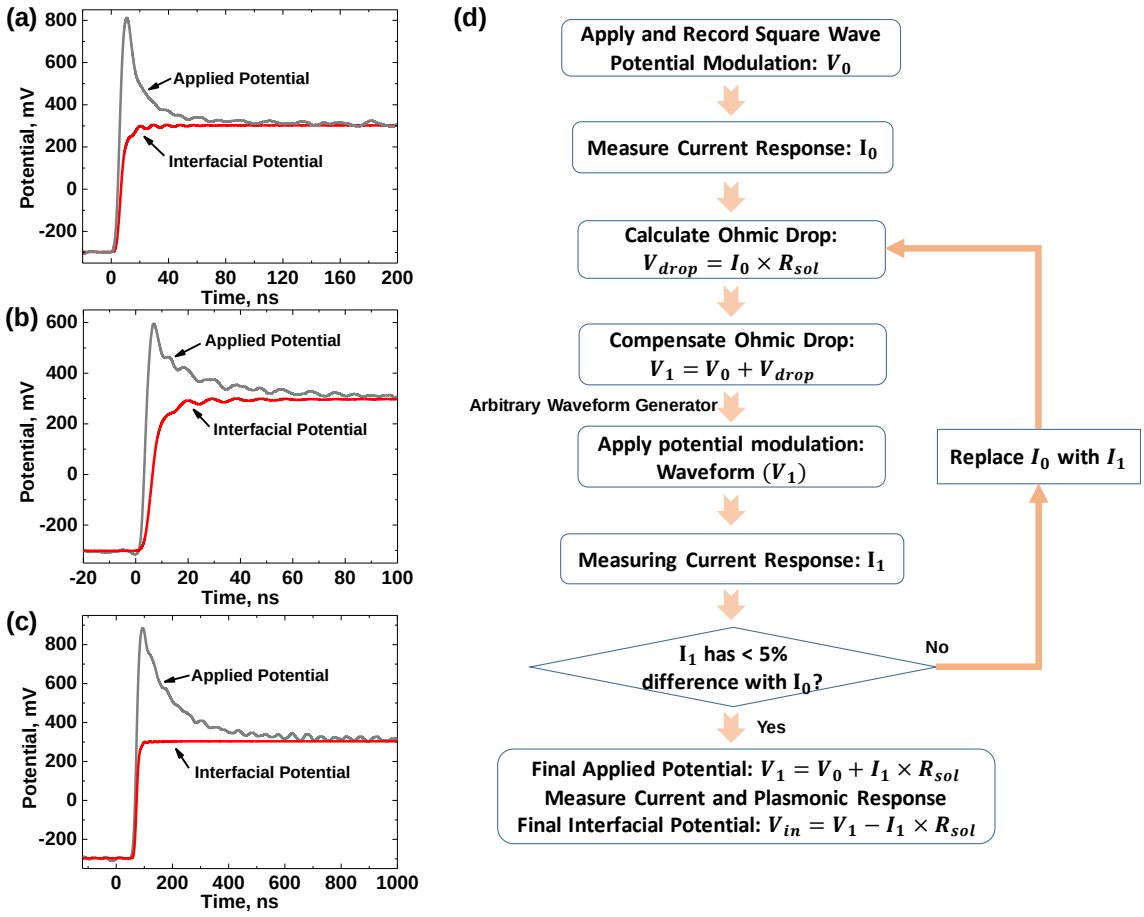

Figure 2.16: Applied potential waveform (grey) and actual interfacial potential waveform (red), of a bare gold microelectrode in 3.75 M $NaClO_4$ (a), 3-MPA modified gold microelectrode in 3.75 M $NaClO_4$ (b), and 3-MPA modified gold microelectrode in 70 mM PBS (c). (d) Workflow showing the compensation of the ohmic drop, where R_{sol} is the solution resistance.

2.4.4 Evaluation of the System Response Time

We studied the electrochemical process using chronoamperometry, which stepped potential to a preset value to trigger oxidation (or reduction) of the adsorbed molecules, and monitored the electrochemical current via both the traditional electrical and P-ECM methods simultaneously over time. To evaluate the response time of the system, including the electrochemical cell and P-ECM detection system, we measured the charging and

discharging processes in 3.75 M $NaClO_4$ electrolyte. In each case, the electrode potential was initially held at –0.3 V (vs. Ag/AgCl), and then stepped to +0.3 V and held at +0.3 V for 1 μs before stepping back to –0.3 V, during which the electrochemical response was monitored with the electrical and P-ECM methods. The time constants from the plasmonic and electrical measurements are both ~35 ns for a bare gold microelectrode (Fig.2.17(a)). In contrast, the time constants for the 3-MPA (3-Mercaptopropionic acid) modified microelectrode are ~7 ns (Fig.2.17(b)), which is 5 times smaller than that for the bare gold microelectrode because of the decreased interfacial capacitance (Fig.2.18).

In the tests discussed above, concentrated electrolytes were used to reduce the solution resistance (Rs). However, to study cytochrome c adsorbed on the 3-MPA modified microelectrode, the electrolyte was replaced by 70 mM PBS, which was necessary because concentrated electrolytes would cause cytochrome c to desorb from the microelectrode.[70] In 70 mM PBS, the charging time constant was found to be 100 ns, because of the increased electrolyte resistance (Fig.2.17(c)). This sub-μs time constant still represents one of the fastest measurements of ET in cytochrome c and could measure ET rate as fast as 10^7 s^{-1} (Fig.2.19, Table 2.1).

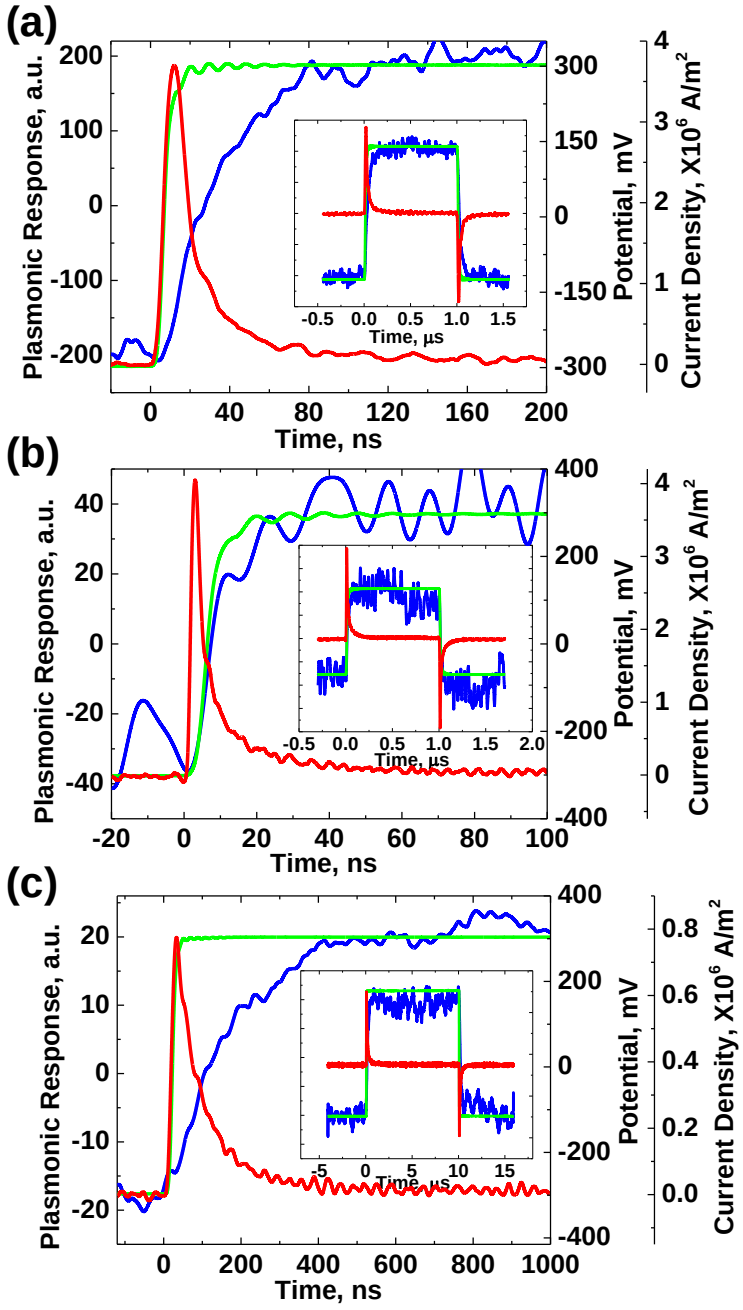

Figure 2.17: Time responses of P-ECM (blue), electrical current (red) and potential (green) under different conditions. (a) A bare gold microelectrode in 3.75 M $NaClO_4$. (b) A 3-MPA modified microelectrode in 3.75 M $NaClO_4$. The oscillations in the plasmonic response (blue) are due to noise in the laser. (c) A 3-MPA modified gold microelectrode in 70 mM phosphate buffered saline (PBS). Insets in (a-c) show the corresponding time responses over wider time windows. In (a) and (b), the electrode potential was varied between -0.3 V and +0.3 V at 500 kHz, and in (c), the electrode potential was varied between -0.3 V and +0.3 V at 50 kHz.

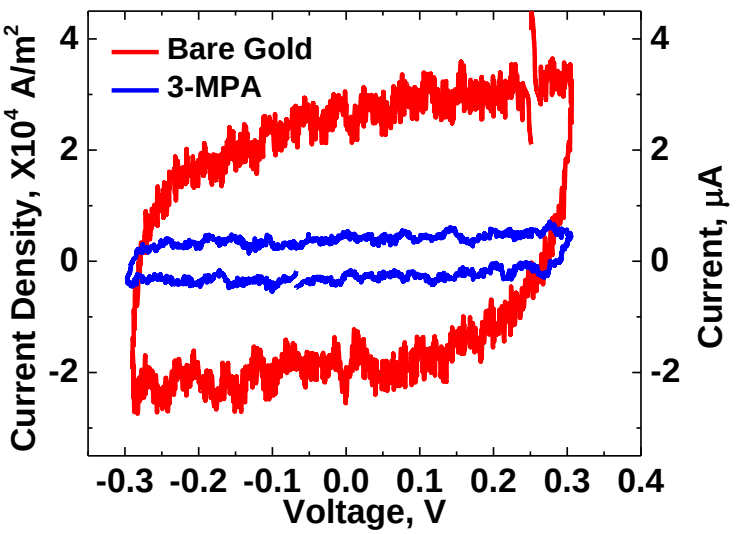

Figure 2.18: Cyclic voltammetry of bare (red) and 3-MPA modified (blue) gold microelectrodes. The experiments were performed in 70 mM PBS with a potential scanning rate of 60 kV/s from -0.3 V to +0.3 V.

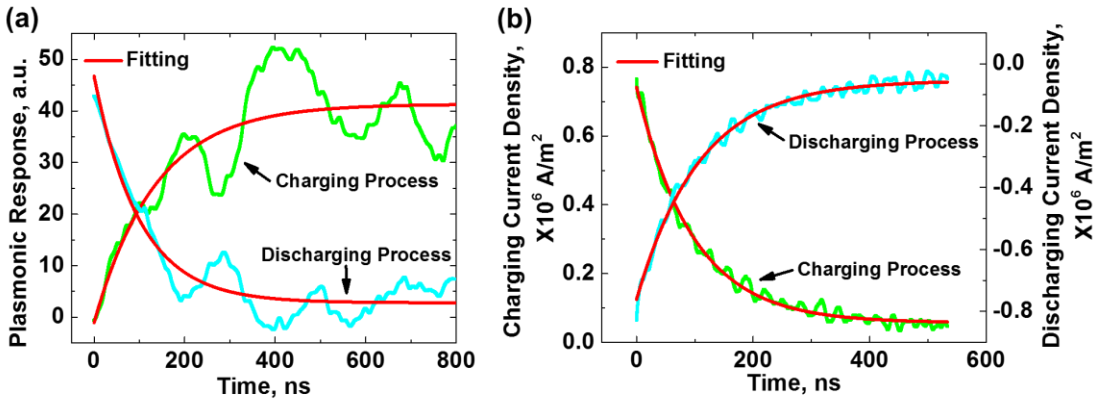

Figure 2.19: Charging (green) and discharging (cyan) kinetics of a 3-MPA modified gold microelectrode in 70 mM PBS measured by P-ECM (a) and electrical (b) methods.

Table 2.1
Time Constants for Charging/Discharging of a 3-MPA Modified Microelectrode in 70 mM PBS Measured by P-ECM and Electrical Methods

	Charging Process	***Discharging Process***
P-ECM	131.58 ns	99.64 ns
Electrical Method	133.33 ns	98.73 ns

2.5 Materials and Methods

Chemicals. Sodium perchlorate ($NaClO_4$), 3-MPA, purified bovine heart cytochrome c, trifluoroacetic acid (TFA, ReagentPlus®) and acetonitrile were obtained from Sigma-Aldrich. The 3.75 M $NaClO_4$ and 5 mM 3-MPA aqueous solutions were prepared from deionized water (Milli-Q, Millipore Corp.). Phosphate buffered saline (Corning cellgro, 154 mM NaCl, 5.6 mM Na_2HPO_4, and 1.1 mM KH_2PO_4) was diluted with deionized water to 70 mM. 50 μM cytochrome c solution was made by dissolving cytochrome c in the 70 mM PBS buffer. Two solvents, 0.1% TFA in DI water and 0.1% TFA in acetonitrile, were prepared and filtered for high performance liquid chromatography (HPLC) and absorption spectrum analysis.

Microelectrodes preparation. BK-7 glass slides were cleaned by acetone and then followed by deionized water. Gold microelectrodes were fabricated on each glass slide by photolithography with the following procedures: patterning the glass surface with photoresist, depositing gold on the patterned surface using thermal evaporation (Edwards II thermal evaporator), and then lifting off of the photoresist layer. After fabrication of the microelectrodes, SU-8 2007 photoresist (purchased from MicroChem) was spin-coated on top of the microelectrodes (500 rpm for 10 seconds followed by 2000 rpm for 30 seconds, layer thickness ~7 μm). Photolithography was then applied to open only the portion of the microelectrodes used for ET reaction study (lengths of exposed microelectrodes are 30-50 μm), as shown in Figs.2.12(b) and (c).

Microelectrodes modification. The microelectrodes were dipped in 5 mM 3-MPA solution for 2 hours, and then rinsed by deionized water repeatedly to remove excess 3-MPA. The microelectrodes were then brought into contact with 50 μM cytochrome c to

allow adsorption of cytochrome c to the 3-MPA surface (Fig.2.20(b)) for 4 mins. To remove cytochrome c in the bulk solution, the cytochrome c solution was replaced with 70 mM PBS for electron transfer reaction studies. P-ECM CVs (Fig.2.21(b)) were then performed to confirm the immobilized cytochrome c on 3-MPA surface.

3-MPA modification and cytochrome c adsorption on the microelectrodes. P-ECM can be operated in the conventional surface plasmon resonance imaging mode, which allows us to monitor and determine molecular adsorption processes.[42,95] Using this capability, we followed 3-MPA modification of the gold microelectrode by measuring the plasmonic image intensity vs. time (Fig.2.20(a)), and cytochrome c adsorption onto the 3-MPA modified microelectrodes (Fig.2.20(b)). The estimated coverage of cytochrome c is about 16% of a complete monolayer. Fig.2.20(a) shows the schematic of immobilized cytochrome c on the 3-MPA surface. Traditional and P-ECM CVs performed with 3-MPA modified electrodes (Fig.2.18) and cytochrome c immobilized electrodes (Fig.2.21) support good coverage of 3-MPA and immobilization of cytochrome c on the 3-MPA layer.

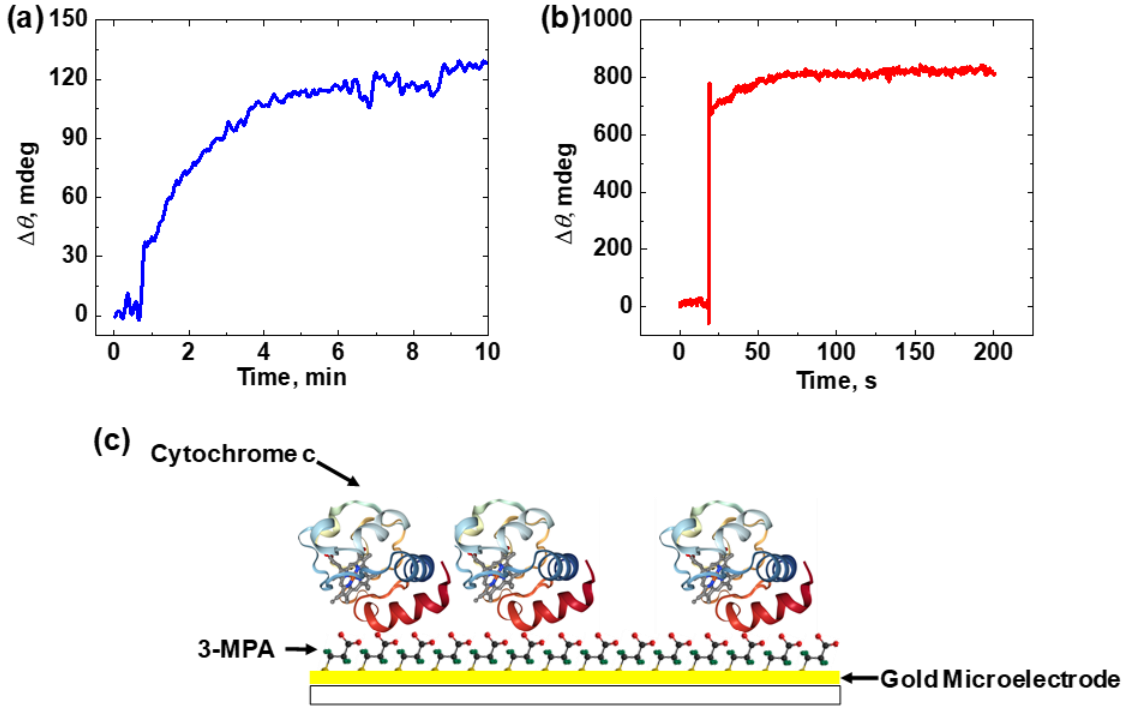

Figure 2.20: Plasmonic monitoring of 3-MPA modification (a) and cytochrome c adsorption (b) on gold microelectrodes, where $\Delta\theta$ is the surface plasmon resonance angle shift determined from the plasmonic image intensity. 3-MPA concentration: 5 mM in deionized water, and cytochrome c concentration: 50 µM in 70 mM PBS. (c) Schematic of cytochrome c immobilized on 3-MPA coated gold surface, showing electrostatic attraction between the lysine groups of the protein and carboxylate groups of 3-MPA. Cytochrome c image from the RCSB PDB (www.rcsb.org) of PDB ID 2B4Z (Mirkin, N.; Jaconcic, J.; Stojanoff, V.; Moreno, A. Proteins: Structure, Function, and Bioinformatics, 2008, 70, 83).

2.6 Cyclic Voltammetry

Before the plasmonic-based chronoamperometry measurement, we first perform the cyclic voltammetry (CV) to figure out at which potential the reactions happen and how the response is. The CV of cytochrome c adsorbed on a 3-MPA modified microelectrode reveals a pair of oxidation and reduction peaks superimposed on a large background current arising from double layer charging and defects in the 3-MPA layer (red curve, Fig.2.21(a)).[87,99] The origin of the large background current was further confirmed by

performing CV on 3-MPA modified microelectrode without cytochrome c (blue curve, Fig.2.21(a)). From the peak areas, the coverage of cytochrome c was found to be 2.23 pmol/cm^2.

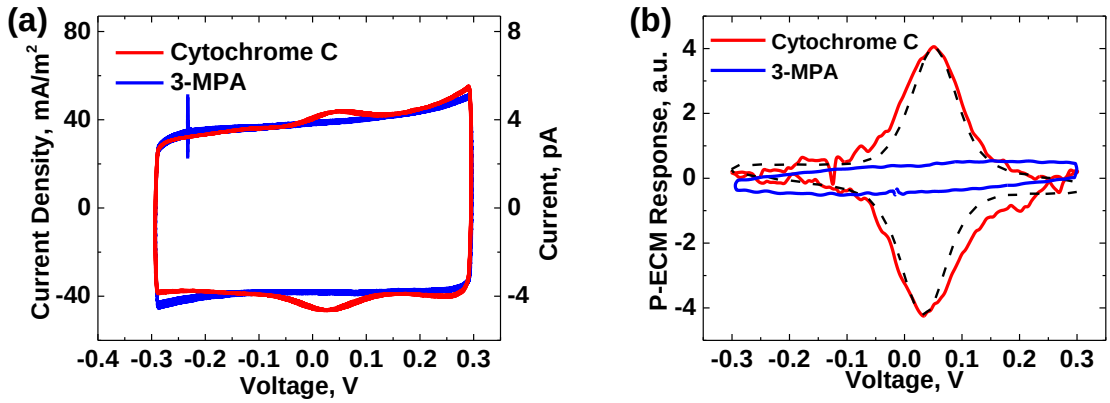

Figure 2.21: (a) Traditional (electrical measurement) CVs with (red) and without (blue) cytochrome c immobilized on a 3-MPA modified gold microelectrode. (b) Corresponding P-ECM CVs, determined from the time derivative of recorded plasmonic intensity, where the dashed line is an ideal CV. Buffer: 70 mM PBS; potential sweep rate: 1.2 V/s.

The corresponding CV obtained from P-ECM with Eqs. 2.6 and 2.7 shows a pair of well-defined oxidation and reduction peaks similar to those of the traditional CV (red curve, Fig.2.21(b)). However, the contribution of the background charging current to the CV of P-ECM (blue curve, Fig.2.21(b)) is small compared to the oxidation and reduction currents because $1/\alpha$ in Eq.2.10 is much smaller than $B\frac{\alpha_{ox}-\alpha_{red}}{nF}$ in Eq.2.9. This suppression of the charging current in P-ECM helps resolve fast ET current, which is a distinct advantage of P-ECM over the traditional chronoamperometry. We plotted the ideal CV for a fully reversible one-electron transfer reaction for a layer of homogeneous redox species immobilized on an electrode. The measured CV is in good (87%) agreement with that of the ideal CV in terms of peak separation, width and shape.

To prove most of our oxidation/reduction signal is coming from cytochrome c sample instead of impurity, we also conduct the UV-VIS absorption spectrum (Fig.2.22(a)) and HPLC (Fig.2.22(b)) measurement. The materials and parameters of our HPLC analysis (1260 Infinity Automated LC/MS Purification System, Agilent Technologies) are shown in the table below, similar as that provided by Sigma-Aldrich.[100] We prepared the sample in which cytochrome c was dissolved in the solution [A] (Table 2.2) at 0.8 mg/mL, and measured the UV-VIS absorption spectrum by the spectrophotometer (Nanodrop 2000c, Thermo Scientific™). The two absorption peaks of cytochrome c sample are similar to those reported in literature.[95,101] The HPLC show a well-defined peak, which is also consistent with the specs of the sample (95%).

Table 2.2
Test Parameters of HPLC analysis

column	Discovery BIO Wide Pore C18, 15 cm × 4.6 mm I.D., 5 µm particles (568222-U)
mobile phase	[A] (0.1% TFA in water) : (0.1% TFA in acetonitrile); (70:30) [B] (0.1% TFA in water) : (0.1% TFA in acetonitrile); (64:36)
gradient	0-100% B in 30 min
flow rate	1 mL/min
temp	ambient
detector	UV, 210 nm
injection	15 µL cytochrome c at 0.8 mg/mL in 0.1%TFA

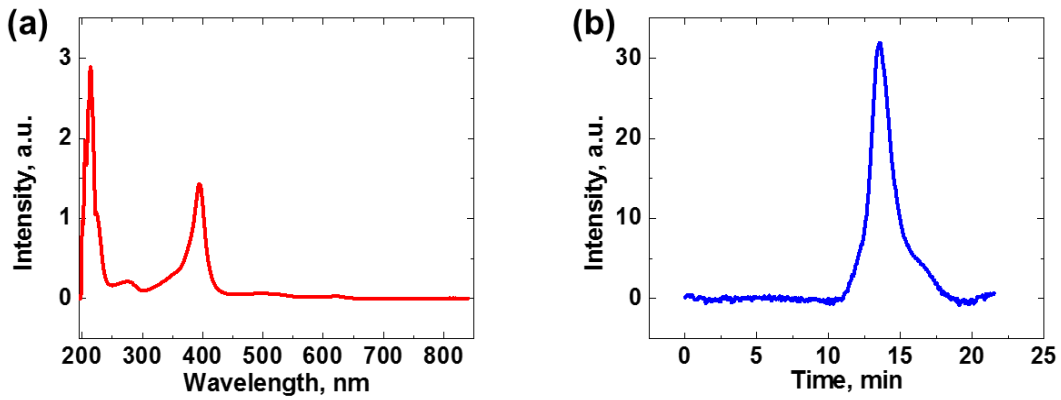

Figure 2.22: Absorption spectrum (a) and HPLC measurement (b) of cytochrome c sample.

2.7 ET Detection of Cytochrome c by Fast P-ECM

The CV measurements show that most of the electrochemical response in the P-ECM signal comes from the ET reaction of cytochrome c. To study the kinetics of the ET reaction, we performed chronoamperometry with both the traditional electrical and P-ECM methods. We started the experiment by holding the potential at -0.3 V, at which cytochrome c was at the reduced state, and then stepped the potential to +0.3 V to oxidize the redox protein, during which we recorded both the transient plasmonic and electrical responses. During oxidation, the plasmonic imaging intensity increases over time, which provides oxidation kinetics (Fig.2.23(a)). The transient plasmonic intensity is proportional to the charge transfer (Eq.2.6), so it probes ET kinetics like the traditional chronocoulometry. We attempted but failed to fit the transient plasmonic signal with exponential functions (Fig.2.24), but could fit the kinetics with a stretched exponential function, $e^{-(k_{ox}t)^{\beta}}$, with $k_{ox} = 7.80 \times 10^3\ s^{-1}$ and $\beta = 0.5$, respectively.

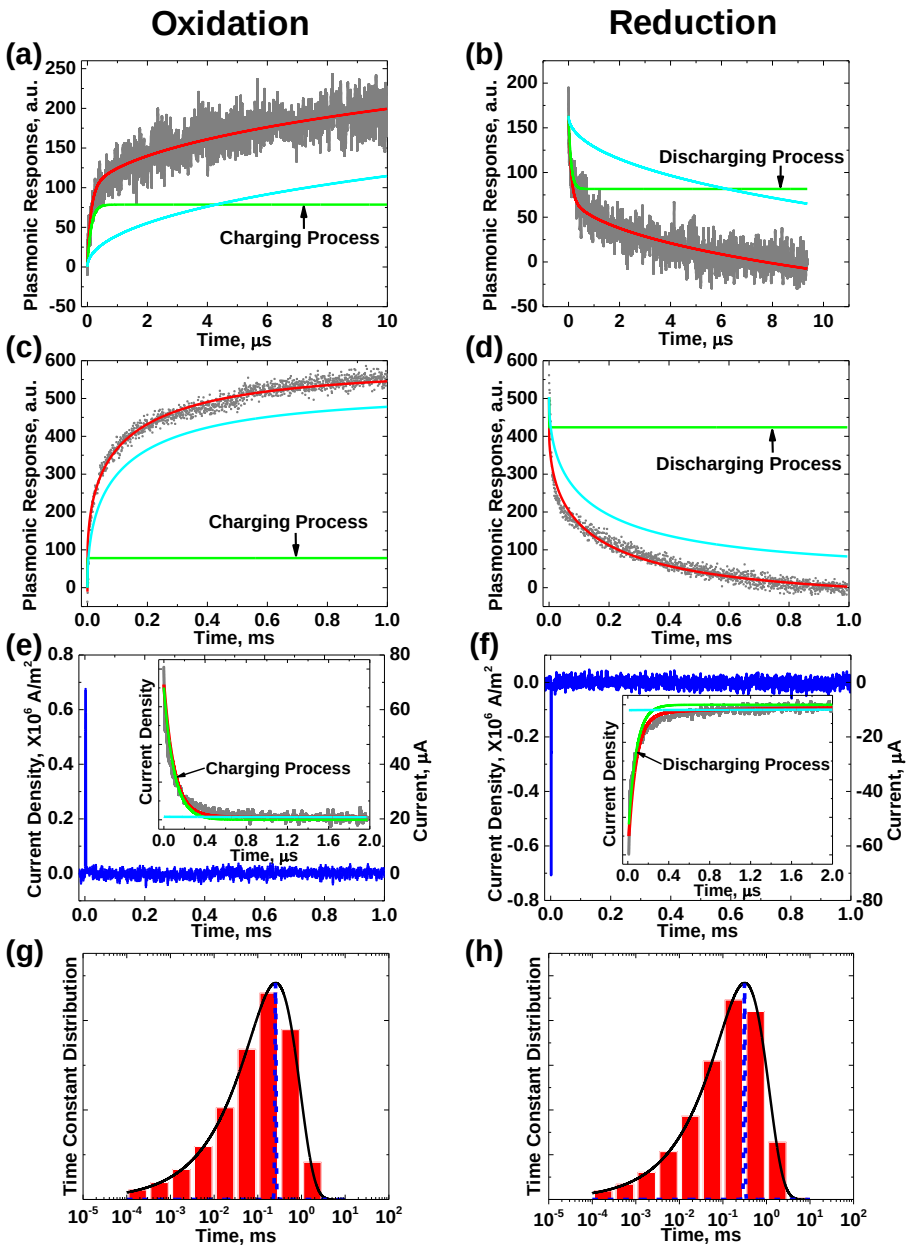

Figure 2.23: P-ECM data (grey) and fitting (red) to stretched exponential functions during oxidation (a) and reduction (b) over 10 μs, where green and cyan curves are the charging and conformational change processes, respectively. (c) and (d) are similar to (a) and (b), except the time window was expanded to 1 ms, showing good fitting of the experimental data over a wide time widow. (e) and (f) are simultaneously recorded chronoamperometry data showing charging as the dominant contributions. Insets: Zooming-in to the initial current responses. The electrode potential was stepped to +0.3 V from -0.3 V during oxidation, to -0.3 V from +0.3 V during reduction. (g) and (h) are the distribution of time scales of conformational changes associated with oxidation (g) and reduction (h), where the dashed lines indicate single-time constant distribution with a width reflecting measurement error.

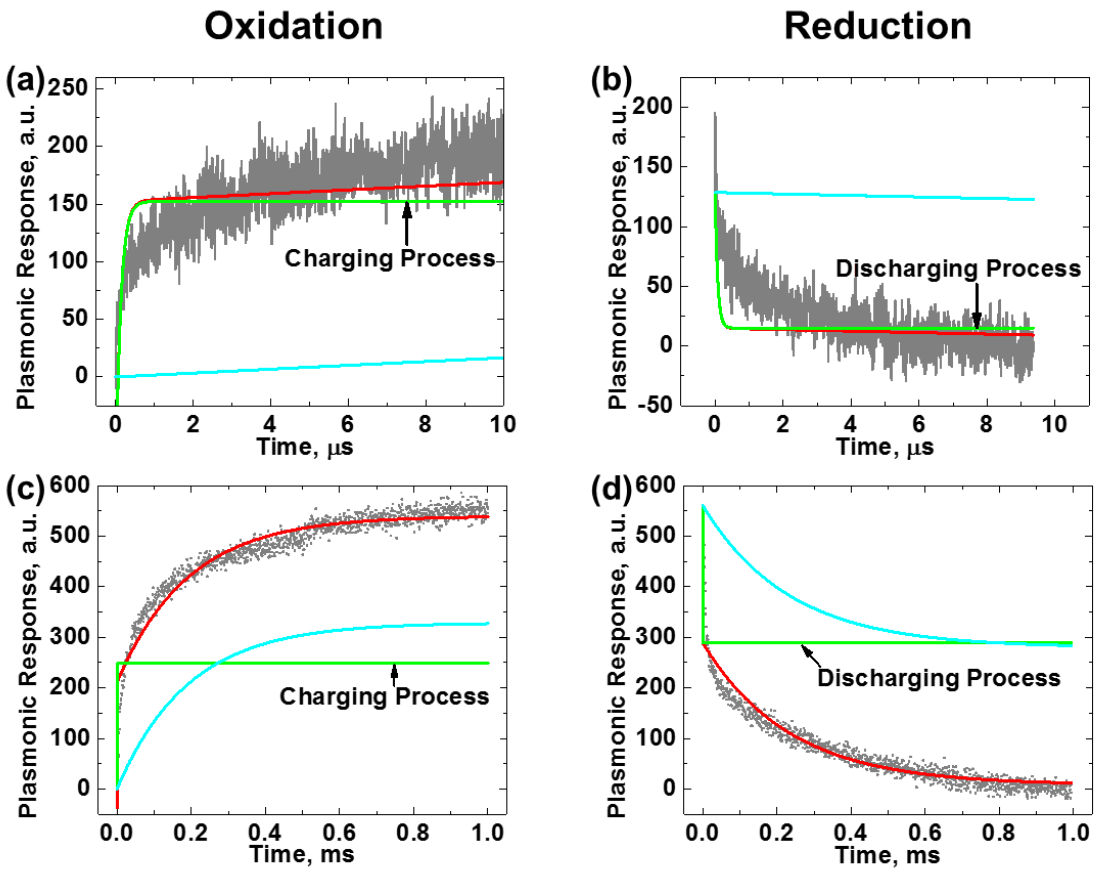

Figure 2.24: Fitting (red) of cytochrome c ET kinetics measured by P-ECM (grey) over different time windows using simple exponential functions, $(A_1(1-e^{-k_{c1}t})+A_2(1-e^{-k_{ox}t})+C_1$ for oxidation and $B_1e^{-k_{c2}t}+B_2e^{-k_{red}t}+C_2$ for reduction, respectively), where charging and conformational contributions are presented by green and cyan curves, respectively.

We note that although the capacitive charging contribution was relatively small, it was included in the fitting with the time constant determined from the chronoamperometry with 3-MPA modified microelectrode (without cytochrome c). The corresponding fitting equation is $A_1(1-e^{-k_{c1}t})+A_2\left(1-e^{-(k_{ox}t)^{\beta}}\right)$, where A_1 and A_2 describe the relative contributions from the charging and ET processes, which were determined to 14.1% and 85.9%, respectively, by fitting the data with the above expression (Table 2.3). The

relatively small A_1 is consistent with the observation that the charging contribution is small compared to the ET process in P-ECM.

Table 2.3
Charging and ET rates of cytochrome c (Fig.2.23)

	Time Scale	*Component*	*Oxidation Process*		*Reduction Process*	
			Contribution, %	*Rate Constant, s^{-1}*	*Contribution, %*	*Rate Constant, s^{-1}*
P-ECM	**10 µs**	**Charging**	$A_1 = 14.12$	$k_{c1} = (7.80 \pm 0.20) \times 10^6$	$B_1 = 15.08$	$k_{c2} = (1.30 \pm 0.10) \times 10^7$
		Conformation	$A_2 = 85.88$	$k_{ox} = (7.80 \pm 0.05) \times 10^3$	$B_2 = 84.92$	$k_{red} = (6.29 \pm 0.03) \times 10^3$
	1 ms	**Charging**	$A_1 = 13.26$	$k_{c1} = (8.10 \pm 0.30) \times 10^6$	$B_1 = 14.87$	$k_{c2} = (1.10 \pm 0.30) \times 10^7$
		Conformation	$A_2 = 86.74$	$k_{ox} = (8.00 \pm 0.10) \times 10^3$	$B_2 = 85.13$	$k_{red} = (6.52 \pm 0.07) \times 10^3$
Electrical Method	**10 µs**	**Charging**	$A_1 = 97.97$	$k_{c1} = (1.00 \pm 0.06) \times 10^7$	$B_1 = 97.69$	$k_{c2} = (1.27 \pm 0.04) \times 10^7$
		Conformation	$A_2 = 2.03$	$k_{ox} = (7.70 \pm 1.20) \times 10^3$	$B_2 = 2.31$	$k_{red} = (6.00 \pm 1.00) \times 10^3$

* $k_{c1,2}$ are charging/discharging rate constants, respectively. k_{ox} and k_{red} are rate constants for the oxidation and reduction of the redox protein, respectively. Note: The relative contributions from capacitive charging (A_1 and B_1,) are small in P-ECM compared to ET (A_2 and B_2). In contrast, the relative contributions from capacitive charging dominate the measured current in the traditional electrical measurement.

The analysis above shows that the ET kinetics measured with P-ECM follows a stretched exponential function over a time scale from 0.1 to 10 µs. To further validate the observation, we extended the time window to 1 ms, and found that the same stretched exponential function fits the data over a broad time window (0.1 µs to 1 ms) (Fig.2.23(c)). The simultaneously recorded electrical current (chronoamperometry) shows a rapid decay of the current, which is primarily due to the charging process (Fig.2.23(e)). Zooming in of the transient current in Fig.2.23(e) shows exponential decay of the charging current with a time constant of $1.0 \times 10^7\ s^{-1}$, similar to that obtained for the 3-MPA modified microelectrode (Inset, Fig.2.23(e)). The ET component of the measured current is

overwhelmed by the large capacitive charging current as expected from the CV shown in Fig.2.21(a), so kinetic analysis of the ET rate is difficult with the traditional chronoamperometry.

We carried out the electrical and plasmonic measurements for the reduction process by stepping the potential from +0.3 V to -0.3 V (Figs.2.23(b), (d) and (f)). The P-ECM image intensity also follows the stretched exponential function, $e^{-(k_{red}t)^{\beta}}$, with $k_{red} = 6.29 \times 10^3\ s^{-1}$ and $\beta = 0.5$, similar to that of the oxidation process. The fitting equation is $B_1 e^{-k_{c2}t} + B_2 e^{-(k_{red}t)^{\beta}}$, where B_1 and B_2 describe the relative contributions from the discharging and ET processes. The relative contributions of the double layer charging and ET processes are close to those found for the oxidation process (Table 2.3), and the corresponding electrical measurement (chronoamperometry) shows a discharging current constant similar to that of the oxidation process (Table 2.3), further validating the findings for the oxidation process.

To validate the observation, we performed the measurement with different starting and ending potentials. Fig.2.25(a) and (b) show the plasmonic responses during oxidation and reduction of cytochrome c when stepping the potential from -0.4 V to +0.4 V. Fig.2.25(c) and (d) show the measurements while varying the potential from –0.2 V to +0.2 V. The results can also be fitted well with stretched exponential functions (Table 2.4). We also carried out the measurement by stepping the potential from -0.3 V and -0.1 V, and detected smaller responses with a relatively large capacitive charging background (Figs. 2.25(e) and (f)). Stepping the potential between wider ranges may cause electrode instability. The results show similar rate constant as the potential range of $\pm$0.3 V.

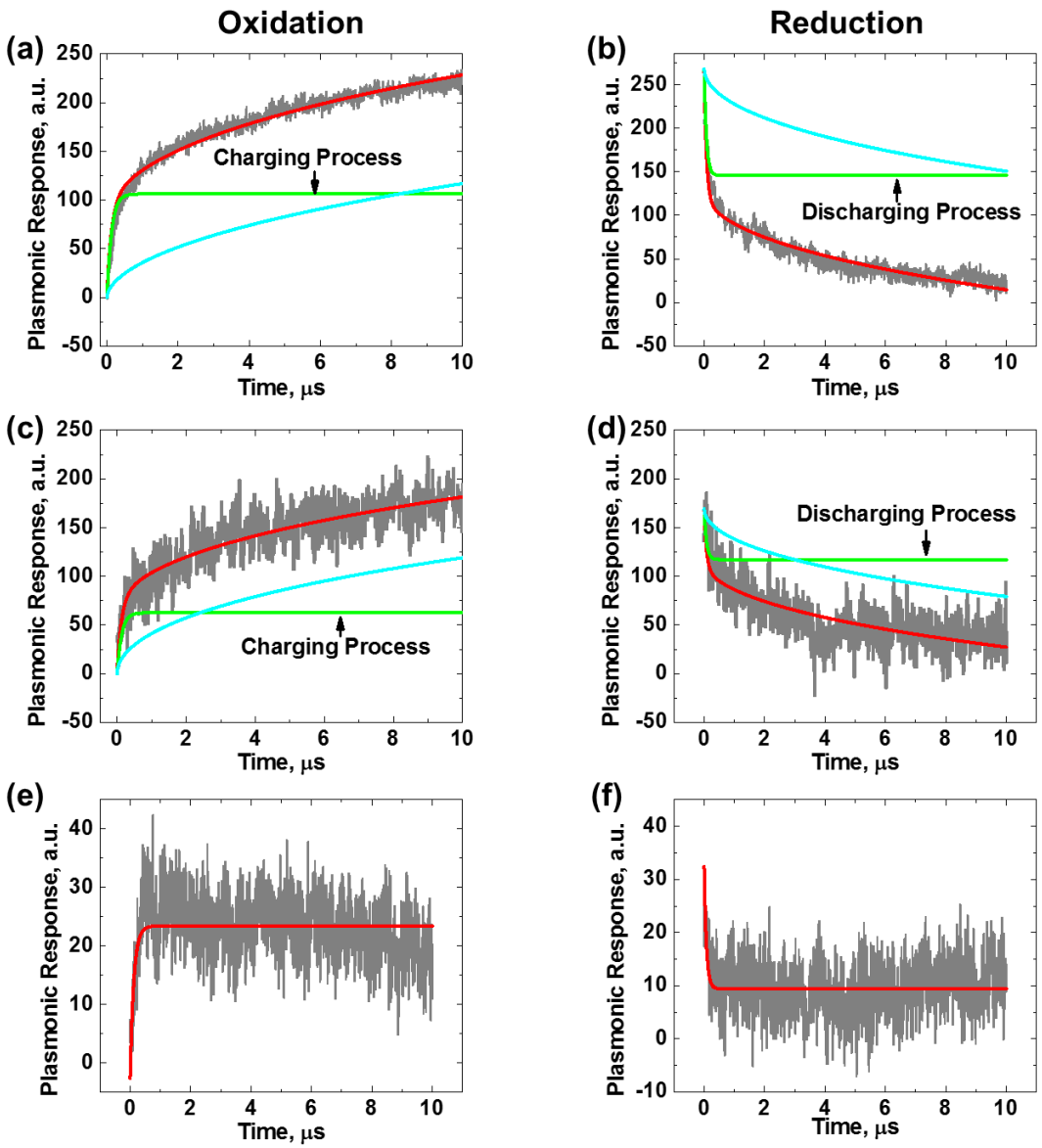

Figure 2.25: P-ECM data (grey) and fitting (red) to stretched exponential functions, where green and cyan curves are the charging and conformational change processes, respectively. In (a) and (b), the electrode potential was varied between -0.4 V and +0.4 V at 50 kHz, in (c) and (d) the electrode potential was varied between -0.2 V and +0.2 V at 50 kHz, and in (e) and (f) the electrode potential was varied between -0.3 V and -0.1 V at 50 kHz.

Table 2.4
Charging and ET rates of cytochrome c with different starting and ending potentials (Figs.2.25)

Potential Range	*Component*	*Oxidation Process*		*Reduction Process*	
		Contribution, %	*Rate Constant, s^{-1}*	*Contribution, %*	*Rate Constant, s^{-1}*
-0.4 V ~ +0.4 V	***Charging***	$A_1 = 17.24$	$k_{c1} = 7.80 \times 10^6$	$B_1 = 18.56$	$k_{c2} = 1.30 \times 10^7$
	Conformation	$A_2 = 82.76$	$k_{ox} = 7.82 \times 10^3$	$B_2 = 81.44$	$k_{red} = 6.33 \times 10^3$
-0.3 V ~ +0.3 V	***Charging***	$A_1 = 14.12$	$k_{c1} = 7.80 \times 10^6$	$B_1 = 15.08$	$k_{c2} = 1.30 \times 10^7$
	Conformation	$A_2 = 85.88$	$k_{ox} = 7.80 \times 10^3$	$B_2 = 84.92$	$k_{red} = 6.29 \times 10^3$
-0.2 V ~ +0.2 V	***Charging***	$A_1 = 10.26$	$k_{c1} = 7.80 \times 10^6$	$B_1 = 11.36$	$k_{c2} = 1.30 \times 10^7$
	Conformation	$A_2 = 89.74$	$k_{ox} = 7.83 \times 10^3$	$B_2 = 88.64$	$k_{red} = 6.30 \times 10^3$
-0.3 V ~ -0.1 V	***Charging***	$A_1 = 100$	$k_{c1} = 8.28 \times 10^6$	$B_1 = 100$	$k_{c2} = 1.33 \times 10^7$

Kinetic that follows an empirical stretched exponential function has been observed in other complex systems,[102,103] which indicates multiple time scales involved in the kinetics. The corresponding distribution of the time scale for a stretched exponential function is given by[104]

$$G(\tau) = \frac{1}{2\sqrt{\pi}}\sqrt{\frac{\tau}{\tau_0}}e^{-\frac{\tau}{4\tau_0}}, \qquad (2.11)$$

where τ_0(red) and τ_0(ox) are inversely proportional to the reduction and oxidation rate constants k_{red} and k_{ox}, of the molecules obtained from the fitting described above. The average time constant is $< \tau >= \frac{\sqrt{\pi}}{2\beta}\tau_0$, and the corresponding average ET rate constant is $< k >= \frac{2\beta}{\sqrt{\pi}}{\tau_0}^{-1}$. The distributions of time scales involved in the oxidation and reduction of cytochrome c are shown in Figs.2.23(g) and (h), which vary over a range from sub-μs to ms. The average time constants are 0.23 ms and 0.28 ms for the oxidation and reduction processes, respectively, which are consistent with that extracted from CV.[84,85]

Previous studies have shown that conformational fluctuations in cytochrome c provide gating to the ET of the molecule.[70,71,82,84,85] The conformation gating model assumes that ET between the heme group and the electrode is fast, and the rate limiting step is the conformational changes in the redox protein.[84,85] Recent Raman and molecular dynamics simulation studies further indicated that the conformational gating involves reorientation of the heme group, occurring at a time scale of about 0.35 ms.[82–85] This time scales matches well with the average time constant observed here, but the present work shows a broad distribution of time scale around the average value. Our high-performance liquid chromatography data (Fig.2.22) shows a pronounced peak with a small shoulder (possibly due to modified cytochrome c[105–107]), and measured CV agrees (87%) with the ideal CV, indicating that heterogeneity in the protein sample and adsorption geometry could contribute to but is unlikely to be the dominant source of the extremely broad time scale. Our data suggest that the re-orientation of the heme group couples with nuclear motions at different time scales.

2.8 Conclusion

We have demonstrated a P-ECM approach to study fast electrochemistry with fast optical detection (a few ns, and limited by the response of the electrochemical cell). Using the approach, we have studied ET of a redox protein (Cytochrome c) adsorbed on a 3-MPA modified microelectrode. P-ECM measures both the capacitive charging and ET currents, but the former is greatly suppressed compared to the traditional electrochemical measurements. This suppression of charging current, together with the fast detection time of P-ECM, allows us to directly study the kinetics of ET in cytochrome c with

chronoamperometry over a broad time window (100 ns – 1 ms). Although the average time constants obtained with P-ECM agree with those obtained with traditional electrochemical methods, P-ECM reveals that the ET process occurs at multiple time scales, ranging from sub-μs to ms, indicating that conformational gating of the ET in the protein involves different conformational changes. We anticipate that the plasmonic methods can contribute to the study of fast electrochemical processes on electrodes, especially when combining it with the indirect laser induced temperature jump approach.

CHAPTER 3

MONITORING MOLECULAR INTERACTIONS IN NANOLITER DROPLETS ARRAY WITH AN INTEGRATED MICROARRAY PRINTING AND PLASMONIC DETECTION SYSTEM

3.1 Introduction

Monitoring molecular interactions is critical to the understanding of many biological processes, and directly relevant to applications in drug screening, disease biomarker discovery and fundamental protein functional studies.[108–111] A key to molecules interactions is the kinetic information, which tells how and how long the process going.[24,112,113] However, molecules in living organism are of great variety, e.g. there are ~3000 proteins in E-coli and estimated 2 million proteins in human body, and one kind of molecule can function by interacting with many other kinds of molecules, indicating the urgent need for high-throughput detection.[114–116]

The common practice of realizing molecular interactions involves techniques using fluorescence or radioactive molecules, or nanoparticles to label the target molecules.[117–122] While these labeling approaches are helpful for investigating certain processes, the tags can sometime be problematic, because they may affect the activity of the original molecules and lead to an inaccurate measurement.[119,123,124] Certain label free techniques, such as isothermal titration calorimetry and microscale thermophoresis, measure the state before and after molecular interactions.[125–129] These end-point assays based methods could measure the binding affinity but provide no kinetic information, which limit their applications especially in drug screening. Although backscattering interferometry can

measure the dynamic binding process, it is not suitable for high-throughput detection purpose.[130,131]

As a member of label free techniques, surface plasmon resonance imaging (SPRi) surpasses end-point static observations with real-time direct quantification of interaction kinetics, and extends the capability to array detection.[45,132–134] Though series of SPRi related technologies have been developed to measure the molecular interactions, these methods require continuous flow of analyte solutions, leading to a large consumption of molecular samples.[4,42,135–137] This will bring a great increase in cost, especially when the sample is rare and expensive, such as purified proteins and cerebrospinal fluids from patients. While some microarray techniques were introduced to solve this problem, such as patterned gel by photolithography and microfluidic wells, the design was sometime complicated and not user friendly (hard to change according to users' need).[136–140]

Here, we developed an integrated microarray printing and detection system (IMPDS) for high-throughput and versatile measurement of molecular interactions with ultra-low volume cost of analyte samples. The principle is to dispense the ligand and analyte by ultra-low volume piezoelectric liquid printing, and simultaneously record the binding process using SPRi. Unlike conventional techniques, this method allows spot-on-spot nanodroplet-based interactions that consume much less sample volume and enables flexible M × N combinations of spot interactions, with the capability of measuring binding kinetic in long time (longer than 10 mins). Using this technique, we have demonstrated the capability of detecting different ligand-analyte interactions in 10×10 nanoliter droplet array. Furthermore, we have successfully built a model to quantify and extracted the rate constants of binding process in tiny droplets, while considering the depletion and diffusion

of analytes. This work is accomplished with the help of Feng Xiao, who cooperated to finish part of the experiments. The data processing method is actually original in this thesis, and part of the results shown here are adapted from the thesis of Feng Xiao due to equally contribution.

3.2 Experiment Setup and Working Principle

The breadboard system and principle of IMPDS to measure binding kinetics is illustrated in Fig.3.1.

A novel ultra-low volume piezoelectric liquid dispensing (PLD) system is held over the top of a proprietary high-resolution distortion-free surface plasmon resonance imaging (DF-SPRi) system. To study molecular binding of the array, the PLD system is programmed to introduce the drop-on-drop interaction on each spot, while the SPRi system records the plasmonic image on modified gold surface in real-time. With the capability of printing as small as 0.4~0.6 nL on each spot and as much as 8 spots simultaneously, the IMPDS is able to bring in and measure the interactions in a less consumption and high-throughput way. SPRi enables real-time quantification of interaction kinetics and could provide real-time feedback for modification process from the very first step. With a detection limit of 0.78 response unit (RU) for 1 second temporal resolution, our SPRi could quantify the kinetic accurately (Fig.3.2).

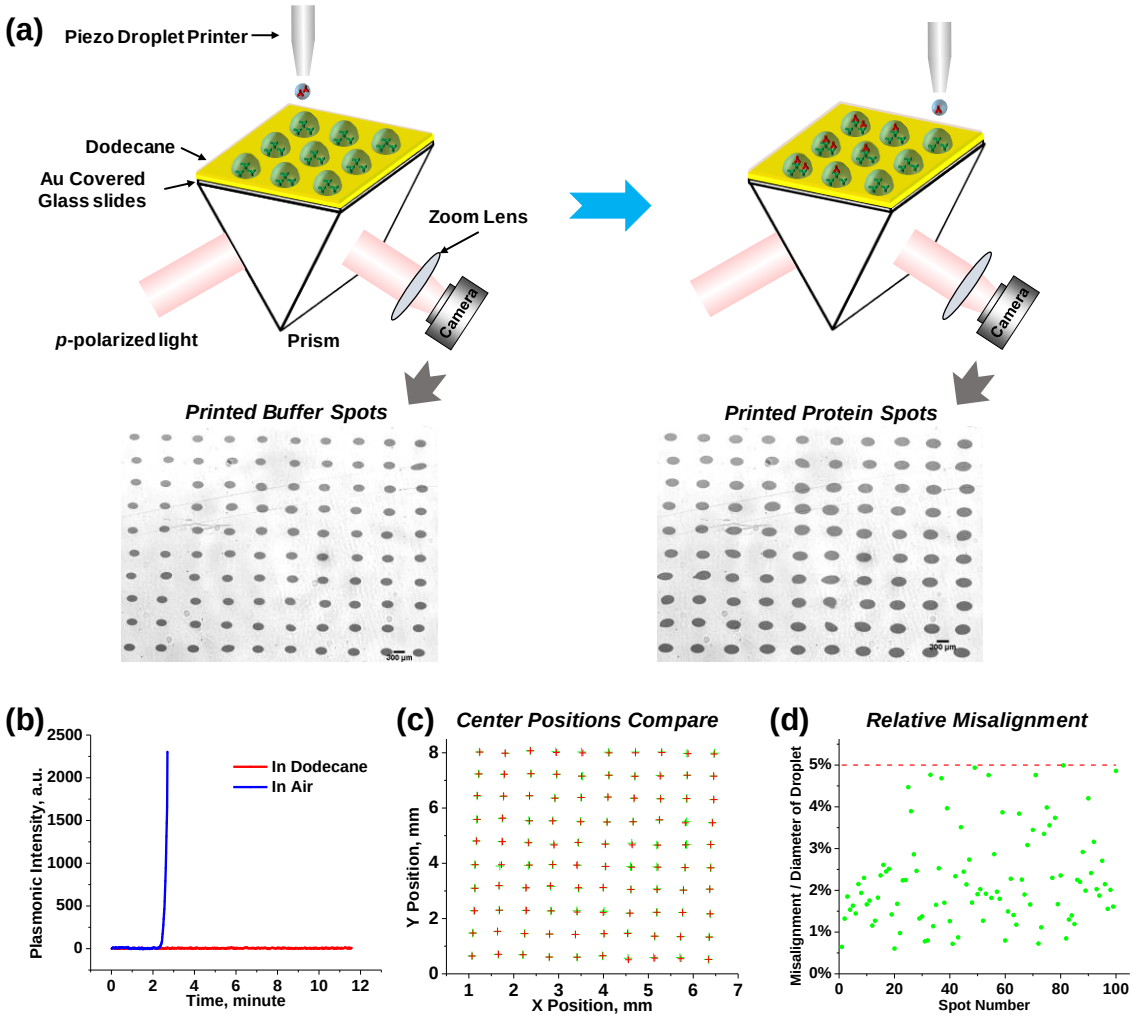

Figure 3.1: (a) Schematic drawing of Integrated Microarray Printing and Detection System (IMPDS) and the way it works. Insets: plasmonic images of printed buffer and protein array in dodecane, respectively. The center to center distance between spot is 0.8 mm. (b) Plasmonic image intensity time profile of the printed spots in air and in dodecane, which shows good stability after covered by the mineral oil. (c) shows the 10 × 10 center positions of buffer spots (green) and protein spots (red) in (a). (d) is the relative misalignment between the two spots in the two-time printing, compared with corresponded droplet radius (adapted from. ref 141).

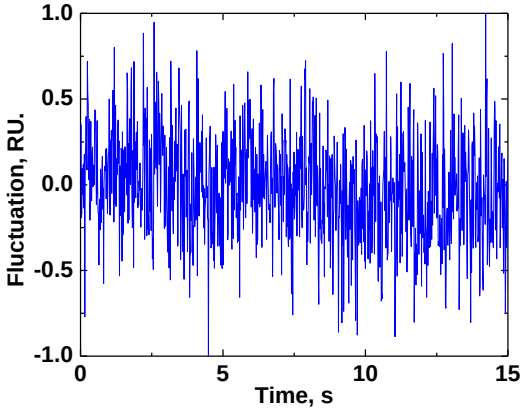

Figure 3.2: IMPDS setup noise during 15 s.

To monitoring the molecular interaction in the droplet, one of the challenges is the evaporation. Since the plasmonic intensity is very sensitive to the salt concentration and temperature, the evaporation of such a tiny droplet in a short time will lead to a huge deformation (time-related) of the signal and severely affect the binding process in an unquantifiable way. Furthermore, smaller droplet dries out even faster, e.g. a 3 nL droplet will dry out in seconds, bringing the difficulty of measuring the kinetic of long time binding. To prevent the evaporation, the chips are first covered by a thin layer of dodecane (~40 μL) before printing the array, as shown in Fig.3.1(a). Since dodecane has low viscosity (1.34 mPa·s), high boiling point (216.3 ℃) and is lighter than water (750 kg/m^3), it could perfectly help to prevent the evaporation of droplet from the very beginning. Fig.3.1(b) shows the time profile of a single spot plasmonic response covered by dodecane, and the intensity shows almost no fluctuation compared with the one in air during 10 mins, which is sufficiently for most binding measurement. We also tried other oil like silicone and perfluorononane, but dodecane works best. Perfluorononane is heavier than water (1799 kg/m^3), so it could not hold the droplet to contact the gold surface. While silicone oil is

lighter than water (913 kg/m^3) it has larger viscosity (5.5 mPa·s) and less stable (boiling point ~140 ℃). Moreover, the droplet spreads much more in silicone oil, leading to smaller binding signal (larger surface area) and hard control of the droplet shape (may bring cross interactions between nearby spots).

While the dodecane can stop the evaporation, it may also lower the dispensing accuracy among different time printing. To ensure that we have a good alignment, every time we dispensed 5 droplets on each spot with each droplet volume of 0.6 nL. Because the location of each droplet shot from the PLD followed a gaussian distribution around the center position, more droplets would surely help to decrease the misalignment. However, this will increase the droplet size and narrow the gap between nearby droplet, resulting in more consumptions of sample and lowers array density. Fig.3.1(c) compares the centers of spots between two times printing (buffer first and then anti-BSA), which shows very small misalignment for all the 10×10 spots. This is also confirmed by the histogram plot of the misalignment (Fig.3.1(d)), demonstrating a less than 5% displacement to radius ratio, which indicates the good performance of droplet printing. Fig.3.3 shows the case in which the printing parameter are not well adjusted.

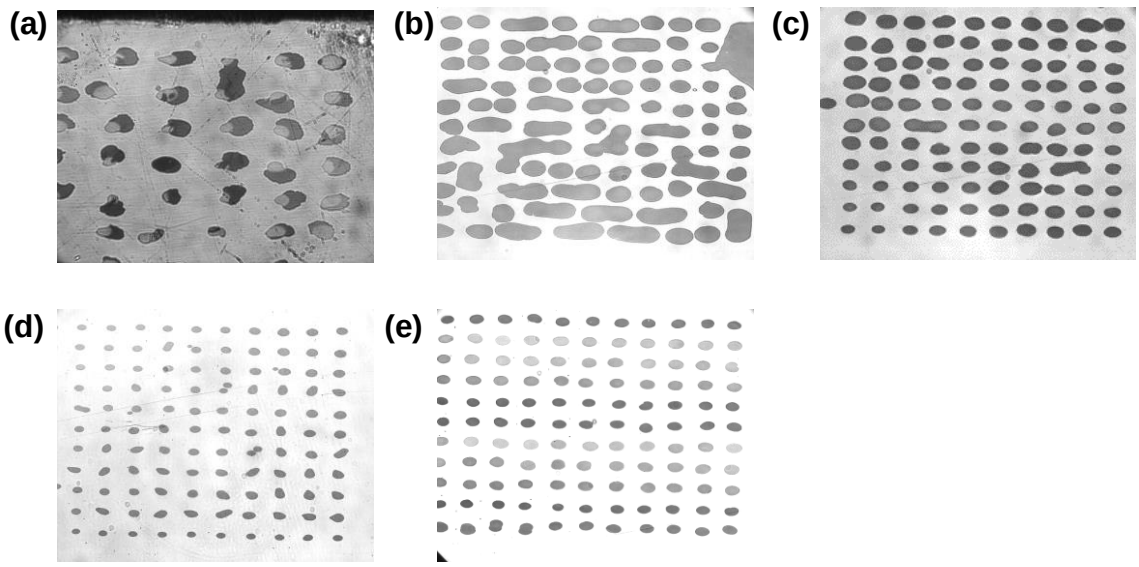

Figure 3.3. Printing results when parameters are not well adjusted. (a) Octane as the cover oil. Surface get dirty and droplet spread. (b) Silicon oil as the cove oil. Droplets cover relatively large surface area and begin to merge with each other. (c) Too strong power of the piezo printer. (d) Too small power of the piezo printer or the oil layer is too thick. (e) The oil layer is too thin.

3.3 Materials and Method

Chemicals. N-hydroxysuccinimide (NHS), N-ethyl-N'-(3-dimethylaminopropyl) carbodiimide hydrochloride (EDC), Sodium acetate (NaOAc), Acetic acid (AcOH), Tween® 20, Ethanolamine, Dodecane, Bovine serum albumin (BSA) and anti-BSA antibody (produced in rabbit) were obtained from Sigma-Aldrich (St. Louis, MO). Dithiolalkanearomatic-PEG3-OH (Dithiol-PEG-OH) and dithiolalkanearomatic-PEG6-COOH (Dithiol-PEG-COOH) were purchased from SensoPath Technologies (Bozeman, MT). 1 nM mixed dithiol ethanol solution of 10:1 PEG-OH/PEG-COOH were prepared for modification of pre-cleaned gold chip. Aqueous solution containing 100 mM NHS and 400 mM EDC for further surface activation, blocking buffer solution of 1 M Ethanolamine, binding buffer solution of 10 mM pH=5.0 NaOAc/AcOH were prepared from deionized

water (Milli-Q, Millipore Corp.). Both the NaOAc/AcOH buffer solution and phosphate buffered saline (PBS, Corning cellgro, 154 mM NaCl, 5.6 mM Na_2HPO_4, and 1.1 mM KH_2PO_4) were added 0.1% Tween 20 before usage. 200 μg/mL BSA solution and 100 nM anti-BSA solution was were prepared by dissolving BSA in NaOAc/AcOH buffer solution and anti-BSA antibody in PBS buffer solution, respectively. Different concentrations of anti-BSA solution were obtained by diluting the 100 nM anti-BSA solution using the PBS buffer.

Instrumentation. Fig.3.1(a) is a schematic illustration of the experiment setup. Collimated p-polarized light-emitting diode (LED) with 670 nm wavelength and 1 mW power shoot onto the gold-coated slides through a triangular prism for surface plasmon excitation. The plasmonic image was collected by a CCD camera (Pointgrey, Flea3 1.3 MP Mono USB3 Vision) through a 10× variable zoom lens with a spatial resolution of ~5 μm at a frame rate of 30 frames per second. A PDMS well was placed on top of the gold chip to serve for global washing purpose.

Chips preparation. Gold chips were prepared by gold deposition on cleaned BK-7 glass slides using thermal evaporation (Edwards II thermal evaporator). After cleaned with DI-water and ethanol, the gold chips were immediately dipped into 1 mM PEG-OH/PEG-COOH ethanol solution overnight in the dark. DI-water and ethanol were then used to remove excess molecules. 250 μL mixed 1:1 NHS/EDC solution was injected globally to activate the whole surface. This could convert the -COOH group into NHS ester receptor, which interact with amine group of BSA later. After activation, gradient washing (gradually diluted the NHS/EDC solution by DI water) was applied to clean the activated surface.

Experimental Process. The whole experimental process contains 4 major steps, as shown in the flow chart of Fig.3.4: 1) prepare and calibrate the sensor chip, 2) conjugate the receptor protein (BSA) to the sensor chip surface, 3) measure the binding interactions, and 4) process the data to obtain the associate and dissociate rate constants and binding affinity of each spots. Each major step consists of multiple steps that listed in Fig.3.4.

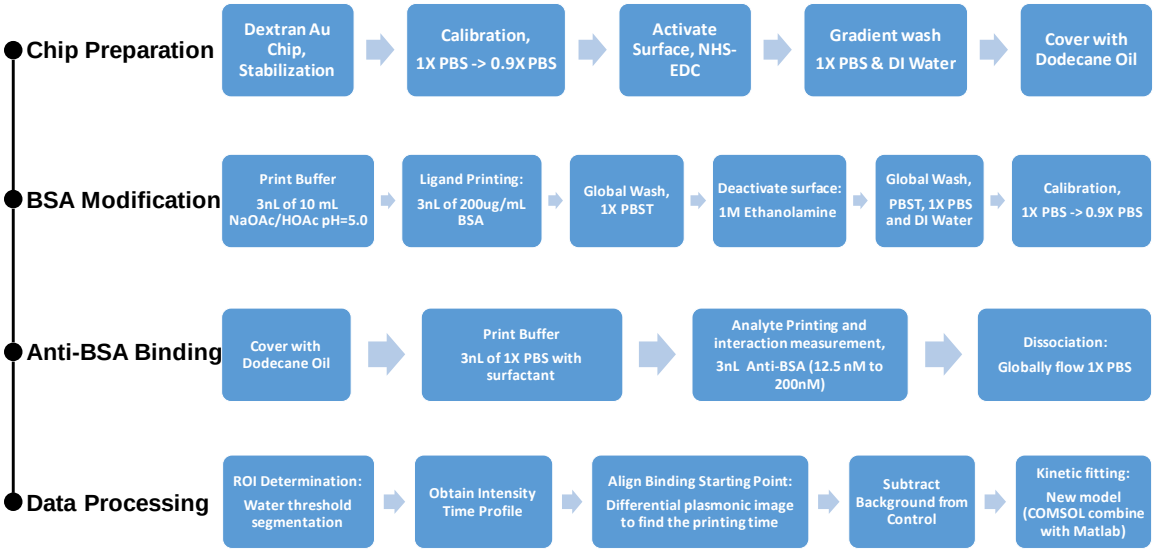

Figure 3.4: IMPDS experimental process

Data Analysis. To analyze the kinetic from individual spots of the array, a Matlab program (integrated with COMSOL) is fully developed for automatically processing images and extracted the binding kinetic information using the model described in Section 3.4. As shown in Fig.3.5, the integrated algorithms perform the following tasks: a) self-determine the ROI region (each spots) and binding starting point; b) obtain the intensity of individual spots; c) automatically fit each binding curves and extracted binding affinities. The COMSOL model we built is consist of two parts: the transport of diluted species module to take care of the molecule diffusion, and the surface reaction module which calculates the surface interaction. During the fitting process, Matlab provides value of fitting parameters (k_a, k_d and R_{eq}) to COMSOL, and the COMSOL will simulate the binding

curves and feed it back to COMSOL to compare with the experiment results. After calculating the difference, Matlab will send a new set of values to COMSOL and repeat the previous steps. Applied the fitting program, we could finally extract the rate constants.

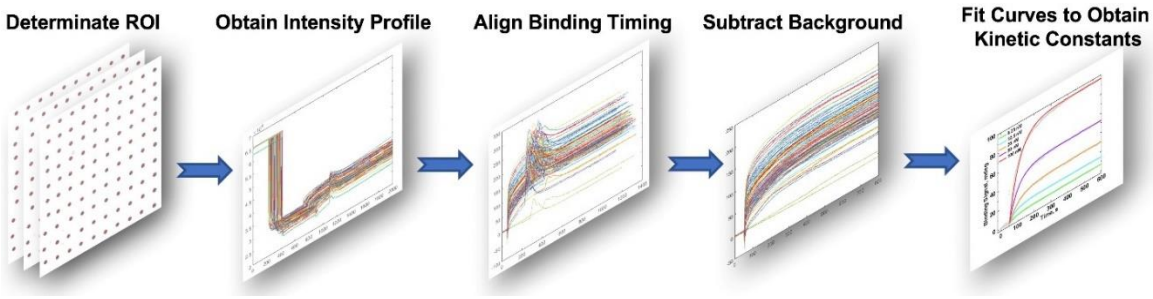

Figure 3.5: Flow chart of the data processing steps.

3.4 Protein Interactions Measurements

To demonstrate the capability of high-throughput and low sample consumption binding kinetic detection, we carried the experiment measuring bovine serum albumin (BSA) and anti-BSA interaction. To begin with, we calibrated the self-assemble monolayer (SAM) coated gold chip sensitivity, and the plasmonic intensity variation on the 100 spots are almost uniform (Fig.3.6(a)). The chip was then activated, followed by the modification of BSA which is done by first printing buffer on the surface and then dispensing the BSA with a concentration of 200 μg/mL on each of 10×10 spots. The good performance of our PLD system ensured the good alignment of our different times printing. Fig.3.6(b) and (c) show the time profile of plasmonic signal during BSA modification process and the final differential plasmonic image. The amplitude of BSA binding signal varied from spot to spot, which could be caused by multiple reasons, such as variation in droplet volumes, droplet to surface contact angles, binding efficiency and the activation process. However, this variation is not affecting the measurement of binding kinetics, as we will discuss later.

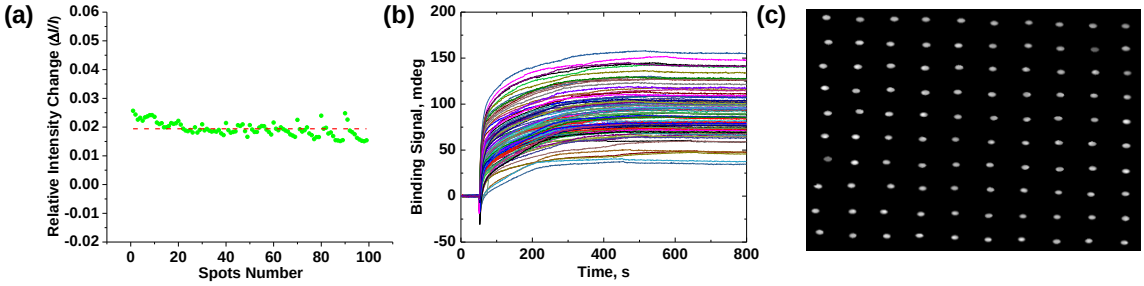

Figure 3.6: (a) Plasmonic calibration profile for 10 × 10 spots. (b) Detection of BSA binding signals. (c) Differential plasmonic image (subtract first frame) after BSA modification process.[141]

After the functionalization of the BSA receptors array, the analyte molecules (anti-BSA antibody) were introduced by first dispensing 3 nL buffer and then 3 nL droplets of analyte with 5 different concentrations (12.5 nM, 25 nM, 50 nM, 100 nM, 200 nM) onto the BSA spots with double row replicates for each concentration. Fig.3.7(a) shows the differential plasmonic image that reflect the maximum anti-BSA binding at all spots, obtained by subtract the plasmonic image recorded at 600 s (maximum anti-BSA binding) from the image recorded right before printing the anti-BSA droplets (50 s). Obviously, there is a trend of signal increase with higher concentration of the analyte. Fig.3.7(b)-(f) shows the association process of anti-BSA of all spots. Again, random variation of binding signal strength among the spots is observed; however, this does not affect the accuracy of binding kinetic measurement as we will show below.

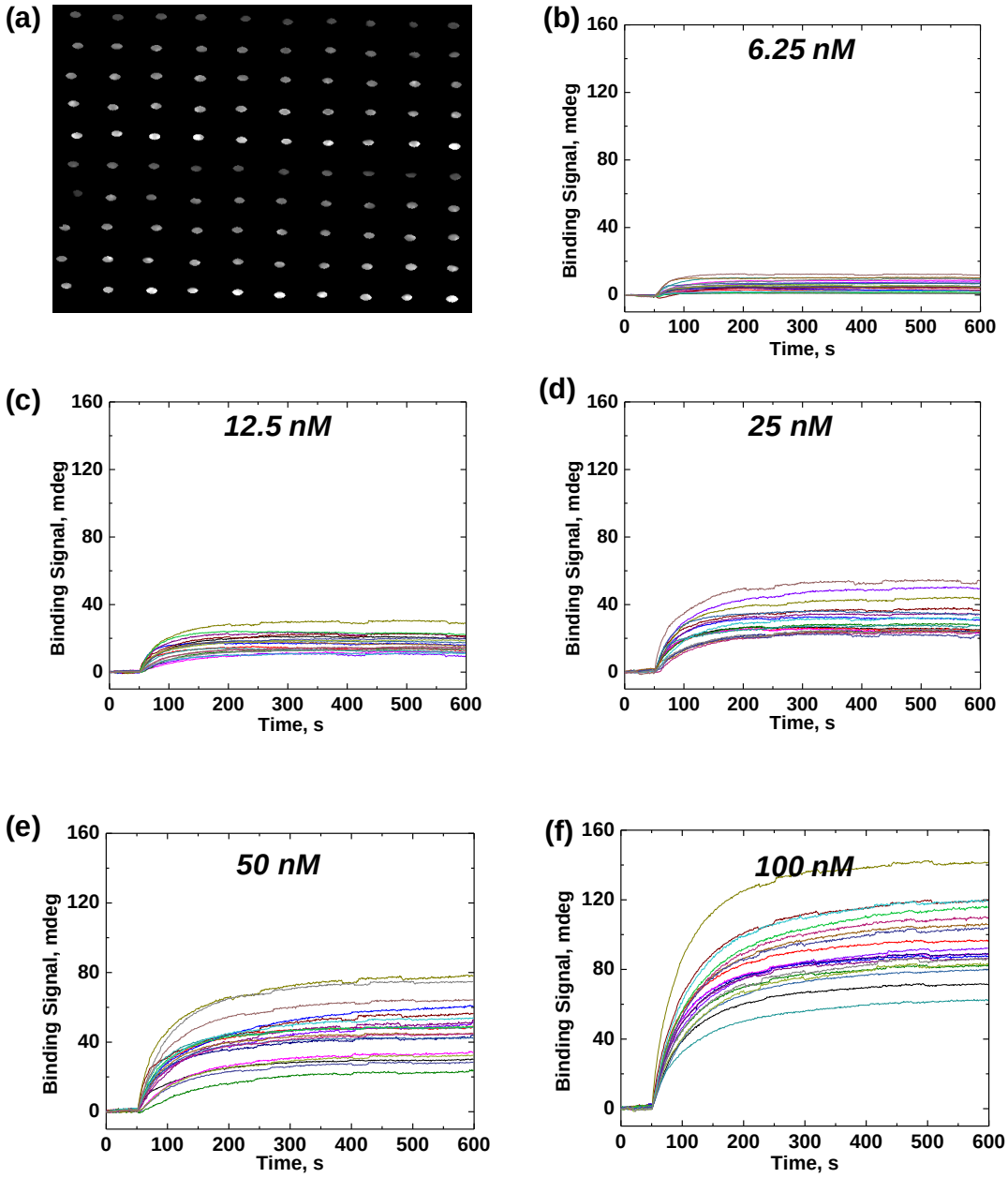

Figure 3.7：(a) Differential plasmonic image (subtract first frame) after anti-BSA with different concentrations binds to surface modified BSA. The concentrations of anti-BSA in (a): 1st and 6th row are 6.25 nM (b), 2nd and 7rd row are 12.5 nM (c), 3rd and 8th row are 25 nM (d), 4th and 9th row are 50 nM (e), 5th and 10th row are 100 nM (f). (b) – (f) are the time profile of plasmonic intensity for each spot, and each diagram corresponds to a certain concentration.

To precisely quantify the binding kinetics, dissociation process was also measured by continuously flowing phosphate buffer (1× PBS) globally, although dissociation rate

constant can be extracted from the multi-concentration association curves in principle. Fig. 3.8 shows the dissociation curves of all the 10 × 10 spots with 5 different concentrations of analyte.

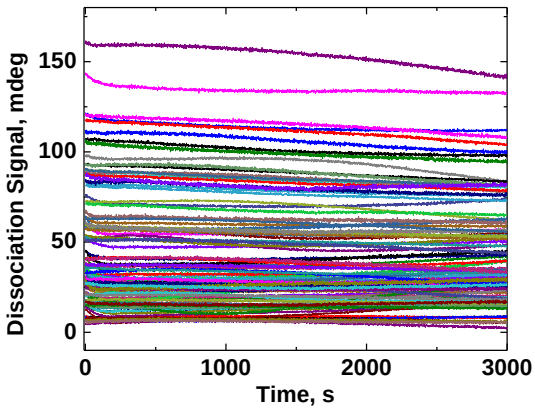

Figure 3.8: Dissociation curves of 100 spots.

3.5 Quantification of Binding Kinetics

Different from conventional instruments based on SPRi that require continuous sample flow through the surface, our IMPDS system enables real-time measurement of protein-protein interactions in tiny droplets. While the droplet-based measurement significantly reduces sample consumption and allows many binding pairs to be tested simultaneously on the same sensor chip, this also make kinetic constants extraction harder. In conventional SPRi measurements, the association process could be simply described by the following equation[142]

$$R_t = R_{eq}\left[1 - e^{-(k_a C + k_d)t}\right] \tag{3.1}$$

where R_{eq} is the plasmonic signal at steady state, C is the analyte concentration, k_a and k_d are the association rate constant and dissociation rate constant, respectively. While the

analyte concentration C in the continuous flowing solution is considered as a constant, the one in the droplet is limited and decreases along the binding process.

To investigate the influence of analyte depletion and diffusion, we used COMSOL to simulate the association process. Fig.3.9(a) shows that with low concentrations of analyte, both the observed kinetic and the signal amplitude are quite different from those when analyte is abundant, showing the important of considering depletion effect. Fig.3.9(b) showing the results compare between normal, 10 times slower and 10 times faster diffusion speed, with an analyte concentration of 6.25 nM. For small molecules or even smaller molecules in our case, the diffusion process seems have little impact on observed kinetics, but it is still better to consider since the concentration gradient in the bulk varies along the time. For larger molecules which diffuse much slower than anti-BSA, the diffusion needs to be carefully considered, since it affects the kinetic measurement a lot.

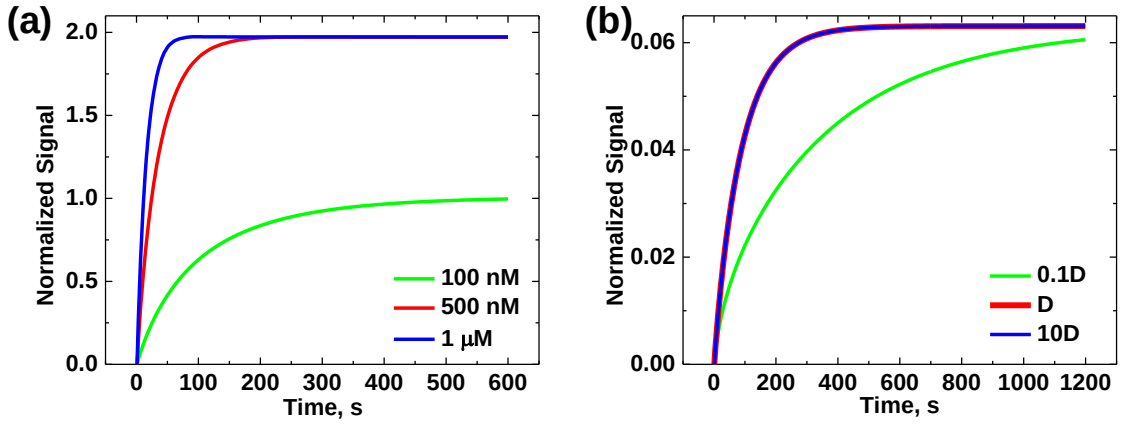

Figure 3.9: COMSOL simulation results. (a) Anti-BSA binding signals with much higher concentrations. Analyte is depleted when concentration is low (green), and the kinetic is quite different compared with the case when analyte is excess (blue and red). (c) Binding signal with a concentration of 6.25 nM. D is the diffusion constant of anti-BSA, which is 5.9×10^{-7} cm^2/s.

Therefore, our approach requires new algorithms for data analysis and the binding kinetics quantification. With the binding process proceeding, the analyte near the surface will be gradually consumed. As we will show later (Figs.3.10(a) and (b)), this makes the concentration of the analyte in the droplet vary with both time (depletion) and space (diffusion). This indicates that the conventional model and Eq. 3.1 are not suitable for the droplet system. To accurately analysis the association process, the depletion and diffusion of the analyte must be taken into consideration.

We build a model to analyze the association kinetics while considering both diffusion and depletion of the analyte. And the model is described as below[143]

Reaction: $$\frac{\partial C_{AB}(t)}{\partial t} = k_a C_A(0,t)(C_B(0) - C_{AB}(t)) - k_d C_{AB}(t) \quad (3.2)$$

Plasmonic Signal: $$\Delta\theta = \alpha C_{ab} \quad (3.3)$$

Diffusion: $$\frac{\partial C_A(z,t)}{\partial t} + \nabla \cdot \left(D \frac{\partial C_A(z,t)}{\partial z} \right) = R_i \quad (3.4)$$

$$R_i = \begin{cases} 0 & , \ z > 0 \\ \frac{\partial C_A(0,t)}{\partial t} (Obtain\ from\ Eq.\ 3.2), & z = 0 \end{cases} \quad (3.5)$$

Depletion: $$\int C_A(z,t)\, S dx = C_{A0} V - C_{AB}(t) S \quad (3.6)$$

The parameters in the model is shown in Table 3.1.

Table 3.1 Parameters of New Model for Extracting the Kinetics

Symbol	***Meaning***	***Symbol***	***Meaning***	***Symbol***	***Meaning***
C_A	concentration of the analyte in the droplet	k_d	dissociation rate constant	*D*	diffusion coefficient
C_B	surface density of the receptor protein	R_t	Plasmonic response	*V*	volume of the droplet
C_{AB}	surface density of the product	α	ratio between plasmonic and surface density	*S*	surface area of the droplet
k_a	association rate constant	z	distance from the surface to analyzed region		

To extract the rate constant, we first fit the dissociation curve to obtain the initial value of dissociation rate constant k_d. Then we modeled the system in COMSOL simulation and combined it with Matlab to fit the binding process and extracted the kinetic parameters, by setting the k_d we got in the dissociation phase as initial fitting value. As shown in Fig.3.10(c), this model fits the experimental data well, and is not limited to any certain concentration. Figs.3.10(a) and (b) show the results of COMSOL simulation at 100 s and 600 s with the initial analyte concentration of 100 nM, and the concentrations of analyte in both cases are obviously much smaller than that at starting point, further confirming the impact of depletion. Comparing Figs.3.10(a) and (b), we could see that the concentration gradient of the analyte in the bulk droplet varied from time to time, indicating that diffusion of analyte also changes along with time, validating the importance of considering diffusion process.

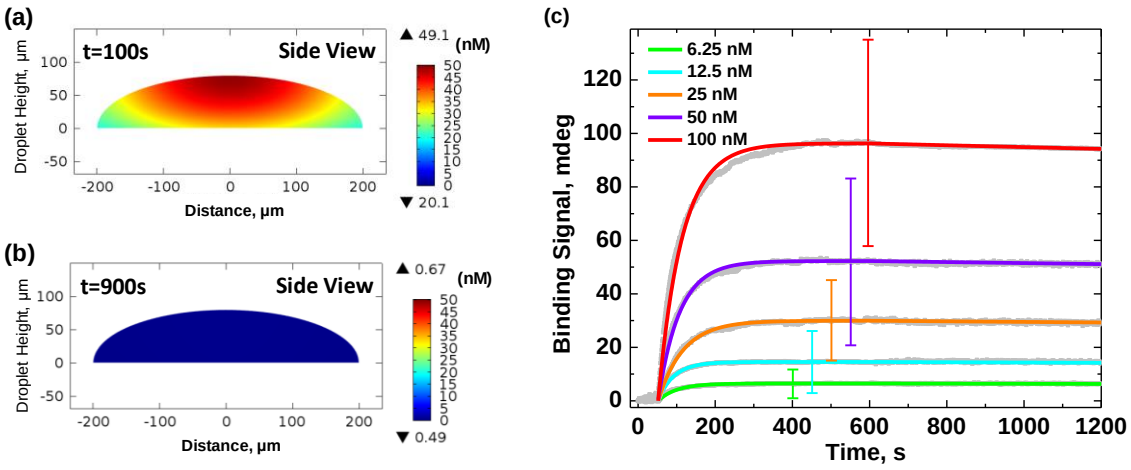

Figure 3.10: COMSOL simulation results of concentration distribution at 100 s (a) and 900 s (b) with an initial anti-BSA concentration of 100 nM. (c) Fitting results of selected (representative) association/dissociation process measurement (combining Matlab with COMSOL). The variations for each curve are calculated from the 20 spots plasmonic response of each concentration.

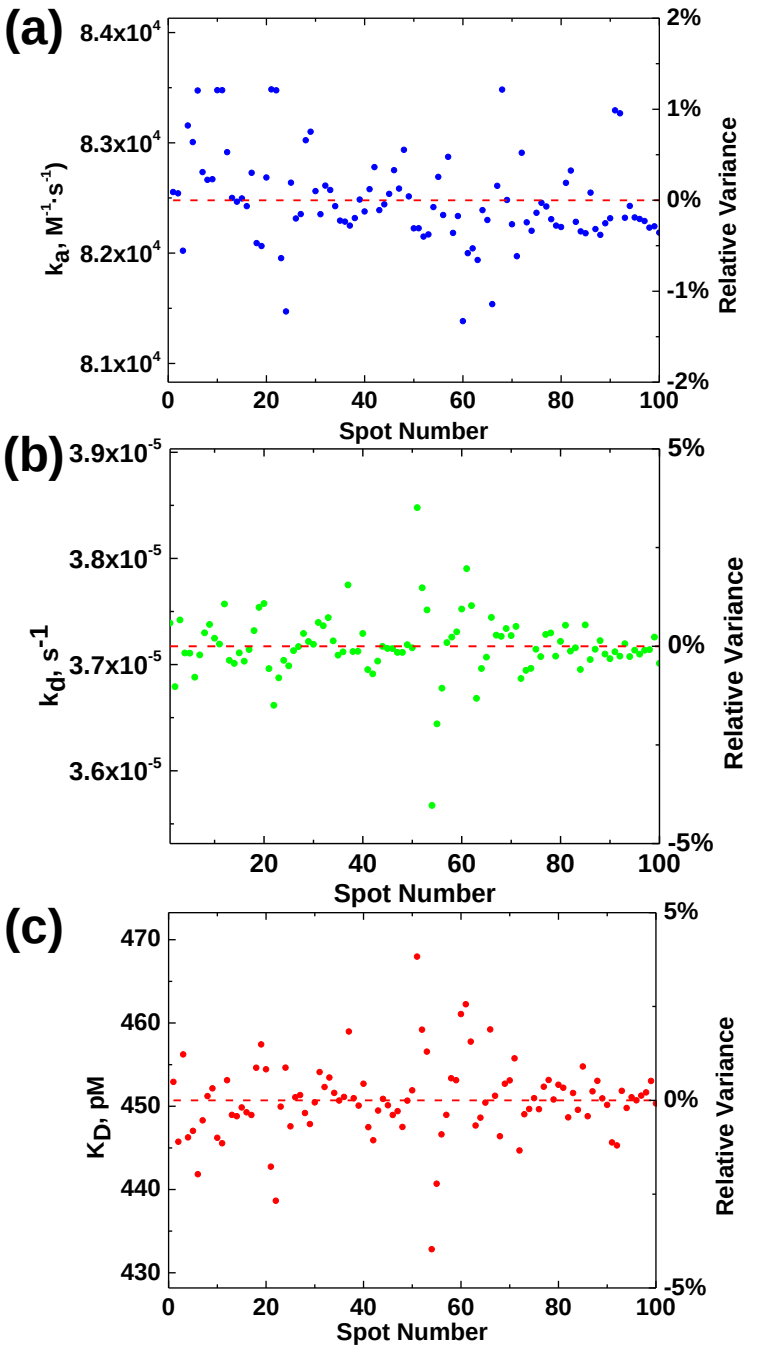

Figure 3.11: Histograms of association rate constant (a), dissociation rate constant (b) and binding affinity extracted from fitting results of 100 spots.

The association rate constants (k_a), dissociation rate constants k_d and binding affinities (K_D) were extracted by using the model proposed above to fit the experiment data. Fig.3.11 shows the histogram of the kinetic constants of the 100 spots. All three diagrams

could be fitted by gaussian fitting, with the average values for k_a, k_d and K_D of 8.5×10^4 $M^{-1}S^{-1}$, 3.7×10^{-5} s^{-1} and 0.451 nM, respectively. The relative variation of the rate constants is within ±5%, providing less than 10% variabilities for high throughput measurements of binding affinities.

3.6 Results Validation by Conventional SPRi

To further validate the kinetic rate constants we obtained, conventional flow-through method (BI-3000) was applied to measure the association and dissociation phase with the same sample. Fig.3.12 shows the experiment results. By global fitting all sensorgrams based on a monovalent model for molecular interaction (Eq.3.1), we could extract the rate constants. Table 3.2 shows the binding kinetics compare between conventional method and our IMPDS system, presenting a very close result. However, compared with the commercial instrument taking 300 μL for each single concentration measurement, our IMPDS consumed only 6 nL analyte for a single spot, which is 50000 times smaller. The consumption of ligands (BSA) during the modification process is also greatly reduced and real-time monitored.

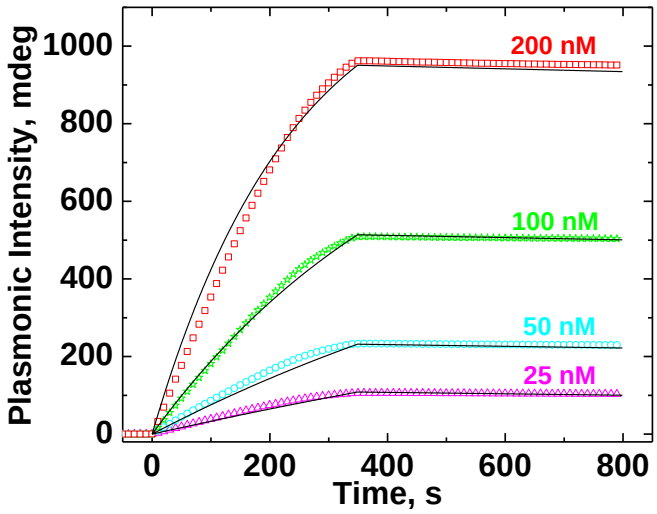

Figure 3.12: Commercialized SPRi instrument (BI-3000, Biosensing Instrument) measurement results. Kinetic rate constants were extracted according to 1:1 model of molecular interaction (black line shows fitting result of each concentration) and shown in Table 3.1.

Table 3.2
Compare the binding kinetics obtained by conventional SPRi (Fig. 3.12) and IMPDS (Fig.3.11(c))

	Conventional SPRi (BI-3000)	**IMPDS**
$k_a, \mathbf{M^{-1}s^{-1}}$	$(5.2 \pm 1.2) \times 10^4$	$(8.5 \pm 0.4) \times 10^4$
$k_d, \mathbf{s^{-1}}$	$(3.0 \pm 0.2) \times 10^{-5}$	$(3.7 \pm 0.2) \times 10^{-5}$
$K_D, \mathbf{pM}$	569 ± 33	451 ± 5
Sample Consumption, µ L/each concentration	300	0.003

3.7 Conclusion

In all, we have developed a system which integrates an ultra-low volume piezoelectric liquid dispensing (PLD) and plasmonic imaging detection for the first time. Using this system, we monitored the ligand-analyte molecular interaction in a tiny droplet (6 nL). We successfully extracted the kinetic rate constants by building a model considering the depletion and diffusion of analyte. We also demonstrated the capability of measuring different binding process in 10×10 droplets array, indicating the ability of the IMPDS to conduct flexible and high-throughput measurement. We anticipate this method can contribute to the study of high-throughput detection of molecular interactions, such as drug screening, disease biomarker selection and fundamental research of protein interactions.

CHAPTER 4

FOCUSED SURFACE PLASMON RESONANCE MICROSCOPY

4.1 Introduction

High numerical aperture objectives have been applied on SPRi to obtain higher resolution for imaging purpose.[22] In a conventional SPR microscopy, the interference between scatter light and SPPs produce a 'tail' pattern.[144] This greatly helps for nanomaterials and small molecule imaging. However, this 'tail' pattern, combined with certain micrometers propagation distance of SPP, limits the ability of SPR microscopy to observe a structure with detailed information.[145] Although certain imaging processing method has been developed to remove the pattern, it does not truly enhance the resolution.

To enhance the spatial resolution of conventional SPR microscopy, focused surface plasmon resonance microscopy has been invented. The basic schematic diagram is shown in Fig.4.1. In conventional SPR microscopy (Fig.4.1(a)), collimated light is incident to the surface of sample and reflected light will be recorded; however, in focused SPR microscopy (Fig.4.1(b)), the light is collimated before entering the objective lens and focus at a small point (diffraction limited) of the sample. The back focal plane image, as shown in Fig.4.1(c), will be recorded to extract the information of the refractive index change. Because light incident at varied angles, the reflected light corresponding to the beam incidents at the dip angle will be dark (Fig.4.1(c)), and at the other angle it will be bright. Therefore, the 'dark ring' contains the information of SPR. Since focused SPR microscopy is only sensitive to the focus spot, it greatly enhances the spatial resolution. Compared with a tiny spot image obtained from conventional SPR microscopy, the back focal plane image

provides possibilities to extract the spot information with enhanced signal to noise ratio (SNR).

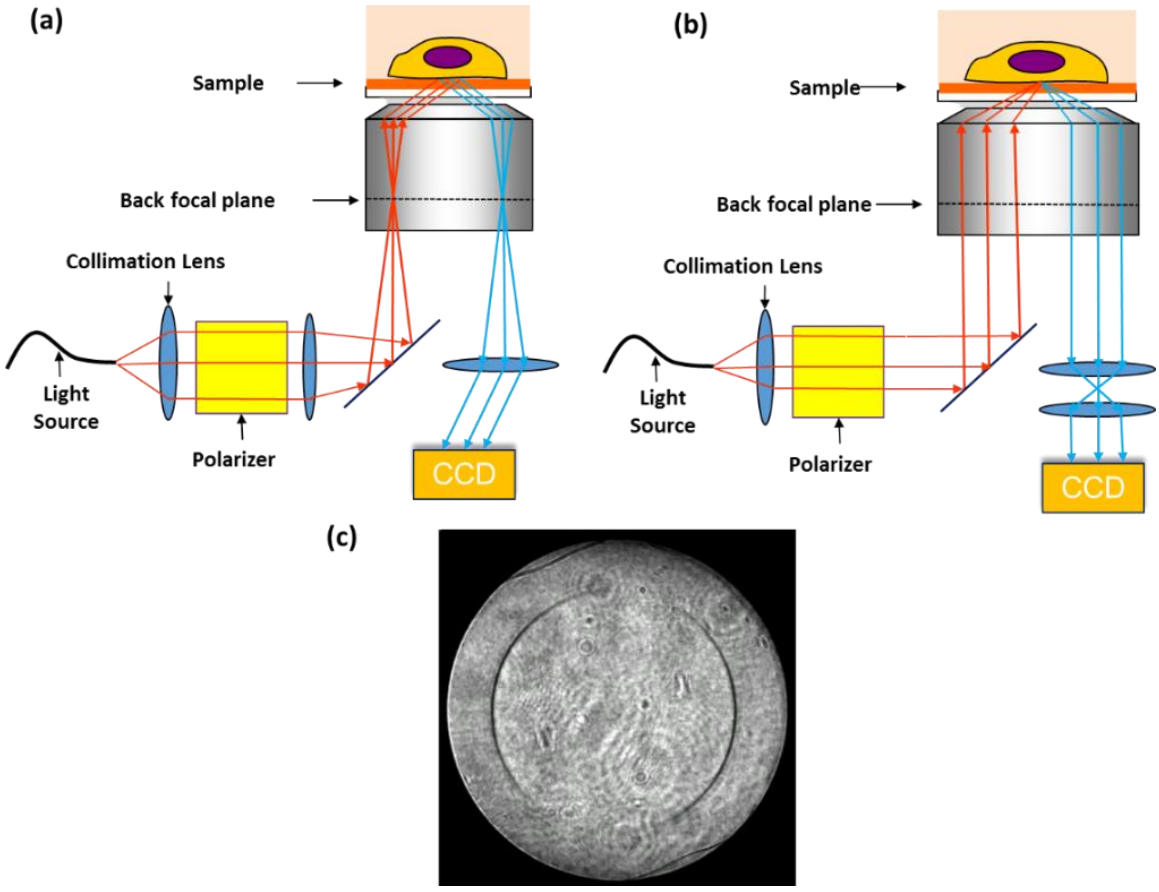

Figure 4.1: Principle of focused SPR microscopy. (a) conventional SPR microscopy; (b) focused SPR microscopy; (c) back focal plane image of focused SPR microscopy.

The concept of focused SPR microscopy was first introduced by Yeatman et al. in 1988 (Fig.4.2).[146] They theoretically demonstrated the feasibility of focus SPR microscopy and provided the theoretical model and basic estimation. Their calculation indicated that the spatial resolution was greatly enhanced though a little bit sensitivity is lost.

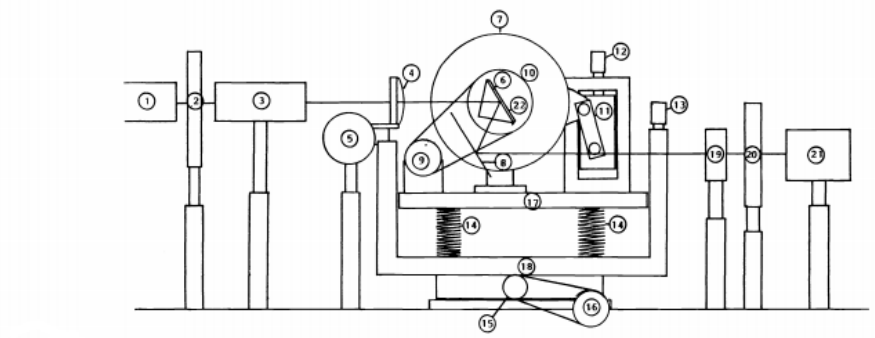

Apparatus used for scanned surface plasmon measurements, with components as labelled below:
1. HeNe laser (1 mw).
2. Polarizer.
3. Beam expander.
4. Focussing lens.
5. Focus control.
6. Prism.
7. Rotating platform.
8. Mirror.
9. Servo potentiometer.
10. Drum for potentiometer belt.
11. Rotation control link mechanism.
12. Rotation control micrometer.
13. Vertical translation micrometer.
14. Support springs.
15. Horizontal translation micrometer.
16. Servo potentiometer.
17. Vertically translating platform.
18. Horizontally translating cradle.
19. Lens.
20. Polarizer.
21. Photodetector.
22. Ag film on glass slide.

Figure 4.2: Theoretical prototype of focused SPR microscopy proposed by E. Yeatman.[146]

Hiroshi Kano et al. experimentally realized the focused SPR microscopy.[147,148] The schematic view is shown in Fig.4.3. A laser beam with 632.8 nm wave length is collimated incident and focused to a tiny spot after goes through an objective lens with NA equals to 1.3~1.4. The radius of the 'dark ring' is used as the indicator of refractive index change, and they could measure the poly-methyl-methacrylate (PMMA) film as thin as 3.5 nm in air. Applying this setup, they could distinguish the aggregated 1.5 μm silica beads as shown in Fig. 4.4.

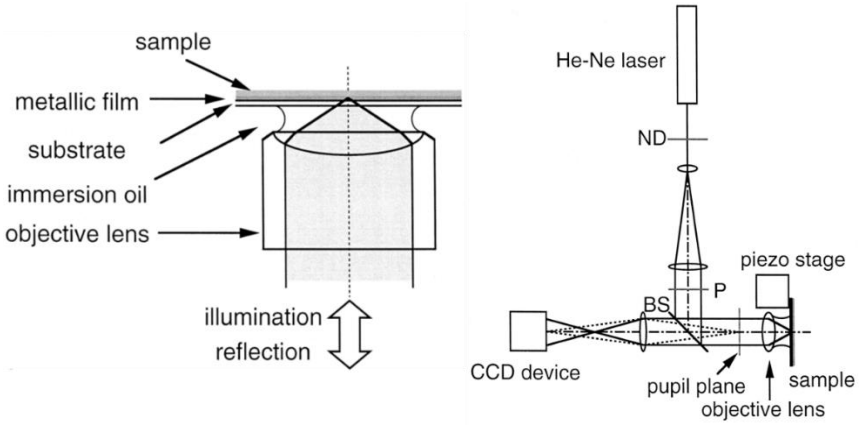

Figure 4.3: Schematic view of focused SPR microscopy proposed by Kano et al.[147]

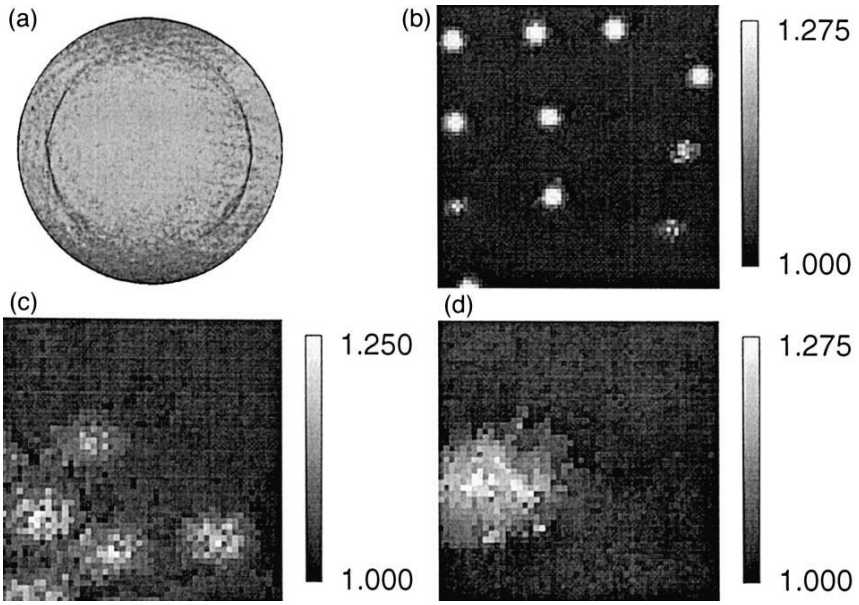

Figure 4.4: Observation of 1.5 μm silica beads by scanning focus point of the setup[148]

The development of focused SPR microscopy have focused on two parts since then: one is based on detection the amplitude (i.e. the radius of the ring), while the other measures the phase shift. Both have contributed great works.

4.1.1 Radius Measurements

K. Watanabe et al. improved the configuration of Kano's setup by adding the liquid crystal (which shown in Fig.4.6 as ZPol) to produce the SPP with radial polarized light.[144,145,149] As shown in Fig.4.5, the radical polarized light will have a stronger electric field component along z direction compared with linear polarized one, and thus enhance the sensitivity.

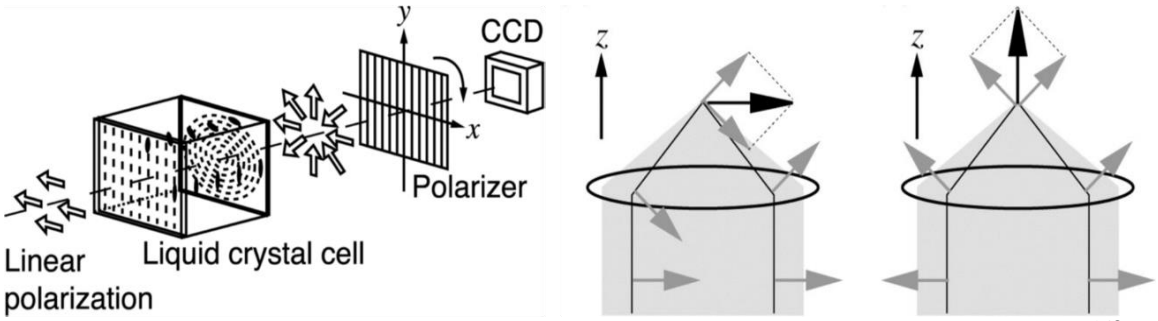

Figure 4.5: Enhance sensitivity of focused SPR setup by using radical polarized light[149]

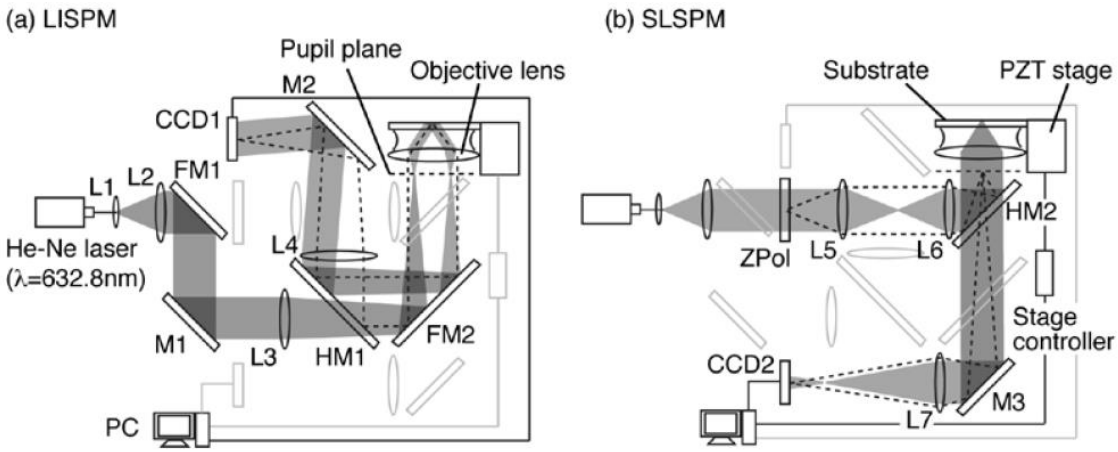

Figure 4.6: The optical system built by Watanabe: (a) conventional SPR microscopy; (b) focused SPR microscopy. The optical path can be switched using flipper mirror FM1 and FM2.[144]

The schematic view of Watanabe's setup is described in Fig.4.6. They could switch conventional SPR microscopy to focus SPR microscopy back and forth to compare the difference. Piezo stage is applied for scanning purpose. What they measure is the radius of the dark ring, as shown in Fig.4.7, and they do the following procedures to extract the information: (a) select a back focal plane image as a reference; (b) find the best fit ring to the 'dark ring' in the selected image; (c) fix the center and the radius of the ring; (d) find pixels containing a portion of the best fit ring inside in each of the pupil images, as shown in Fig.4.7; (e) sum up the pixel values by giving weights that are proportional to the length

of the ring segment in each pixel; (f) normalize the sum by the circumference of the ring.[144] By getting the circumference of the ring, the radius of the ring ρ_{sp} can be easily calculated.

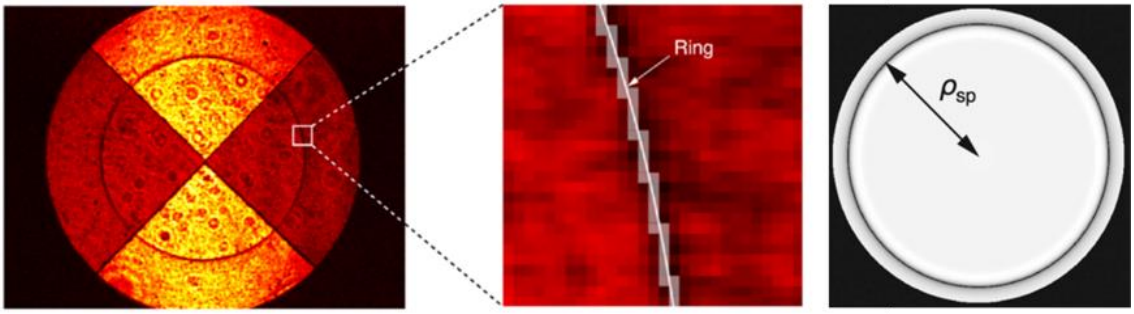

Figure 4.7: Algorithm to measure focus SPR response

By using the equation we can get the sample refractive index n_s[144]

$$\rho_{sp} = Real\left[\frac{\omega}{c}\left(\frac{n_m^2 n_s^2}{n_m^2+n_s^2}\right)^{1/2}\right] \qquad (5.1)$$

where ω, c and n_m is the angular frequency of light, light speed and complex refractive index of metal, respectively. Using this setup, they could increase the spatial resolution to 210 nm in air with a N.A equals to 1.4 objective lens, as shown in Fig.4.8.

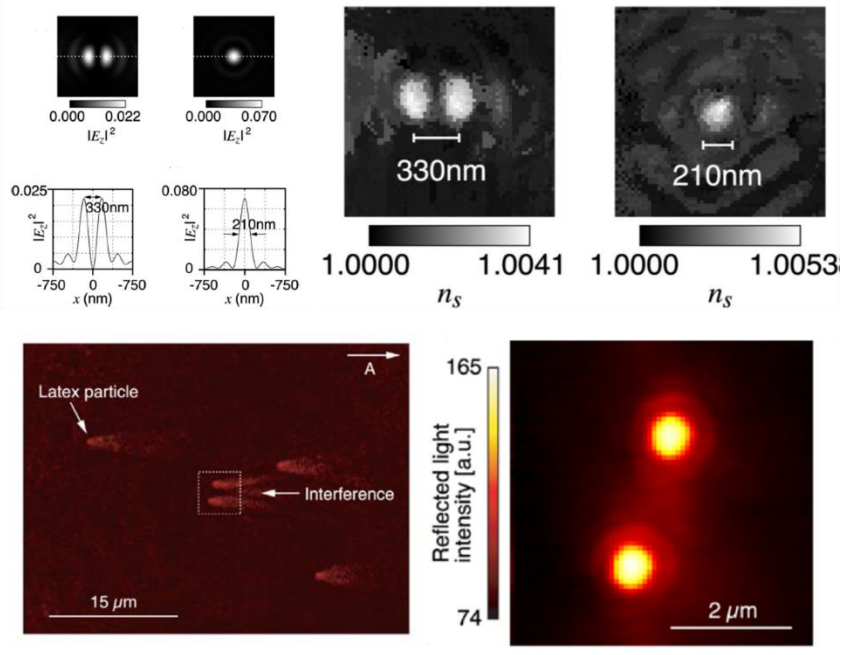

Figure 4.8: Observation of latex nanoparticle by enhanced focused SPR microscopy (Lower left shows conventional SPR imaging)[144,149]

They could also measure some biology samples in water with higher N.A. equals to 1.65 objective lens. Figs.4.9(a) and (b) show the measurement of lipid layer with different thickness. They conducted the experiment to image the cell adhesion sites, as presented in Fig.4.9(d). The cell adhesion site could be clearly distinguished from each other in the scanning image of focused SPR microscopy, while the conventional SPR imaging shows a very blurry image.

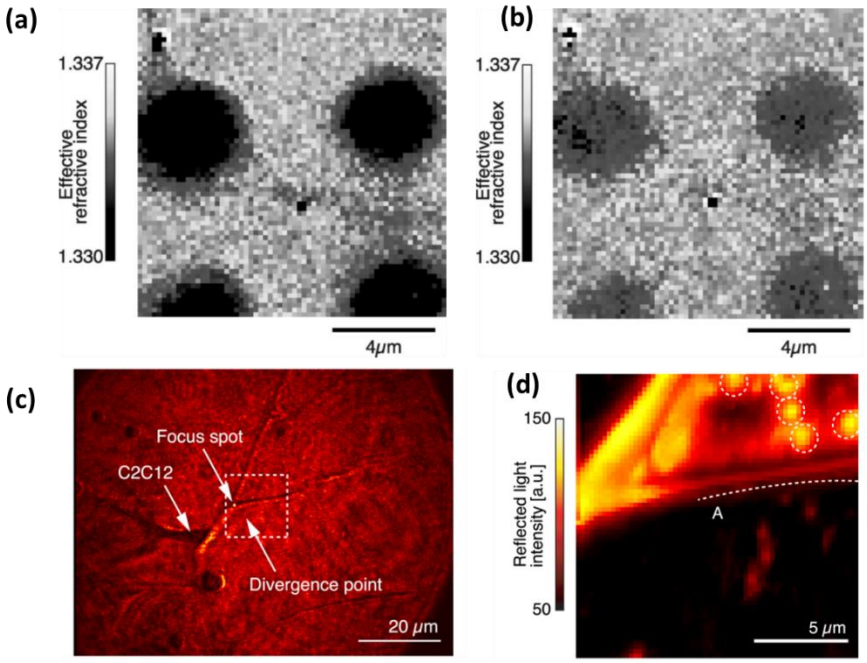

Figure 4.9: Measurement of biological sample by focused SPR microscopy. (a) and (b) are DiynePC and DLPC lipid layers; (c) is the conventional SPR microscopy image of cell adhesion site; (d) is focused SPR microscopy image of region shown in (c).[144,149]

By confining the SPR in a small region and avoiding the 'tail' image, the amplitude measurement greatly enhanced the spatial resolution (diffraction limit). However, the simple processing method limit their SNR (only use small number of pixels), and their sensitivity actually lose a little bit.

4.1.2 Phase Shift Detection by Focused SPR Microscopy

The phase detection has higher sensitivity than amplitude for SPR imaging setup. To increase the sensitivity while keeping high spatial resolution, Somekh et al. proposed a focused SPR microscopy that measures the phase shift, which is inspired by scanning acoustic microcopy.[150,151] They used the acousto-optic modulators to shift the frequency of reference and detection beam to ω_1 and ω_2, and detected the interference signal which contained the phase information at frequency $\omega_1 - \omega_2$ to decrease the noise level. By tuning the focus distance, they could be able to maximize the phase difference of the signal, which will be discussed later in this section. Fig.4.10 is the schematic of the setup and shows how changing the focus distance will vary the contrast of images.

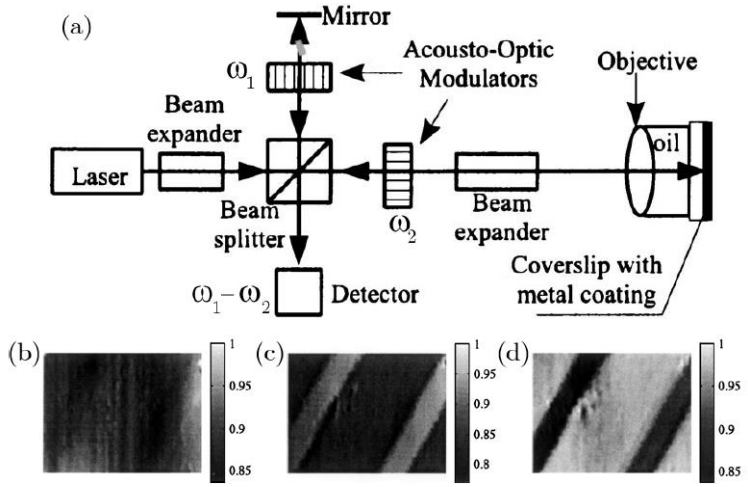

Figure 4.10: (a) Schematic view of the focused SPR microscopy setup developed by Somekh et al. (b), (c) and (d) Images in air of a structured dielectric sample (6 μm wide SiO_2 strips on gold, 1 nm thick) for different defocalizations (objective to the metal surface): z=0 μm, z=1.5 μm, z=1.85 μm.[150,151]

T. Roland et al. further developed the phase detection configuration of focused SPR microscopy (Fig.4.11).[152–154] Radial polarized light was used as discussed in the previous section. The detection beam is focused at small tiny spot by a high NA objective lens. Then the interference information is detected by photomultiplier at certain frequency.

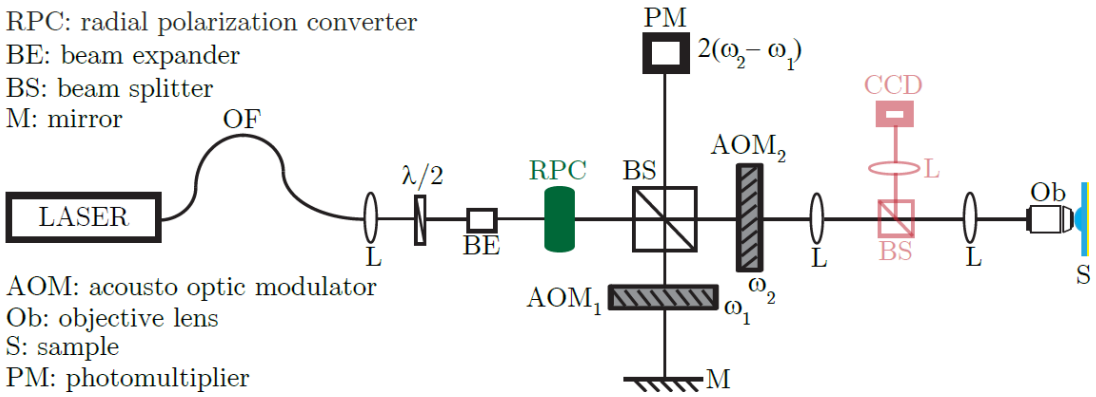

Figure 4.11: Schematic of the focused SPR setup developed by T. Roland et al.[154]

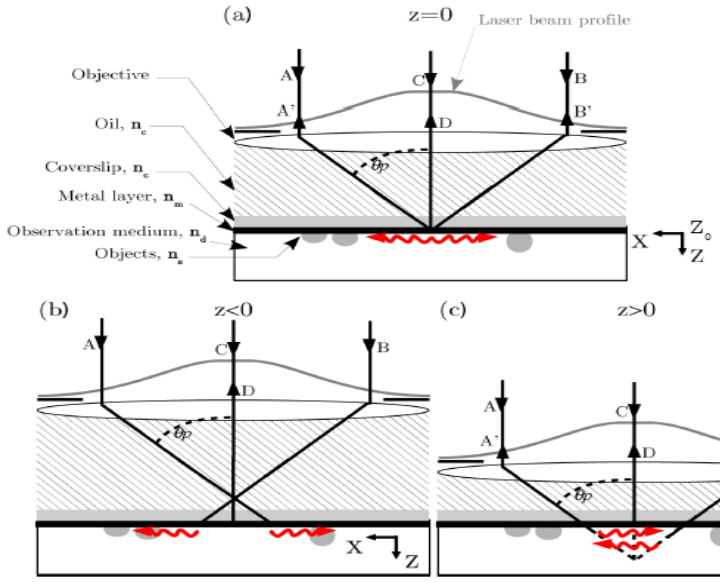

Figure 4.12: Illustration of detection principle of focused SPR setup by T. Roland et al. The SPPs for the incident ray angle corresponds to θ_P. The objective is (a) at focus Z = 0, (b) defocalized in the coupling medium Z < 0, or (c) in the observation medium Z > 0.[154]

The measurement of this configuration is done by changing the defocus distance. In Fig.4.12, three situations corresponding to the focus distance is described: 1) Z = 0, which means at the focus point; 2) Z < 0, which indicates focusing in the immersion oil; 3) Z > 0, which means focusing in the sample. Piezo stage is used to tune the focus position. A, B and C represent the incident lights whereas B', A' and D are the back reflected light.

When the objective is at focus (Z = 0), as show in Fig.4.12, all lights is reflected back no matter their angle of incidence. And SPR are only excited by the light A and B that arrive at the metal surface with an incidence angle equals to 'dip' angle θ_P.

When Z < 0, which means the focus is in the immersion oil, SPR can still be excited on the surface of metal. According to the theory by H. Rather, surface plasmon polaritons can reradiate light after the propagating distance,[19] and in this situation, SPPs will propagate away from the center of the illumination region. Therefore, none of the reradiated lights will be conjugated through the objective as a consequence, which means the light carries the information of SPR will not be recorded.

When Z > 0, the focus is in the sample, we will see that the light such as A, will still excite SPPs, and they will travel to the center of illuminating region. When the SPPs travels the propagating distance, it will reradiate and be conjugated back by the objective lens, and can be detected at the photodetector, so is the incident light C. Other light which are not coupled with SPPs will not be conjugated reflected back, since the focus is not at Z=0. The phase retardation of SPPs is contributed by both excitation conditions and propagating distance along surface, which can be changed by tuning the value of Z. By recording interference of back reflected light (which is the interference of SPPs reradiated light and 0^o incident light) and reference beam, we could separation the phase information out, which is depending on the defocus distance and the refractive index information on the metal surface.

The basic equations for extracting the information will be shown below. The total interference light intensity is[154]

$$I(t) = E_0^2 + E_{reflected}^2 + E_0^* E_{reflected} \cos(2\pi\Omega t + \Delta\Phi) \qquad (5.2)$$

Where E_0 is the electric field of reference beam, $E_{reflected}$ is the electric field of back reflected light, which can be expressed as[154]

$$E_{reflected} \sim P^2(\sin\theta)\left[r_p(\sin\theta)\cos^2\varphi + r_s(\sin\theta)\sin^2\varphi\right]e^{i2n_c k\cos\theta Z} \quad (5.3)$$

Where $P(\sin\theta)$ is the pupil function, and r_p and r_s is the Fresnel reflection coefficient, $e^{i2n_c k\cos\theta Z}$ is the phase shift induced by the defocus distance by the objective, φ is the angle defined as the angle between x and y component of electrical field, which is 0~2π for radial polarization. Since the signal is detect at the difference of frequency Ω, the recorded information will be the conjugated term of *I(t)*. Suppose the E_0 is uniform, and the reflected light is considered to be small enough, we could have the recording intensity as[154]

$$V(Z) = \iint P^2(\sin\theta)\left[r_p(\sin\theta)\cos^2\varphi + r_s(\sin\theta)\sin^2\varphi\right]e^{i2n_c k\cos\theta Z} sin\theta d\theta d\varphi (5.4)$$

In which we can easily extract the relationship between reflection coefficient of s and p polarized light with the defocus distance Z, which is shown in Fig.4.13. We can see from the Fig.4.13 that the intensity is periodically change with certain Z distance[154]

$$\Delta Z = \frac{\lambda}{2n_c(1-\cos\theta_P)} \quad (5.5)$$

where λ is the wavelength of incident light. For different refractive index, we are going to have different ΔZ, which will cause the difference of recording light intensity. As seen in Fig.4.13, by parking Z at certain value, we can have the largest contrast of samples, and this is how this method works.

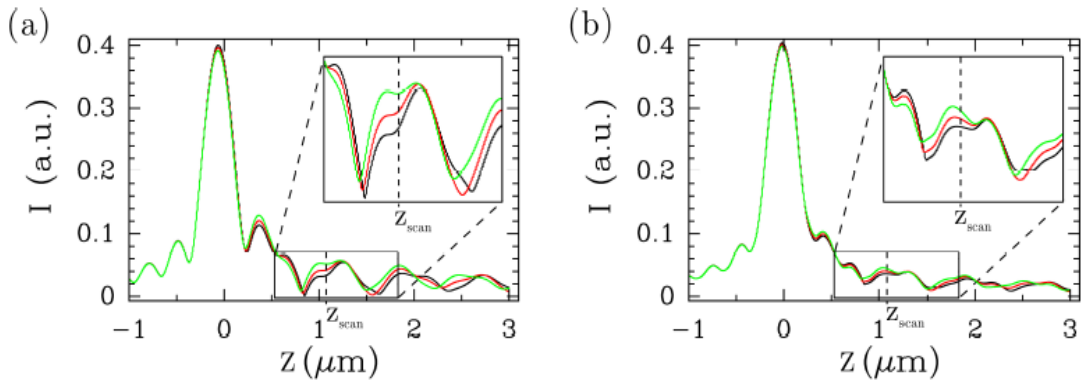

Figure 4.13: Theoretical simulation of the intensity *I(Z)* for lipid layers (ε = 2.56) with different thickness (0, 5, and 10 nm, black, red, and green curves respectively). (a) Radially polarized light; (b) linearly polarized light.[152]

Fig.4.14 shows the measurement results of 30 nm gold and latex particles, and they could be easily distinguished from each other. This method enhances the sensitivity, due to the measurement of phase information along the metal surface. However, the resolution of the sample is decreased because of the defocus approach. Therefore, there is certain balance between the sensitivity and the resolution.

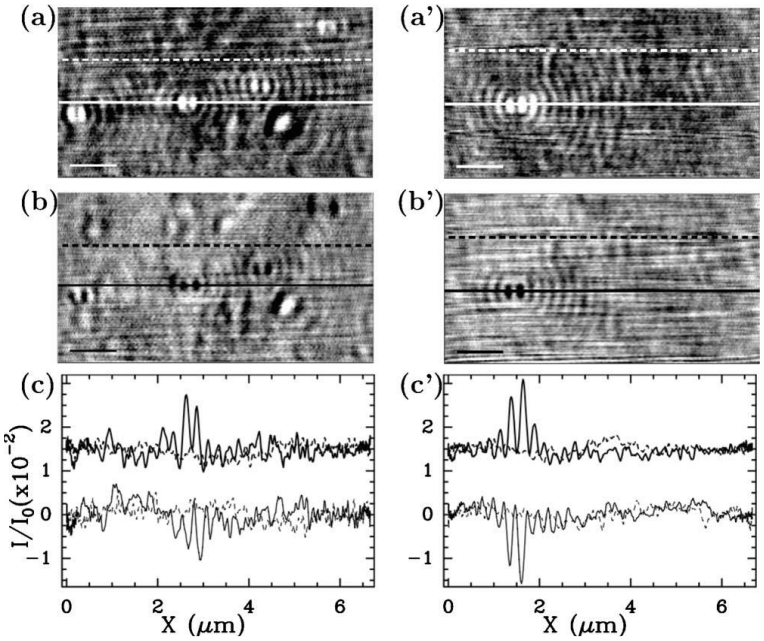

Figure 4.14: Detection of 30 nm gold and latex particles by focused SPR microscopy. (a) and (b) gold nanoparticles measured at Z=1.270 μm and 1.100 μm, (a') and (b') Latex nanoparticles detected at Z=0.767 μm and 0.500 μm. (c) and (c') is the intensity profile of solid line in (a), (b), (a') and (b'). [154]

In all, comparing with conventional SPR microscopy, focused SPR microscopy provides the possibility to increase the spatial resolution while keeping or even improving the sensitivity. Through scanning the sample, we should be able to image the sample with high resolution; we could also only detect one-point information at a time without disturbing by the signal of other site, which may be able to be applied in array design or other certain case.

Here we developed focus SPR microscopy based on the amplitude measurement configuration, which makes use of the enhanced spatial resolution. An algorithm has been developed to enhance the signal to noise ratio of the setup. Two modes are proposed for different measurement purpose: scanning mode is designed for obtain detailed spatial information, in which the focus spot works as a probe to scan along the sample; point mode is applied to real-time monitor the localized refractive index change, while the beam is focused on one certain position and this provides the possibility for single protein measurement.

4.2 Experiment Setup Configuration

The schematic diagram and real setup of focused SPR microscopy is described in Fig.4.15. Collimated light travels through a 60× NA=1.49 lens and focus on the sample at a tiny spot, size of which is 200 nm (diffraction limited). The back focal plane imaged is recorded by CCD camera or photodiode for different purpose (imaging or ultrafast detection, respectively). Scanning Mirrors is added to move the focus spot along the surface, and the step for incident angle change is 0.1 ^{o}/V.

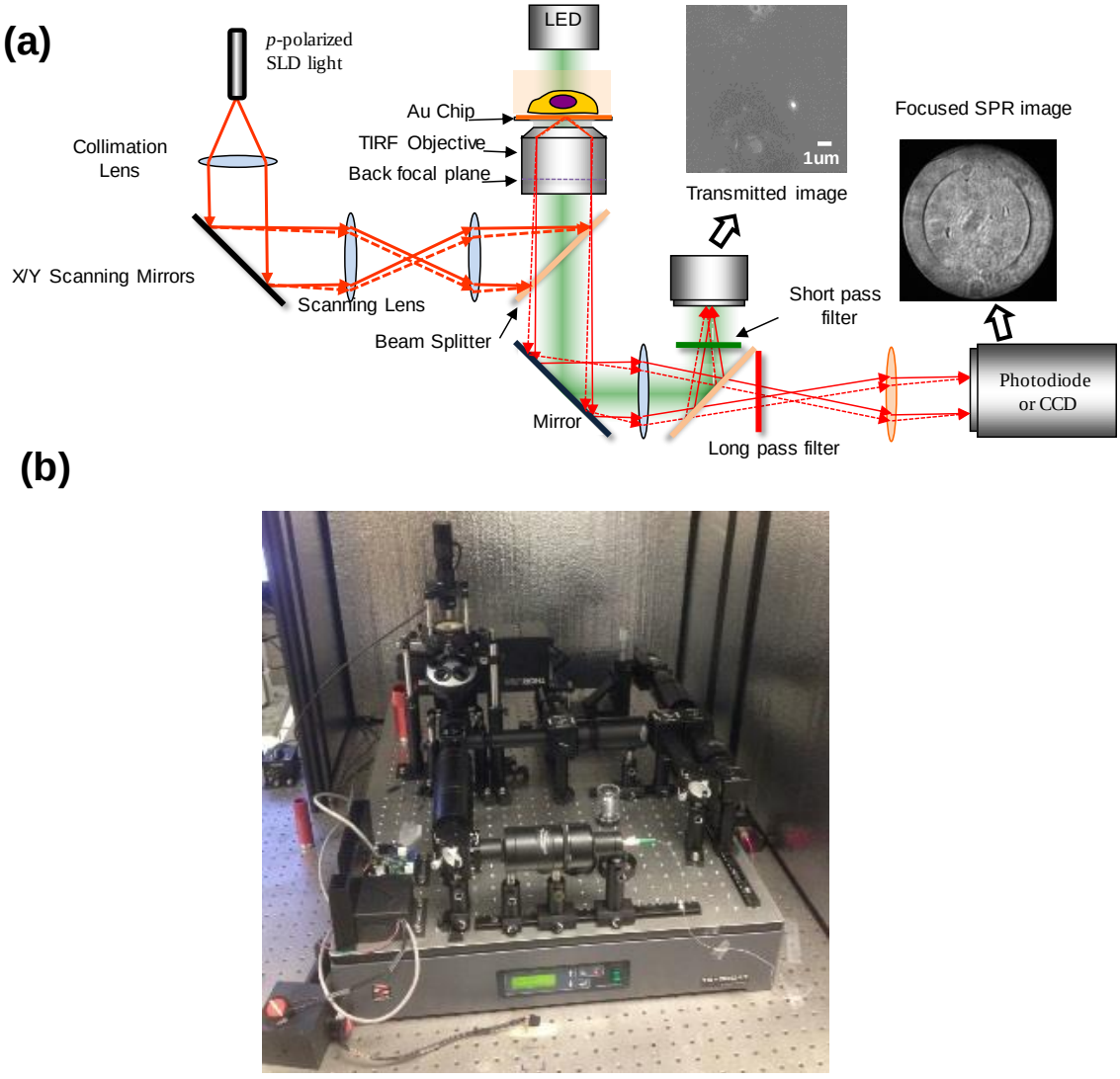

Figure 4.15: Schematic diagram (a) and real setup (b) of focused SPR microscopy.

4.3 Data Processing and Noise Calibration

To extract the plasmonic information and obtain better signal to noise ratio, we applied the bi-cell algorithm which is commonly used in AFM to process the image.[155] Two nearby dip regions were chosen, and the signal is determined by

$$\Delta = \frac{I_A - I_B}{I_A + I_B}, \tag{5.6}$$

where I_A and I_B are the intensity of the two regions. The assumption is that the two regions have reversed intensity variation with similar amplitude. Therefore, the differential of two regions could represent how the dip angle shift, while canceling the common noise. Moreover, dividing the summation normalizes the signal and further reduces the noise brought by light intensity fluctuation.

As depicted in Fig.4.16 (zoom in picture of the 'ring' region), we choose two nearby regions around the dip location. When the surface refractive index change, the dip position will also change. For example, with a higher refractive index the dip shifts to larger angle, resulting in intensity of A region increase and B region decrease, which will cause the value change. The relationship between the signal and angle change could be obtained by moving the two ROI regions along the axis vertical to the dip region, and it is linear during certain range with a high sensitivity (shown in next section).

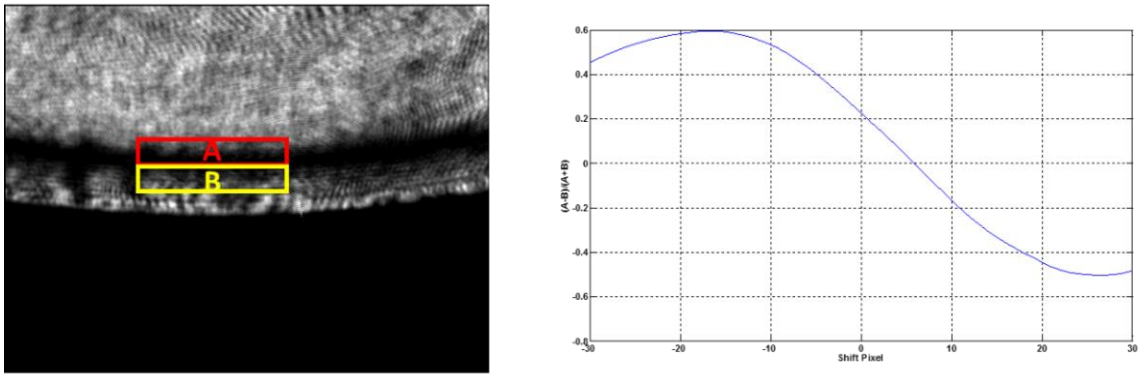

Figure 4.16: Bi-cell date processing algorithm for focused SPR microscopy. Left: the selected two regions near the dip region; Right: focused SPR response vs. dip angle shift.

4.4 Measurement Results and Discussions

4.4.1 Noise Quantification

We calibrated the noise level of our setup by switching flow buffer from water to 1% ethanol and then switching back (Fig.4.17), and the dig angle will have a 60 mdeg shift,

corresponding to a refractive index change (RIU) of 0.0004. The noise level of the conventional SPR microscopy is 0.14 mdeg, and our focus SPR microscopy can be as low as 0.03 mdeg.

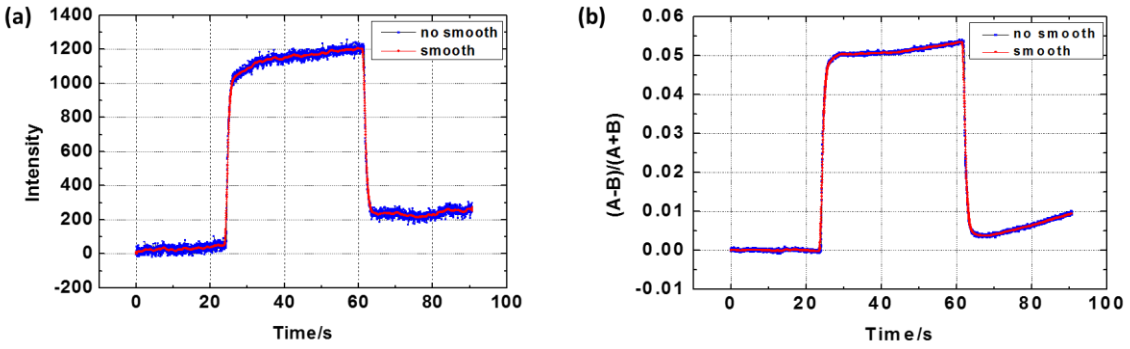

Figure 4.17: 1% ethanol calibration of different setups: (a) conventional SPR microscopy; (b) focus SPR microscopy.

4.4.2 Scanning Mode of Focused SPR microcopy

The focus SPR microscopy can be operated at scanning mode, while we used the scanning mirror to move the spot along the surface. A scanning results of aggregated bacteria on the gold surface is shown in Fig.4.18. It provides higher sensitivity compared with transmitted microscopy and offers more detailed information compared with conventional SPR microscopy.

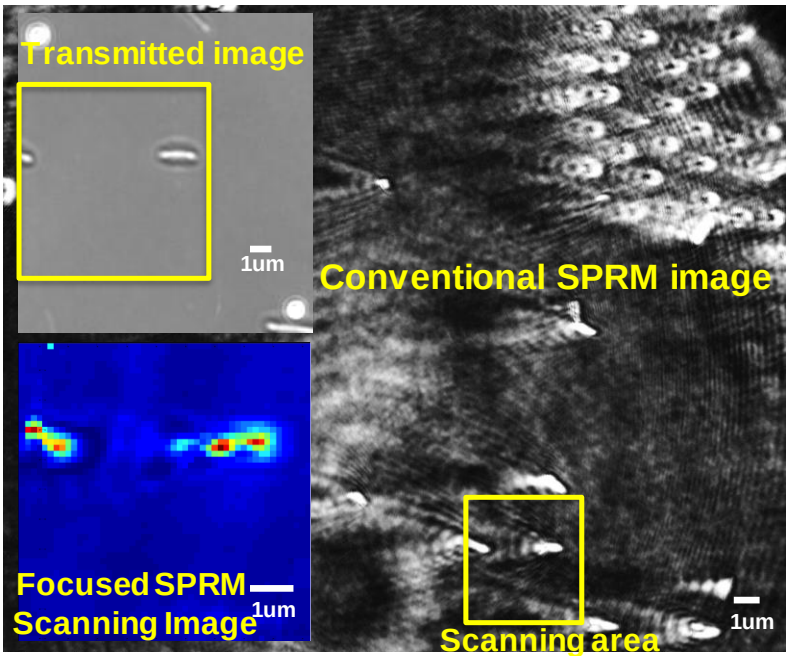

Figure 4.18: Compare measurement of different microscopes.

4.4.3 Detection of Single Nanoparticle Binding

We detected the single nanoparticle binding on the focus SPR setup by focusing the beam at one spot and monitoring the dip angle change (point mode). To decrease the mechanical noise of the system, the drug delivery system was applied and the inlet of it is near the focus region. 1X PBS buffer was used as the buffer, which screened the charge repelling between gold surface and polystyrene particle. Fig.4.19 shows the signal as function of time detecting binding of 100 nm and 64 nm polystyrene particles by focus SPR microscopy.

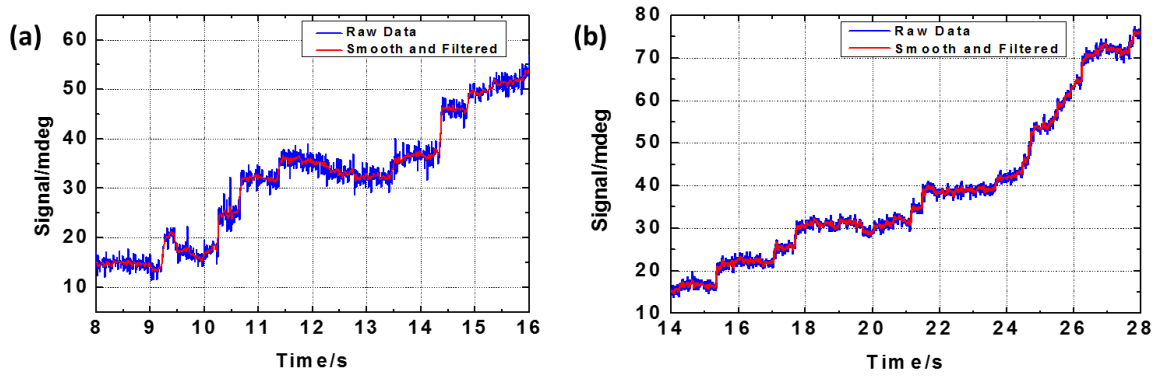

Figure 4.19: Measurement of polystyrene nanoparticles binding: (a) 100 nm, (b) 64 nm.

To extract the signal of single nanoparticle binding, we use the method shown in Fig.4.20. We first applied median filter fitting which is sensitive to stepwise signal change. Then we differentiated the of the fitting curve, and the only the binding signal will introduce a peak. By finding the positions of different peak and values of it we could obtain information of each single binding event. Last, histogram of the peak value would represent the distribution of binding signal (Fig.4.21). We assume the signal with most counts is the single nanoparticle binding, which is 5 mdeg for 100 nm and 2 mdeg for 64 nm polystyrene particles.

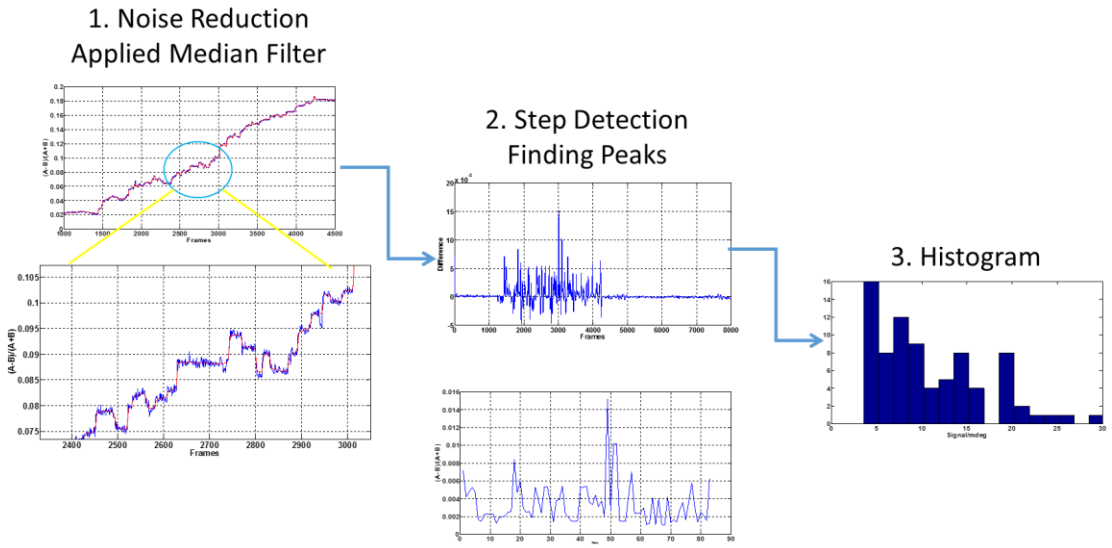

Figure 4.20: Signal processing to acquire the information of single nanoparticle binding

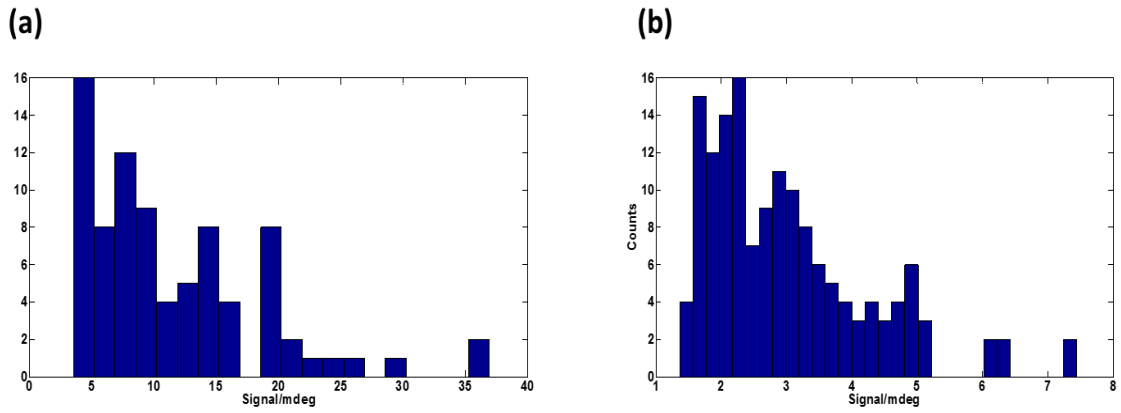

Figure 4.21: Histogram of 100 nm (a) and 64nm (b) polystyrene nanoparticles binding signals

To validate our results, we did a theoretical simulation while assuming that the sensitivity for focus spot is Gaussian distributed and all bindings are single events. The histogram of the binding signal provided by the nanoparticle binding on different site of the spot. The simulation results are consistent well with our experiment observation.

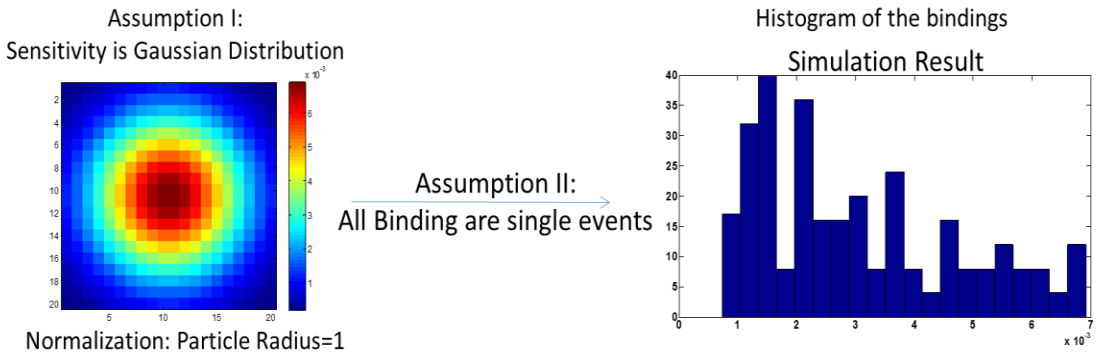

Figure 4.22: Simulation results of nanoparticle binding

To note that we also developed an automatic counting algorithm for conventional imaging SPRi. Because there are tens of thousands of frames for one time recording and enormous particles in solutions, manually counting is impossible. An algorithm which can automatically do the counting is build and Fig.4.23 shows its work flow.

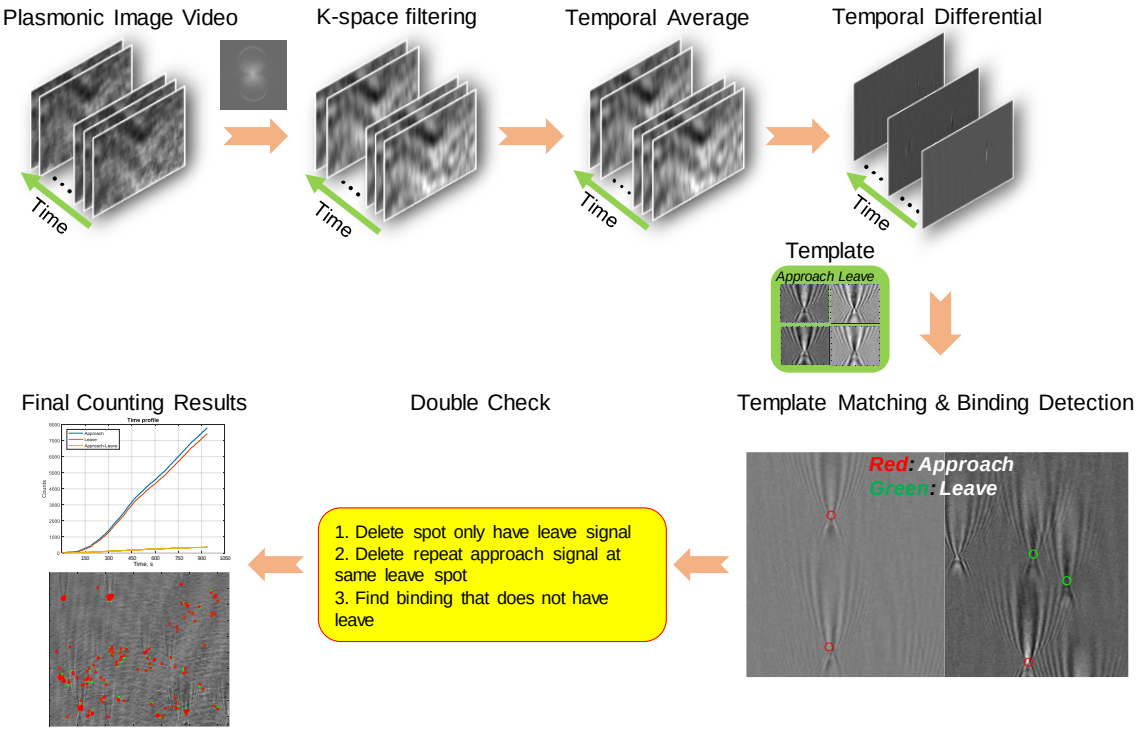

Figure 4.23: Flow chart diagram of automatic counting algorithm for time-resolved digital counting. Three major steps are included: 1) Image sequence is first pre-processed to enhance the image contrast. K-space filtering and temporal differential (subtract previous frame from present one) was used to remove the background refringent pattern and moving average of image sequence temporally was applied to reduce the shot noise. 2) Recognizing the particle approaching/leaving the surface on all the frames. Template was chosen from the image sequence, then each frame was compared with the template by normalized autocorrelation. If there is a strong correlation between template and certain spot of the image indicates approaching/leaving particle on that position. 3) The computer initiates self-check and excludes unreasonable counting, results after the correction are then output.

We first enhanced the plasmonic binding signal which prepares for the next image correlation step. SNR of the signal mainly depends on 3 factors: the image contrast, shot noise and pixel noise. The image contrast is enhanced by removing the background: k-space filtering described somewhere else could increase the contrast of nanoparticles plasmonic image and temporal differentiation by subtracting the previous frame from the present one is applied to fully remove the refringent patterns. The pixel noise could be decreased by increasing the number of pixels per ROI with zoom in, but it reduced the field

of view in the meantime. Shot noise is caused by the fluctuation of the photon number emitted by the light source, which is governed by a Poisson distribution. The fluctuation is usually positive related to the square root of the photon amount, and the SNR of shot noise for a ROI is[156,157]

$$SNR = \frac{N}{\sqrt{N}} = \sqrt{N} = \sqrt{fps * t_{ave} * ept * P_{pixel} * NOP_{ROI} * \eta} \qquad (4.1)$$

Where fps is the frame rate, t_{ave} is the time duration of image averaging, ept is the exposure time for each pixel, P_{pixel} is the light power at each pixel, NOP_{ROI} is the number of pixels for the ROI region and η is the quantum efficiency. While the last four parameters are almost determined for certain hardware, we could increase the frame rate or time duration of average. Fig.4.24 shows the results of the plasmonic image contrast enhancement of binding through averaging.

To demonstrate what is the minimum size of gold nanoparticle we could observe, we further applied the algorithm for measurement of 40 nm, 20 nm and 10 nm bare gold nanoparticle non-specific binding. With 100 frames averaging (800 fps, corresponding to 125 ms temporal resolution) the results show a good contrast even for 10 nm gold nanoparticles (Fig.4.25). The contrast shows a cubic power decrease with the particle diameter, and a 2 nm detection limit for gold nanoparticles (Fig.4.26, Noise level of contrast ~10^{-5}).

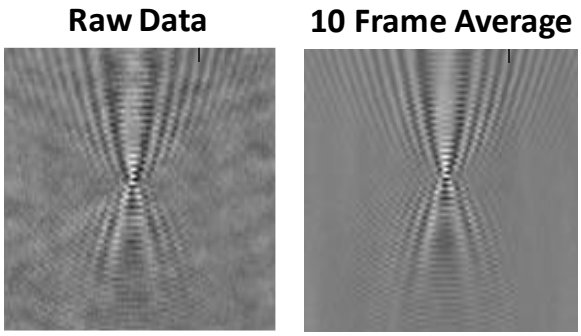

Figure 4.24: Compare raw image(left) and averaged image(right). The image contrast is greatly enhanced.

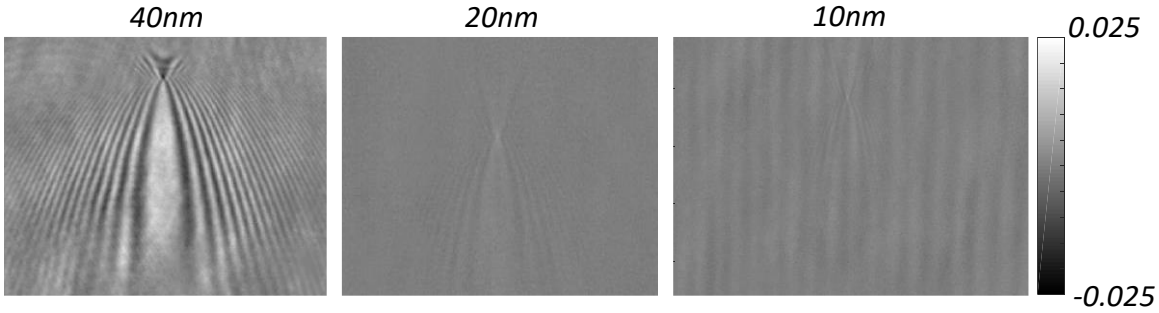

Figure 4.25: Measurement of different size gold nanoparticle binding.

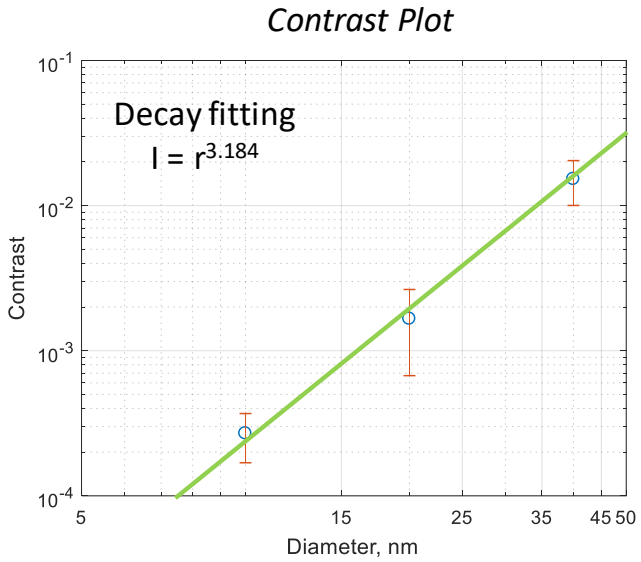

Figure 4.26: Contrast vs. particle size plot. The fitting(green) shows contrast decrease with cubic power (~3.2) of the diameter.

The major part of the automation algorithm is template matching to detect each nanoparticle binding. This is realized by image normalized correlation between the

template and the image, which compares them at the spatial domain and eliminate the intensity influence.[158] Templates are first chosen from the pre-processed image sequence and used to correlate with each frame. Fig.4.27 shows the correlation results for certain frames.

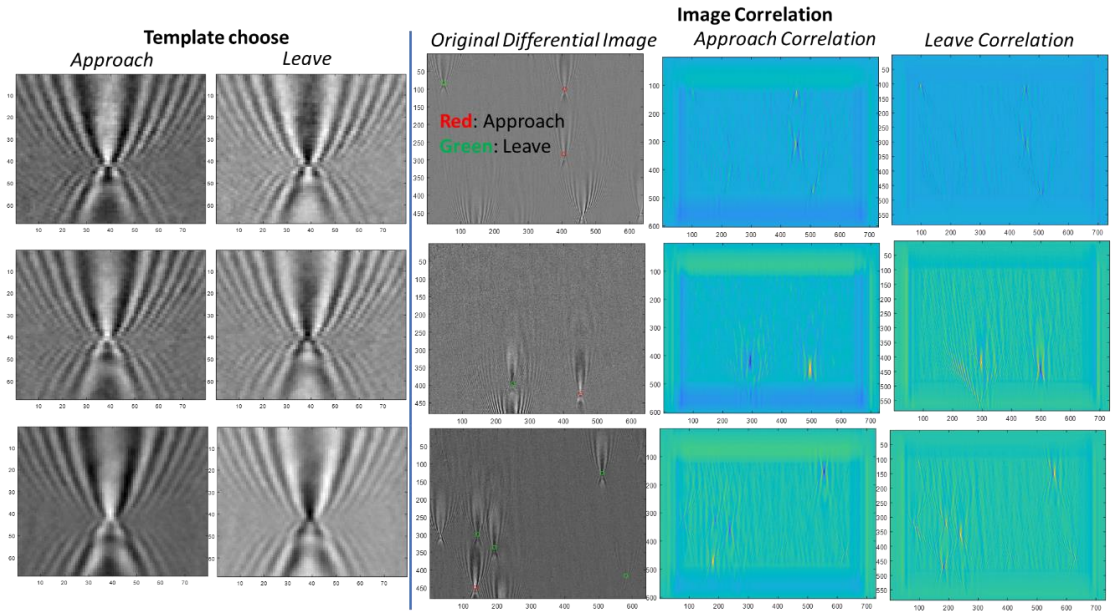

Figure 4.27: Normalized Correlation of template and temporal differential image.

We determine the approaching/leaving nanoparticles on each frame by finding the local maximum in the correlation image. Carefully choosing the criteria for determine local maximum is needed. As shown in Fig.4.28, improper criteria will miss some particles or introduce wrong counting. To notice that the correlation between template and image may change along the time due to the focus drift, and this needs adjustment of the criteria. In order to circumvent the problem, the algorithm keeps updating the template and criteria after certain period. The templates are automatically replaced by the newly recognized approaching/leaving images, and the judging criteria is updated by evaluating the new templates and images.

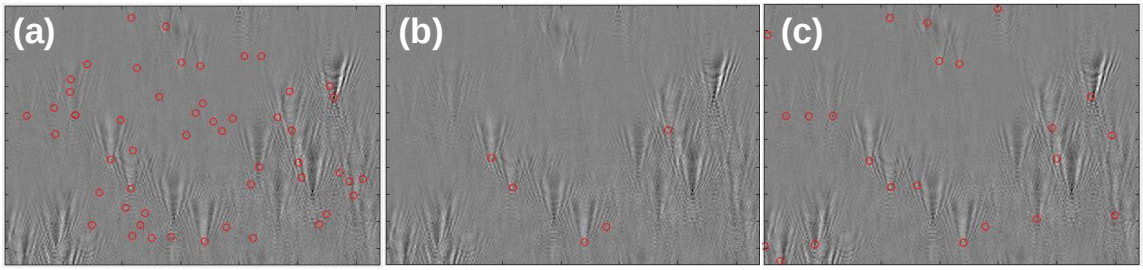

Figure 4.28: Different judging criteria will lead to different counting results. (a) Loose; (b) Tight; (c) Proper.

By recognizing the spots with strong correlation on each frame, particles approaching and leaving the surface at certain time could be determined. This provides both the temporal and spatial information of the nanoparticles. Then a quick check is initialized. First, if one spot is found to be both approaching and leaving at the same frame, it indicates the particle is fluctuation along the surface and it will not be counted. Second, two types of counting error are checked and corrected. One is the spot only has the leaving signal, this may be caused by missing count of an approaching signal or the particle is already there before starting point. In both cases, deleting the signal does not affect the final counting number. This case is usually very rare (<0.1%). Another case is that approaching signal may occur at a spot many times but without any leaving signal. In this case we only keep the last approaching signal since that is the only one responsible for our counting. A final check will be made by human to confirm the result.

4.4.4 Nanoparticle Oscillation Measurement

Another application for the focus SPR microscopy is to observe nanoparticle oscillation. Shan et al. in our group have demonstrated to use conventional SPR microscopy to measure the oscillation of gold nanoparticles which are linked to the surface by PEG tether to detect binding and phosphorylation events.[45,46] Since the gold particles are quasi-

fasten to the surface, it will be easy for focus SPR microscopy to do the measurement. The preparation of the sample is discussed somewhere else.[45] The focus SPR measurement of the 50 nm gold nanoparticle oscillation is present in Fig.4.29, which shows better SNR compared with conventional setup because of suppressed background and pixel noise.

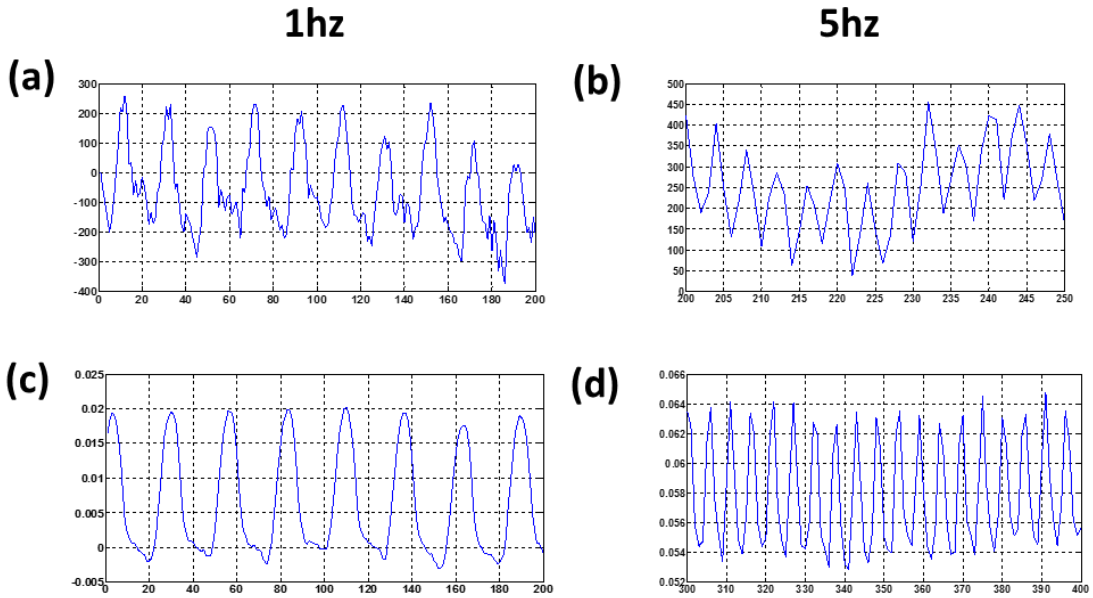

Figure 4.29: Detection oscillation signal of 50 nm gold particles (frame rate: 50 fps). (a) and (b) are the results of conventional SPR microscopy; (c) and (d) are the results of focused SPR microscopy.

4.5 Conclusion

In conclusion, we have developed the focused SPR microscopy and demonstrated its capability for detecting refractive index change. The bi-cell algorithm provides a way to evaluate the signal and eliminate the common noise from light source. Compared with conventional SPR microscopy, it offers higher spatial resolution and better SNR. Using this technique, we have successfully measured the single binding events of 100 nm and 65 nm polystyrene beads non-specific binding and oscillations of 50 nm Au nanoparticles. We hope this will provide a new way of plasmonic imaging-based protein detection.

CHAPTER 5

CONCLUSIONS AND PERSPECTIVES

5.1 Conclusions

As a biosensing technique, plasmonic based techniques needs to be sensitive, fast, high throughput and specific. My doctoral projects are also based on these directions. The major contributions include:

1. A fast plasmonic electrochemical microscopy (P-ECM) technique was developed for electron transfer detection using a plasmonic imaging method combined with microfabricated microelectrodes. Applied this technique, fast ET processes in a redox protein (Cytochrome c) adsorbed on a microelectrode was measured. Interestingly, we find the contribution of ET to the plasmonic signal is relatively larger than charging, making it easier to study ET compared with the traditional electrical method. According the measurement, the conformational fluctuations of cytochrome c gate the ET reaction of the protein, and the time scale of the gating occurs from over a broad time range (100 ns – 1 ms).
2. A breadboard version IMPDS setup that is capable of printing less than 10 nL droplets was developed. Spot-on-spot accuracy of 10×10 nanodroplet microarray with less than 5% alignment variability and droplet stability (no measurable evaporation) for more than 10 minutes were achieved. We also carried experiments to demonstrate the feasibility of detecting protein-protein interactions using IMPDS technology. We also developed a prototype data analysis software that can automatically and systematically analysis the information obtained from IMPDS system, which considering the depletion and diffusion the droplet system.

3. I further developed the focused plasmonic imaging system. With a bi-cell algorithm integrated, we could obtain a good signal to noise ratio. The system could be operated at two different modes. For the scanning mode, we use scanning mirror to scan the whole surface and get an enhanced spatial resolution picture compared with conventional SPR microscopy. For the focus mode, we use drug delivery system to detect the binding on the focused spots. We successfully measure the single binding events of 100 nm and 65 nm polystyrene beads non-specific binding, and oscillations of 50 nm Au nanoparticles.

5.2 Perspectives

My research works focused on extending the application field of plasmonic based imaging techniques on protein detections, including the conformational change and interaction kinetics. Combination of these platforms may offer the possibility for new discoveries. As for each technique, the future works include:

1. Ultrafast electrochemical detection technique: Further improvement on temporal resolution to picosecond regime is needed. The response of plasmonic imaging based detection system will not be a problem since we can reduce the feedback resistance of photodiode circuit and increase the light power and averaging more cycles. The real limitation for the whole system speed is how to trigger the fast reaction. In our system, the parasitic resistance and capacitance affect the final speed. There are two methods to overcome it. One way is to attach a photodiode to the electrodes as close as possible, and by using a pico-second pulsed laser to trigger the photodiode we should be able to trigger the system. The major concern of this approach will be how to control the

potential that falls on the EC cells because photodiode is a current source. Another way is to combine our system with the ILIT system. We can hold the system at a metastable state using the Potentiostat, and then trigger the reaction by heating with a pulse laser. Here we can apply similar strategy as pump-probe techniques, while the detection beam could be the pulsed laser separated from the one triggering the reaction. The temporal resolution could be enhanced by tuning time difference of trigger pulse and detection pulse with different optical path. And this will hopefully push the speed into pico-second regime.

2. IMPDS: First, droplet array with higher density is needed since 100 spots is not enough for real multiplex measurement. This will need a comprehensive consideration of the droplet size, field of view and printing accuracy. Secondly, we can apply this technique to detect significant biological reactions, such as measuring the kinetics between the proteins in different signaling pathways. This will provide us more details of the pathways. Moreover, by combining the compressive sensing concept, we may further save samples while applying our setup for diagnosis/biomarker detection.
3. Focus SPR microscopy: We can further enhance the sensitivity by using different polarization strategy to excite the surface plasmon. As for applications, since it provides higher spatial resolution, we could measure certain sub-cellular structures and detect activity in specific region of cells when binding happens.

REFERENCES

(1) Pantazis, P.; Maloney, J.; Wu, D.; Fraser, S. E. Second Harmonic Generating (SHG) Nanoprobes for in Vivo Imaging. *Proc. Natl. Acad. Sci.* **2010**.

(2) Shliom, O.; Huang, M.; Sachais, B.; Kou, A.; Weisel, J. W.; Nagaswami, C.; Nassar, T.; Bdeir, K.; Hiss, E.; Gawlak, S.; et al. Novel Interactions between Urokinase and Its Receptor. *J. Biol. Chem.* **2000**, *275* (32), 24304–24312.

(3) Chen, Y.; Nguyen, A.; Niu, L.; Corn, R. M. Fabrication of DNA Microarrays with Poly(l -Glutamic Acid) Monolayers on Gold Substrates for SPR Imaging Measurements. *Langmuir* **2009**, *25* (9), 5054–5060.

(4) Wang, W.; Yang, Y.; Wang, S.; Nagaraj, V. J.; Liu, Q.; Wu, J.; Tao, N. Label-Free Measuring and Mapping of Binding Kinetics of Membrane Proteins in Single Living Cells. *Nat. Chem.* **2012**, *4* (10), 846–853.

(5) Wang, W.; Foley, K.; Shan, X.; Wang, S.; Eaton, S.; Nagaraj, V. J.; Wiktor, P.; Patel, U.; Tao, N. Single Cells and Intracellular Processes Studied by a Plasmonic-Based Electrochemical Impedance Microscopy. *Nat. Chem.* **2011**, *3* (3), 249–255.

(6) Halpern, A. R.; Wood, J. B.; Wang, Y.; Corn, R. M. Single-Nanoparticle Near-Infrared Surface Plasmon Resonance Microscopy for Real-Time Measurements of DNA Hybridization Adsorption. *ACS Nano* **2014**, *8* (1), 1022–1030.

(7) Shan, X.; Díez-Pérez, I.; Wang, L.; Wiktor, P.; Gu, Y.; Zhang, L.; Wang, W.; Lu, J.; Wang, S.; Gong, Q.; et al. Imaging the Electrocatalytic Activity of Single Nanoparticles. *Nat. Nanotechnol.* **2012**, *7* (10), 668–672.

(8) Shan, X.; Patel, U.; Wang, S.; Iglesias, R.; Tao, N. Imaging Local Electrochemical Current via Surface Plasmon Resonance. *Science* **2010**, *327* (5971), 1363–1366.

(9) Peterson, A. W.; Wolf, L. K.; Georgiadis, R. M. Hybridization of Mismatched or Partially Matched DNA at Surfaces. *J. Am. Chem. Soc.* **2002**.

(10) Chadwick, B.; Gal, M. An Optical Temperature Sensor Using Surface Plasmons. *Jpn. J. Appl. Phys.* **1993**, *32* (Part 1, No. 6A), 2716–2717.

(11) Chen, Z.; Shan, X.; Guan, Y.; Wang, S.; Zhu, J.-J.; Tao, N. Imaging Local Heating and Thermal Diffusion of Nanomaterials with Plasmonic Thermal Microscopy. *ACS Nano* **2015**, *9* (12), 11574–11581.

(12) Palumbo, M.; Nagel, J.; Petty, M. C. Surface Plasmon Resonance Detection of Metal Ions: Layer-by-Layer Assembly of Polyelectrolyte Sensing Layers on a Multichannel Chip. *IEEE Sens. J.* **2005**, *5* (6), 1159–1164.

(13) Yuk, J. S.; Jung, J.-W.; Jung, S.-H.; Han, J.-A.; Kim, Y.-M.; Ha, K.-S. Sensitivity

of Ex Situ and in Situ Spectral Surface Plasmon Resonance Sensors in the Analysis of Protein Arrays. *Biosens. Bioelectron.* **2005**, *20* (11), 2189–2196.

(14) Zhang, J.; Zhang, L.; Xu, W. Surface Plasmon Polaritons: Physics and Applications. *J. Phys. D. Appl. Phys.* **2012**, *45* (11), 113001.

(15) Surface plasmon https://en.wikipedia.org/wiki/Surface_plasmon.

(16) *Handbook of Surface Plasmon Resonance*; Schasfoort, R. B. M., Ed.; Royal Society of Chemistry: Cambridge, 2017.

(17) Otto, A. Excitation of Nonradiative Surface Plasma Waves in Silver by the Method of Frustrated Total Reflection. *Zeitschrift für Phys. A Hadron. Nucl.* **1968**, *216* (4), 398–410.

(18) Kretschmann, E. Die Bestimmung Optischer Konstanten von Metallen Durch Anregung von Oberflächenplasmaschwingungen. *Zeitschrift für Phys. A Hadron. Nucl.* **1971**, *241* (4), 313–324.

(19) Raether, H. *Surface Plasmons on Smooth and Rough Surfaces and on Gratings*; Springer Tracts in Modern Physics; Springer Berlin Heidelberg: Berlin, Heidelberg, 1988; Vol. 111.

(20) Chiu, N.-F.; Huang, T.-Y.; Lai, H.-C. Graphene Oxide Based Surface Plasmon Resonance Biosensors. In *Advances in Graphene Science*; InTech, 2013.

(21) Wegner, G. J.; Wark, A. W.; Lee, H. J.; Codner, E.; Saeki, T.; Fang, S.; Corn, R. M. Real-Time Surface Plasmon Resonance Imaging Measurements for the Multiplexed Determination of Protein Adsorption/Desorption Kinetics and Surface Enzymatic Reactions on Peptide Microarrays. *Anal. Chem.* **2004**, *76* (19), 5677–5684.

(22) Huang, B.; Yu, F.; Zare, R. N. Surface Plasmon Resonance Imaging Using a High Numerical Aperture Microscope Objective. *Anal. Chem.* **2007**, *79* (7), 2979–2983.

(23) Henzler-Wildman, K.; Kern, D. Dynamic Personalities of Proteins. *Nature* **2007**, *450* (7172), 964–972.

(24) Picot, D.; Loll, P. J.; Garavito, R. M. The X-Ray Crystal Structure of the Membrane Protein Prostaglandin H2 Synthase-1. *Nature* **1994**, *367* (6460), 243–249.

(25) Bai, X.; Yan, C.; Yang, G.; Lu, P.; Ma, D.; Sun, L.; Zhou, R.; Scheres, S. H. W.; Shi, Y. An Atomic Structure of Human γ-Secretase. *Nature* **2015**, *525* (7568), 212–217.

(26) Alsteens, D.; Pfreundschuh, M.; Zhang, C.; Spoerri, P. M.; Coughlin, S. R.;

Kobilka, B. K.; Müller, D. J. Imaging G Protein-Coupled Receptors While Quantifying Their Ligand-Binding Free-Energy Landscape. *Nat. Methods* **2015**, *12* (9), 845–851.

(27) Maurel, D.; Comps-Agrar, L.; Brock, C.; Rives, M.-L.; Bourrier, E.; Ayoub, M. A.; Bazin, H.; Tinel, N.; Durroux, T.; Prézeau, L.; et al. Cell-Surface Protein-Protein Interaction Analysis with Time-Resolved FRET and Snap-Tag Technologies: Application to GPCR Oligomerization. *Nat. Methods* **2008**, *5* (6), 561–567.

(28) Pascher, T.; Chesick, J. P.; Winkler, J. R.; Gray, H. B. Protein Folding Triggered by Electron Transfer. *Science* **1996**, *271* (5255), 1558–1560.

(29) Garner, M. M.; Revzin, A. A Gel Electrophoresis Method for Quantifying the Binding of Proteins to Specific DNA Regions: Application to Components of the Escherichia Coli Lactose Operon Regulatory System. *Nucleic Acids Res.* **1981**, *9* (13), 3047–3060.

(30) Karlsson, R.; Fält, A. Experimental Design for Kinetic Analysis of Protein-Protein Interactions with Surface Plasmon Resonance Biosensors. *J. Immunol. Methods* **1997**, *200* (1–2), 121–133.

(31) Akiyama, S.; Takahashi, S.; Kimura, T.; Ishimori, K.; Morishima, I.; Nishikawa, Y.; Fujisawa, T. Conformational Landscape of Cytochrome c Folding Studied by Microsecond-Resolved Small-Angle x-Ray Scattering. *Proc. Natl. Acad. Sci.* **2002**, *99* (3), 1329 LP-1334.

(32) EGFR Signaling Pathway | SinoBiological https://www.sinobiological.com/EGFR-Signaling-Pathway_image_pegfr-signaling-pathway.html (accessed Jul 16, 2018).

(33) Liedberg, B.; Nylander, C.; Lunström, I. Surface Plasmon Resonance for Gas Detection and Biosensing. *Sensors and Actuators* **1983**, *4*, 299–304.

(34) Flanagan, M. T.; Pantell, R. H. Surface Plasmon Resonance and Immunosensors. *Electron. Lett.* **1984**, *20* (23), 968.

(35) Lundström, I. Real-Time Biospecific Interaction Analysis. *Biosens. Bioelectron.* **1994**, *9* (9–10), 725–736.

(36) Sota, H.; Hasegawa, Y.; Iwakura, M.; and, H. S.; Hasegawa, Y.; Iwakura, M. Detection of Conformational Changes in an Immobilized Protein Using Surface Plasmon Resonance. *Anal. Chem.* **1998**, *70* (10), 2019–2024.

(37) Wang, S.; Boussaad, S.; Tao, N. J. Surface Plasmon Resonance Spectroscopy: Applications in Protein Adsorption and Electrochemistry. **2003**, 209–246.

(38) Homola, J.; Yee, S. S.; Gauglitz, G. Surface Plasmon Resonance Sensors: Review.

Sensors Actuators B Chem. **1999**, *54* (1–2), 3–15.

(39) Biacore 8K - GE Healthcare Life Sciences https://www.gelifesciences.com/en/us/shop/protein-analysis/spr-label-free-analysis/systems/biacore-8k-p-05540 (accessed Jul 17, 2018).

(40) ProteOn™ XPR36 Protein Interaction Array System | Life Science Research | Bio-Rad http://www.bio-rad.com/en-us/product/proteon-xpr36-protein-interaction-array-system?ID=ea380548-08ca-4b4e-896b-87e5580ac411 (accessed Jul 17, 2018).

(41) Foley, K. J.; Shan, X.; Tao, N. J. Surface Impedance Imaging Technique. *Anal. Chem.* **2008**, *80* (13), 5146–5151.

(42) Liang, W.; Wang, S.; Festa, F.; Wiktor, P.; Wang, W.; Magee, M.; LaBaer, J.; Tao, N. Measurement of Small Molecule Binding Kinetics on a Protein Microarray by Plasmonic-Based Electrochemical Impedance Imaging. *Anal. Chem.* **2014**, *86* (19), 9860–9865.

(43) Lu, J.; Wang, W.; Wang, S.; Shan, X.; Li, J.; Tao, N. Plasmonic-Based Electrochemical Impedance Spectroscopy: Application to Molecular Binding. *Anal. Chem.* **2012**, *84* (1), 327–333.

(44) Zhang, F.; Wang, S.; Yin, L.; Yang, Y.; Guan, Y.; Wang, W.; Xu, H.; Tao, N. Quantification of Epidermal Growth Factor Receptor Expression Level and Binding Kinetics on Cell Surfaces by Surface Plasmon Resonance Imaging. *Anal. Chem.* **2015**, *87* (19), 9960–9965.

(45) Shan, X.; Fang, Y.; Wang, S.; Guan, Y.; Chen, H.-Y.; Tao, N. Detection of Charges and Molecules with Self-Assembled Nano-Oscillators. *Nano Lett.* **2014**, *14* (7), 4151–4157.

(46) Fang, Y.; Chen, S.; Wang, W.; Shan, X.; Tao, N. Real-Time Monitoring of Phosphorylation Kinetics with Self-Assembled Nano-Oscillators. *Angew. Chemie Int. Ed.* **2015**, *54* (8), 2538–2542.

(47) Yin, L.; Yang, Y.; Wang, S.; Wang, W.; Zhang, S.; Tao, N. Measuring Binding Kinetics of Antibody-Conjugated Gold Nanoparticles with Intact Cells. *Small* **2015**, *11* (31), 3782–3788.

(48) Lu, J.; Yang, Y.; Wang, W.; Li, J.; Tao, N.; Wang, S. Label-Free Imaging of Histamine Mediated G Protein-Coupled Receptors Activation in Live Cells. *Anal. Chem.* **2016**, *88* (23), 11498–11503.

(49) Liu, X.-W.; Yang, Y.; Wang, W.; Wang, S.; Gao, M.; Wu, J.; Tao, N. Plasmonic-Based Electrochemical Impedance Imaging of Electrical Activities in Single Cells. *Angew. Chemie Int. Ed.* **2017**, *56* (30), 8855–8859.

(50) Photosynthesis https://en.wikipedia.org/wiki/Photosynthesis.

(51) Buses World News: ELECTRIC BATTERY MAKER * USA - Tesla Motors, is planning to build its giant battery “gigafactory” in https://busnews.blogspot.com/2015/03/electric-battery-maker-usa-tesla-motors.html.

(52) Dye Sensitized Solar Cells | DSSC | GCellG24 https://gcell.com/dye-sensitized-solar-cells.

(53) Fujishima, A.; Honda, K. Electrochemical Evidence for the Mechanism of the Primary Stage of Photosynthesis. *Bull. Chem. Soc. Jpn.* **1971**, *44* (4), 1148–1150.

(54) Crofts, A. R.; Wraight, C. A. The Electrochemical Domain of Photosynthesis. *Biochim. Biophys. Acta - Rev. Bioenerg.* **1983**, *726* (3), 149–185.

(55) Chidsey, C. E. Free Energy and Temperature Dependence of Electron Transfer at the Metal-Electrolyte Interface. *Science* **1991**, *251* (4996), 919–922.

(56) Sikes, H. D.; Smalley, J. F.; Dudek, S. P.; Cook, A. R.; Newton, M. D.; Chidsey, C. E.; Feldberg, S. W. Rapid Electron Tunneling through Oligophenylenevinylene Bridges. *Science* **2001**, *291* (5508), 1519–1523.

(57) Chan, C.-K.; Hofrichter, J.; Eaton, W. A.; Winkler, J. R.; Gray, H. B. Optical Triggers of Protein Folding. *Science (80-.).* **1996**, *274* (5287), 628 LP-629.

(58) Xiang, L.; Palma, J. L.; Bruot, C.; Mujica, V.; Ratner, M. A.; Tao, N. Intermediate Tunnelling–hopping Regime in DNA Charge Transport. *Nat. Chem.* **2015**, *7* (3), 221–226.

(59) Gray, H. B.; Winkler, J. R. Electron Transfer in Proteins. *Annu. Rev. Biochem.* **1996**, *65* (1), 537–561.

(60) Li, H.; Du, M.; Mleczko, M. J.; Koh, A. L.; Nishi, Y.; Pop, E.; Bard, A. J.; Zheng, X. Kinetic Study of Hydrogen Evolution Reaction over Strained MoS2 with Sulfur Vacancies Using Scanning Electrochemical Microscopy. *J. Am. Chem. Soc.* **2016**, *138* (15), 5123–5129.

(61) Zhou, X.-S.; Liu, L.; Fortgang, P.; Lefevre, A.-S.; Serra-Muns, A.; Raouafi, N.; Amatore, C.; Mao, B.-W.; Maisonhaute, E.; Schöllhorn, B. Do Molecular Conductances Correlate with Electrochemical Rate Constants? Experimental Insights. *J. Am. Chem. Soc.* **2011**, *133* (19), 7509–7516.

(62) Electron transport chain https://en.wikipedia.org/wiki/Electron_transport_chain (accessed Jul 17, 2018).

(63) Beratan, D. N.; Betts, J. N.; Onuchic, J. N. Protein Electron Transfer Rates Set by

the Bridging Secondary and Tertiary Structure. *Science (80-.).* **1991**, *252* (5010), 1285 LP-1288.

(64) Beratan, D. N.; Onuchic, J. N.; Winkler; Gray, H. B. Electron-Tunneling Pathways in Proteins. *Science (80-.).* **1992**, *258* (5089), 1740 LP-1741.

(65) Skourtis, S. S.; Balabin, I. A.; Kawatsu, T.; Beratan, D. N. Protein Dynamics and Electron Transfer: Electronic Decoherence and Non-Condon Effects. *Proc. Natl. Acad. Sci. U. S. A.* **2005**, *102* (10), 3552 LP-3557.

(66) Khoa, L. H.; A., M. M.; F., M. D.; Damian, A.-P.; Wiebke, M.; Anja, K.; M., W. I.; Peter, H.; H., M. D. Thermal Fluctuations Determine the Electron-Transfer Rates of Cytochrome c in Electrostatic and Covalent Complexes. *ChemPhysChem* **2010**, *11* (6), 1225–1235.

(67) Milo, R.; Phillips, R. *Cell Biology by the Numbers*.

(68) Smalley, J. F.; Sachs, S. B.; Chidsey, C. E. D.; Dudek, S. P.; Sikes, H. D.; Creager, S. E.; Yu, C. J.; Feldberg, S. W.; Newton, M. D. Interfacial Electron-Transfer Kinetics of Ferrocene through Oligophenyleneethynylene Bridges Attached to Gold Electrodes as Constituents of Self-Assembled Monolayers: Observation of a Nonmonotonic Distance Dependence. *J. Am. Chem. Soc.* **2004**, *126* (44), 14620–14630.

(69) Robinson, D. B.; Chidsey, C. E. D. Submicrosecond Electron Transfer to Monolayer-Bound Redox Species on Gold Electrodes at Large Overpotentials. *J. Phys. Chem. B* **2002**, *106* (41), 10706–10713.

(70) Avila, A.; Gregory, B. W.; Niki, K.; Cotton, T. M. An Electrochemical Approach to Investigate Gated Electron Transfer Using a Physiological Model System : Cytochrome c Immobilized on Carboxylic Acid-Terminated Alkanethiol Self-Assembled Monolayers on Gold Electrodes. *J. Phys. Chem. B* **2000**, *104* (12), 2759–2766.

(71) Feng, Z. Q.; Imabayashi, S.; Kakiuchi, T.; Niki, K. Electroreflectance Spectroscopic Study of the Electron Transfer Rate of Cytochrome c Electrostatically Immobilized on the ω-Carboxyl Alkanethiol Monolayer Modified Gold Electrode. *J. Electroanal. Chem.* **1995**, *394* (1–2), 149–154.

(72) Pump-probe http://www.unitus.it/biophysics/ricercaen_file/Spectroscopy_file/Pump-probe.htm.

(73) Zinth, W.; Wachtveitl, J. The First Picoseconds in Bacterial Photosynthesis-Ultrafast Electron Transfer for the Efficient Conversion of Light Energy. *ChemPhysChem* **2005**, *6* (5), 871–880.

(74) Cyclic Voltammetry - Chemistry LibreTexts

https://chem.libretexts.org/Textbook_Maps/Analytical_Chemistry/Supplemental_Modules_(Analytical_Chemistry)/Instrumental_Analysis/Cyclic_Voltammetry (accessed Jul 17, 2018).

(75) Bard, A. J.; Faulkner, L. R. *Electrochemical Methods : Fundamentals and Applications*; Wiley, 2001.

(76) Liu, B.; Bard, A. J.; Mirkin, M. V; Creager, S. E. Electron Transfer at Self-Assembled Monolayers Measured by Scanning Electrochemical Microscopy. *J. Am. Chem. Soc.* **2004**, *126* (5), 1485–1492.

(77) Wipf, D. O. Ohmic Drop Compensation in Voltammetry: Iterative Correction of the Applied Potential. *Anal. Chem.* **1996**, *68* (11), 1871–1876.

(78) Bard, A. J.; Rubinstein, I. *Electroanalytical Chemistry : A Series of Advances. Vol. 22*; Marcel Dekker, 2004.

(79) Smalley, J. F.; Krishnan, C. V.; Goldman, M.; Feldberg, S. W.; Ruzic, I. Laser-Induced Temperature-Jump Coulostatics for the Investigation of Heterogeneous Rate Processes: Theory and Application. *J. Electroanal. Chem. Interfacial Electrochem.* **1988**, *248* (2), 255–282.

(80) Smalley, J. F.; Geng, L.; Feldberg, S. W.; Rogers, L. C.; Leddy, J. Evidence for Adsorption of Fe(CN)63−/4− on Gold Using the Indirect Laser-Induced Temperature-Jump Method. *J. Electroanal. Chem.* **1993**, *356* (1–2), 181–200.

(81) Qiang Feng, Z.; Imabayashi, S.; Kakiuchi, T.; Niki, K. Long-Range Electron-Transfer Reaction Rates to Cytochrome c across Long- and Short-Chain Alkanethiol Self-Assembled Monolayers: Electroreflectance Studies. *J. Chem. Soc. Faraday Trans.* **1997**, *93* (7), 1367–1370.

(82) Murgida, D. H.; Hildebrandt, P. Electron-Transfer Processes of Cytochrome c at Interfaces. New Insights by Surface-Enhanced Resonance Raman Spectroscopy. *Acc. Chem. Res.* **2004**, *37* (11), 854–861.

(83) Murgida, D. H.; Hildebrandt, P. Active-Site Structure and Dynamics of Cytochrome c Immobilized on Self-Assembled Monolayers-A Time-Resolved Surface Enhanced Resonance Raman Spectroscopic Study This Work Was Supported by the Deutsche Forschungsgemeinschaft, the Volkswagenstiftung, and Th. *Angew. Chem. Int. Ed. Engl.* **2001**, *40* (4), 728–731.

(84) Jianjun, W.; Haiying, L.; E., K. D.; Hiromichi, Y.; Allison, D.; H., W. D. Electron-Transfer Dynamics of Cytochrome C: A Change in the Reaction Mechanism with Distance. *Angew. Chemie Int. Ed.* **2002**, *41* (24), 4700–4703.

(85) Khoshtariya, D. E.; Wei, J.; Liu, H.; Yue, H.; Waldeck, D. H. Charge-Transfer Mechanism for Cytochrome. *Physica* **2003**, No. c, 7704–7714.

(86) Yuan, X.; Sun, S.; Hawkridge, F. M.; Chlebowski, J. F.; Taniguchi, I. The Rate of Conformational Change of Cytochrome c during Electron Transfer Determined by Double-Potential Step Chronoelliptometry. *J. Am. Chem. Soc.* **1990**, *112* (13), 5380–5381.

(87) Boussaad, S.; Tao, N. J. J. Kinetics of Electron Transfer-Induced Conformational Changes in Cytochrome c Immobilized on Electrodes Studied with Surface Plasmon Resonance. *J. Electroanal. Chem.* **2003**, *554–555* (1), 233–239.

(88) Tarlov, M. J.; Bowden, E. F. Electron-Transfer Reaction of Cytochrome c Adsorbed on Carboxylic Acid Terminated Alkanethiol Monolayer Electrodes. *J. Am. Chem. Soc.* **1991**, *113* (5), 1847–1849.

(89) Fardad, F.; J., B. A.; V., M. M. Voltammetric and Scanning Electrochemical Microscopic Studies of the Adsorption Kinetics and Self-Assembly of n-Alkanethiol Monolayers on Gold. *Isr. J. Chem.* **1997**, *37* (2-3), 155–163.

(90) Marken, F.; Paddon, C. A.; Asogan, D. Direct Cytochrome c Electrochemistry at Boron-Doped Diamond Electrodes. *Electrochem. commun.* **2002**, *4* (1), 62–66.

(91) Wang, S.; Huang, X.; Shan, X.; Foley, K. J.; Tao, N. Electrochemical Surface Plasmon Resonance: Basic Formalism and Experimental Validation. *Anal. Chem.* **2010**, *82* (3), 935–941.

(92) Fang, Y.; Wang, W.; Wo, X.; Luo, Y.; Yin, S.; Wang, Y.; Shan, X.; Tao, N. Plasmonic Imaging of Electrochemical Oxidation of Single Nanoparticles. *J. Am. Chem. Soc.* **2014**, *136* (36), 12584–12587.

(93) Wang, Y.; Shan, X.; Cui, F.; Li, J.; Wang, S.; Tao, N. Electrochemical Reactions in Subfemtoliter-Droplets Studied with Plasmonics-Based Electrochemical Current Microscopy. *Anal. Chem.* **2015**, *87* (1), 494–498.

(94) Fang, Y.; Wang, H.; Yu, H.; Liu, X.; Wang, W.; Chen, H.-Y.; Tao, N. J. Plasmonic Imaging of Electrochemical Reactions of Single Nanoparticles. *Acc. Chem. Res.* **2016**, *49* (11), 2614–2624.

(95) Margoliash, E.; Frohwirt, N. Appendix—Spectrum of Horse-Heart Cytochrome C. *Biochem. J.* **1959**, *71* (3), 570–572.

(96) Boussaad, S.; Pean, J.; Tao, N. J. High-Resolution Multiwavelength Surface Plasmon Resonance Spectroscopy for Probing Conformational and Electronic Changes in Redox Proteins. *Anal. Chem.* **2000**, *72* (1), 222–226.

(97) Wang, S.; Boussaad, S.; Tao, N. J. Surface Plasmon Resonance Enhanced Optical Absorption Spectroscopy for Studying Molecular Adsorbates. *Rev. Sci. Instrum.* **2001**, *72* (7), 3055–3060.

(98) Zhou, X.-S.; Mao, B.-W.; Amatore, C.; Compton, R. G.; Marignier, J.-L.; Mostafavi, M.; Nierengarten, J.-F.; Maisonhaute, E. Transient Electrochemistry: Beyond Simply Temporal Resolution. *Chem. Commun.* **2016**, *52* (2), 251–263.

(99) Cooper, J. M.; Greenough, K. R.; McNeil, C. J. Direct Electron Transfer Reactions between Immobilized Cytochrome c and Modified Gold Electrodes. *J. Electroanal. Chem.* **1993**, *347* (1–2), 267–275.

(100) HPLC Analysis of Cytochrome c Species Variants on Discovery® BIO Wide Pore C18 | Sigma-Aldrich https://www.sigmaaldrich.com/technical-documents/articles/analytical-applications/hplc/hplc-analysis-of-cytochrome-c-species-variants-g001581.html?lang=en&region=US (accessed Jul 17, 2018).

(101) Vanneste, W. H. The Stoichiometry and Absorption Spectra of Components a and A3 in Cytochrome c Oxidase. *Biochemistry* **1966**, *5* (3), 838–848.

(102) Phillips, J. C. Stretched Exponential Relaxation in Molecular and Electronic Glasses. *Reports Prog. Phys.* **1996**, *59* (9), 1133–1207.

(103) Khodadadi, S.; Sokolov, A. P. Protein Dynamics: From Rattling in a Cage to Structural Relaxation. *Soft Matter* **2015**, *11* (25), 4984–4998.

(104) Johnston, D. C. Stretched Exponential Relaxation Arising from a Continuous Sum of Exponential Decays. *Phys. Rev. B* **2006**, *74* (18), 184430.

(105) Brautigan, D. L.; Ferguson-Miller, S.; Margoliash, E. Definition of Cytochrome c Binding Domains by Chemical Modification. I. Reaction with 4-Chloro-3,5-Dinitrobenzoate and Chromatographic Separation of Singly Substituted Derivatives. *J. Biol. Chem.* **1978**, *253* (1), 130–139.

(106) Brautigan, D. L.; Ferguson-Miller, S.; Margoliash, E. [18] Mitochondrial Cytochrome c: Preparation and Activity of Native and Chemically Modified Cytochromes C. *Methods Enzymol.* **1978**, *53*, 128–164.

(107) Ferguson-Miller, S.; Brautigan, D. L.; Margoliash, E. Definition of Cytochrome c Binding Domains by Chemical Modification. III. Kinetics of Reaction of Carboxydinitrophenyl Cytochromes c with Cytochrome c Oxidase. *J. Biol. Chem.* **1978**, *2* (1), 140–148.

(108) Macarron, R.; Banks, M. N.; Bojanic, D.; Burns, D. J.; Cirovic, D. A.; Garyantes, T.; Green, D. V. S.; Hertzberg, R. P.; Janzen, W. P.; Paslay, J. W.; et al. Impact of High-Throughput Screening in Biomedical Research. *Nat. Rev. Drug Discov.* **2011**, *10* (3), 188–195.

(109) Bradbury, A.; Plückthun, A. Reproducibility: Standardize Antibodies Used in Research. *Nature* **2015**, *518* (7537), 27–29.

(110) Tyson, J. J.; Chen, K. C.; Novak, B. Sniffers, Buzzers, Toggles and Blinkers: Dynamics of Regulatory and Signaling Pathways in the Cell. *Curr. Opin. Cell Biol.* **2003**, *15* (2), 221–231.

(111) Cepok, S.; Zhou, D.; Srivastava, R.; Nessler, S.; Stei, S.; Büssow, K.; Sommer, N.; Hemmer, B. Identification of Epstein-Barr Virus Proteins as Putative Targets of the Immune Response in Multiple Sclerosis. *J. Clin. Invest.* **2005**, *115* (5), 1352–1360.

(112) Copeland, R. A.; Pompliano, D. L.; Meek, T. D. Drug–target Residence Time and Its Implications for Lead Optimization. *Nat. Rev. Drug Discov.* **2006**, *5* (9), 730–739.

(113) Swinney, D. C. The Role of Binding Kinetics in Therapeutically Useful Drug Action. *Curr. Opin. Drug Discov. Devel.* **2009**, *12* (1), 31–39.

(114) How many Proteins exist in human body? http://www.innovateus.net/health/how-many-proteins-exist-human-body.

(115) Butterworth, P. J. Lehninger: Principles of Biochemistry (4th Edn) D. L. Nelson and M. C. Cox, W. H. Freeman & Co., New York, 1119 Pp (plus 17 Pp Glossary), ISBN 0-7167-4339-6 (2004). *Cell Biochem. Funct.* **2005**, *23* (4), 293–294.

(116) Walker, J. M.; Rapley, R.; Royal Society of Chemistry (Great Britain). *Molecular Biology and Biotechnology.*; Royal Society of Chemistry, 2009.

(117) Anker, J. N.; Hall, W. P.; Lyandres, O.; Shah, N. C.; Zhao, J.; Van Duyne, R. P. Biosensing with Plasmonic Nanosensors. *Nat. Mater.* **2008**, *7* (6), 442–453.

(118) Medintz, I. L.; Uyeda, H. T.; Goldman, E. R.; Mattoussi, H. Quantum Dot Bioconjugates for Imaging, Labelling and Sensing. *Nat. Mater.* **2005**, *4* (6), 435–446.

(119) Cooper, M. A. Label-Free Screening of Bio-Molecular Interactions. *Anal. Bioanal. Chem.* **2003**, *377* (5), 834–842.

(120) Pan, Y.; Herr, A.; Huang, B.; Wu, M. High-Throughput Molecular Binding Analysis on Open-Microfluidic Platform. **2016**.

(121) Mahlknecht, U.; Ottmann, O. G.; Hoelzer, D. Far-Western Based Protein–protein Interaction Screening of High-Density Protein Filter Arrays. *J. Biotechnol.* **2001**, *88* (2), 89–94.

(122) Giepmans, B. N. G.; Adams, S. R.; Ellisman, M. H.; Tsien, R. Y. The Fluorescent Toolbox for Assessing Protein Location and Function. *Science (80-.).* **2006**, *312* (5771), 217 LP-224.

(123) Swerhone, G. D. W.; Lawrence, J. R.; Neu, T. R. Assessment of Lectin-Binding Analysis for in Situ Detection of Glycoconjugates in Biofilm Systems. *Microbiology* **2001**, *147* (2), 299–313.

(124) Yin, L. L.; Wang, S. P.; Shan, X. N.; Zhang, S. T.; Tao, N. J. Quantification of Protein Interaction Kinetics in a Micro Droplet. *Rev. Sci. Instrum.* **2015**, *86* (11), 114101.

(125) Leavitt, S.; Freire, E. Direct Measurement of Protein Binding Energetics by Isothermal Titration Calorimetry. *Curr. Opin. Struct. Biol.* **2001**, *11* (5), 560–566.

(126) Freyer, M. W.; Lewis, E. A. Isothermal Titration Calorimetry: Experimental Design, Data Analysis, and Probing Macromolecule/Ligand Binding and Kinetic Interactions. *Methods Cell Biol.* **2008**, *84*, 79–113.

(127) Wienken, C. J.; Baaske, P.; Rothbauer, U.; Braun, D.; Duhr, S. Protein-Binding Assays in Biological Liquids Using Microscale Thermophoresis. *Nat. Commun.* **2010**, *1* (7), 100.

(128) Jerabek-Willemsen, M.; Wienken, C. J.; Braun, D.; Baaske, P.; Duhr, S. Molecular Interaction Studies Using Microscale Thermophoresis. *Assay Drug Dev. Technol.* **2011**, *9* (4), 342–353.

(129) Seidel, S. A. I.; Wienken, C. J.; Geissler, S.; Jerabek-Willemsen, M.; Duhr, S.; Reiter, A.; Trauner, D.; Braun, D.; Baaske, P. Label-Free Microscale Thermophoresis Discriminates Sites and Affinity of Protein-Ligand Binding. *Angew. Chemie Int. Ed.* **2012**, *51* (42), 10656–10659.

(130) Bornhop, D. J.; Latham, J. C.; Kussrow, A.; Markov, D. A.; Jones, R. D.; Sørensen, H. S. Free-Solution, Label-Free Molecular Interactions Studied by Back-Scattering Interferometry. *Science (80-.).* **2007**, *317* (5845), 1732 LP-1736.

(131) Baksh, M. M.; Kussrow, A. K.; Mileni, M.; Finn, M. G.; Bornhop, D. J. Label-Free Quantification of Membrane-Ligand Interactions Using Backscattering Interferometry. *Nat. Biotechnol.* **2011**, *29* (4), 357–360.

(132) Homola, J. Surface Plasmon Resonance Sensors for Detection of Chemical and Biological Species. *Chem. Rev.* **2008**, *108* (2), 462–493.

(133) Wang, S.; Shan, X.; Patel, U.; Huang, X.; Lu, J.; Li, J.; Tao, N. Label-Free Imaging, Detection, and Mass Measurement of Single Viruses by Surface Plasmon Resonance. *Proc. Natl. Acad. Sci.* **2010**, *107* (37), 16028 LP-16032.

(134) Rich, R. L.; Myszka, D. G. Advances in Surface Plasmon Resonance Biosensor Analysis. *Curr. Opin. Biotechnol.* **2000**, *11* (1), 54–61.

(135) MacGriff, C.; Wang, S.; Wiktor, P.; Wang, W.; Shan, X.; Tao, N. Charge-Based

Detection of Small Molecules by Plasmonic-Based Electrochemical Impedance Microscopy. *Anal. Chem.* **2013**, *85* (14), 6682–6687.

(136) Chang-Yen, D. A.; Myszka, D. G.; Gale, B. K. A Novel PDMS Microfluidic Spotter for Fabrication of Protein Chips and Microarrays. *J. Microelectromechanical Syst.* **2006**, *15* (5), 1145–1151.

(137) Natarajan, S.; Hatch, A.; Myszka, D. G.; Gale, B. K. Optimal Conditions for Protein Array Deposition Using Continuous Flow. *Anal. Chem.* **2008**, *80* (22), 8561–8567.

(138) Arenkov, P.; Kukhtin, A.; Gemmell, A.; Voloshchuk, S.; Chupeeva, V.; Mirzabekov, A. Protein Microchips: Use for Immunoassay and Enzymatic Reactions. *Anal. Biochem.* **2000**, *278* (2), 123–131.

(139) Campbell, C. T.; Kim, G. SPR Microscopy and Its Applications to High-Throughput Analyses of Biomolecular Binding Events and Their Kinetics. *Biomaterials* **2007**, *28* (15), 2380–2392.

(140) Myszka, D. G.; Rich, R. L. Implementing Surface Plasmon Resonance Biosensors in Drug Discovery. *Pharm. Sci. Technolo. Today* **2000**, *3* (9), 310–317.

(141) Xiao, F. An Integrated Microarray Printing and Detection System to Study Protein-Protein Interactions, Arizona State University, 2017.

(142) Markus, R. Sortagging: A Robust and Efficient Chemoenzymatic Ligation Strategy. *Chem. – A Eur. J.* **2014**, *20* (28), 8516–8529.

(143) Schares, E. S.; Edwards, T. L.; Moorman, M. W.; Polsky, R.; Brozik, S. M.; Manginell, R. P. Three-Dimensional Modeling and Simulation of DNA Hybridization Kinetics and Mass Transport as Functions of Temperature in a Microfluidic Channel. *Electrophoresis* **2013**, *34* (14), 2112–2119.

(144) Watanabe, K.; Matsuura, K.; Kawata, F.; Nagata, K.; Ning, J.; Kano, H. Scanning and Non-Scanning Surface Plasmon Microscopy to Observe Cell Adhesion Sites. *Biomed. Opt. Express* **2012**, *3* (2), 354–359.

(145) Watanabe, K.; Ryosuke, M.; Terakado, G.; Okazaki, T.; Morigaki, K.; Kano, H. High Resolution Imaging of Patterned Model Biological Membranes by Localized Surface Plasmon Microscopy. *Appl. Opt.* **2010**, *49* (5), 887–891.

(146) Yeatman, E. M.; Ash, E. A. Surface Plasmon Scanning Microscopy; Teague, E. C., Ed.; International Society for Optics and Photonics, 1988; Vol. 0897, p 100.

(147) Kano, H.; Knoll, W. Locally Excited Surface-Plasmon-Polaritons for Thickness Measurement of LBK Films. *Opt. Commun.* **1998**, *153* (4–6), 235–239.

(148) Kano, H.; Knoll, W. A Scanning Microscope Employing Localized Surface-Plasmon-Polaritons as a Sensing Probe. *Opt. Commun.* **2000**, *182* (1–3), 11–15.

(149) Watanabe, K.; Horiguchi, N.; Kano, H. Optimized Measurement Probe of the Localized Surface Plasmon Microscope by Using Radially Polarized Illumination. *Appl. Opt.* **2007**, *46* (22), 4985–4990.

(150) Somekh, M. G.; Liu, S. G.; Velinov, T. S.; See, C. W. Optical V(z) for High-Resolution 2π Surface Plasmon Microscopy. *Opt. Lett.* **2000**, *25* (11), 823–825.

(151) Somekh, M. G.; Liu, S.; Velinov, T. S.; See, C. W. High-Resolution Scanning Surface-Plasmon Microscopy. *Appl. Opt.* **2000**, *39* (34), 6279–6287.

(152) Roland, T.; Berguiga, L.; Elezgaray, J.; Argoul, F. Scanning Surface Plasmon Imaging of Nanoparticles. *Phys. Rev. B* **2010**, *81* (23), 235419.

(153) Berguiga, L.; Roland, T.; Monier, K.; Elezgaray, J.; Argoul, F. Amplitude and Phase Images of Cellular Structures with a Scanning Surface Plasmon Microscope. *Opt. Express* **2011**, *19* (7), 6571–6586.

(154) Roland, T. Localized Surface Plasmon Imaging: A Non Intrusive Optical Tool to Cover Nanometer to Micrometer Scales in Biological Systems., Ecole normale supérieure de lyon - ENS LYON, 2009.

(155) Tao, N. J.; Boussaad, S.; Huang, W. L.; Arechabaleta, R. A.; D'Agnese, J. High Resolution Surface Plasmon Resonance Spectroscopy. *Rev. Sci. Instrum.* **1999**, *70* (12), 4656–4660.

(156) Ortega Arroyo, J.; Cole, D.; Kukura, P. Interferometric Scattering Microscopy and Its Combination with Single-Molecule Fluorescence Imaging. *Nat. Protoc.* **2016**, *11* (4), 617–633.

(157) Young, G.; Hundt, N.; Cole, D.; Fineberg, A.; Andrecka, J.; Tyler, A.; Olerinyova, A.; Ansari, A.; Marklund, E. G.; Collier, M. P.; et al. Quantitative Mass Imaging of Single Biological Macromolecules. *Science (80-.).* **2018**, *360* (6387), 423 LP-427.

(158) Normalized 2-D cross-correlation - MATLAB normxcorr2 https://www.mathworks.com/help/images/ref/normxcorr2.html.